Unmanned Aerial Vehicle for Flow Control Experiments with Dielectric Barrier Discharge Plasma Actuators

Vom Fachbereich Maschinenbau
an der Technischen Universität Darmstadt
zur
Erlangung des Grades eines Doktor-Ingenieurs (Dr.-Ing.)
genehmigte

D i s s e r t a t i o n

vorgelegt von

Dipl.-Ing. Wilm Friedrichs

aus Brake (Unterweser)

Berichterstatter:	Prof. Dr.-Ing. C. Tropea
Mitberichterstatter:	Prof. Dr.-Ing. U. Klingauf
Tag der Einreichung:	05. November 2013
Tag der mündlichen Prüfung:	14. Januar 2014

Darmstadt 2014
D17

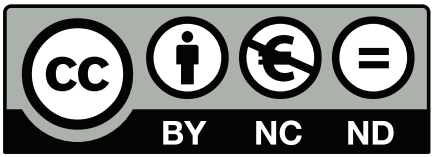

Hiermit erkläre ich, dass ich die vorliegende Arbeit, abgesehen von den in ihr ausdrücklich genannten Hilfen, selbständig verfasst habe.

Darmstadt, den 05.11.2013

Abstract

Dielectric Barrier Discharge (DBD) plasma actuators are a relatively novel type of actuators for active flow control. They offer several benefits, such as fast reaction times due to the absence of mechanical parts. On the other hand there are several difficulties which must be overcome before they reach a stage of maturity suitable for application on aircraft.

In the present study the design, construction and commissioning of an Unmanned Aerial Vehicle (UAV) for flow control experiments with plasma actuators under realistic flight conditions is presented. The UAV has a wingspan of 2.38 m and a flight mass of approximately 10 kg. It is equipped with a flight control system to autonomously conduct the experiments and record measurement data. The fault-free operation of all systems, despite electromagnetic emissions from the high-voltage system of the actuators, and the suitability of the UAV as a flight-test platform have been demonstrated.

Two sections of the modular wing are used for flow control, different airfoil and actuator configurations can thus be interchanged. The attainable Reynolds numbers are in the range of $300,000$ to $600,000$. Validation of the entire system with several configurations has been performed in the wind tunnel prior to free-flight experiments.

Kurzfassung

Dielectric Barrier Discharge (DBD) Plasma-Aktuatoren sind eine relativ neue Art von Aktuatoren zur aktiven Strömungskontrolle. Sie bieten eine Reihe von Vorteilen, wie ihre schnelle Reaktionszeit aufgrund des Fehlens von mechanischen Teilen. Andererseits gibt es einige Problematiken, die überwunden werden müssen, bevor sie einen für die Verwendung auf Flugzeugen erforderlichen Reifegrad erreichen.

In der vorliegenden Arbeit wird daher die Entwicklung, Konstruktion und Inbetriebnahme eines Unmanned Aerial Vehicle (UAV) zur Durchführung von Experimenten zur Strömungskontrolle mit Plasma-Aktuatoren unter realen Flugbedingungen beschrieben. Das UAV hat eine Spannweite von $2,38$ m und eine Flugmasse von circa 10 kg. Zur automatischen Durchführung der Experimente und Messdatenerfassung ist es mit einem Flugkontrollsystem ausgerüstet. Die störungsfreie Funktion aller Systeme, trotz elektromagnetischer Einstreuung durch das Hochspannungssystem der Aktuatoren, und die Eignung des UAV als Messplattform wurden gezeigt.

Zwei Segmente des modular aufgebauten Flügels werden zur Strömungskontrolle genutzt, verschiedene Flügelprofile und Aktuatorkonfigurationen können so verwendet und gegeneinander ausgetauscht werden. Die hierbei erreichten Reynoldszahlen liegen im Bereich von 300.000 bis 600.000. Vor Experimenten im Freiflug wurde eine Validierung des Gesamtsystems mit verschiedenen Konfigurationen im Windkanal durchgeführt.

Acknowledgements

I would like to thank my doctoral advisor Prof. Dr.-Ing. Cameron Tropea for providing the opportunity of pursuing the research leading to this thesis. I am grateful for the advice and support over the years from him and Dr.-Ing. Sven Grundmann. Furthermore, I would like to thank Prof. Dr.-Ing. Uwe Klingauf for refereeing this thesis.

I am truly grateful to all colleagues and the workshop teams at the Center of Smart Interfaces and the Institute of Fluid Mechanics and Aerodynamics in Griesheim for their advice and support. Special thanks go to Johannes Meyer from the Institute of Flight Systems and Automatic Control for his patience and ongoing help with the flight control system and Ralf Kaiser for enabling the flight experiments. Furthermore, I would like to thank my students, who with their work fundamentally contributed to this study.

The research leading to the results presented in this work was conducted as part of the PLASMAERO project. The project has received funding from the European Community's Seventh Framework Programme FP7/2007-2013 under grant agreement n°234201. Further support has come from the Deutsche Forschungsgemeinschaft through Excellence Cluster EXC 259 'Smart Interfaces'.

Contents

1 Introduction

1.1 Motivation

Active flow control is a fast-growing research area aimed at manipulating a flow towards a desired condition. With regards to aeronautical applications the objectives typically are a drag decrease or a lift increase, resulting in a higher lift-to-drag ratio and therefore better efficiency of the aircraft. This overall objective is often pursued by the control of laminar-turbulent transition, separation or reattachment of a boundary layer. Active flow control is of particular interest if the flow has to be optimized for diverse conditions and objectives. For example an aircraft has to fly at preferably low speeds with a corresponding high lift coefficient during take-off while exhibiting minimal drag during cruise flight. The two cases are vastly different, nevertheless both have to be fulfilled satisfactory, requiring an appropriate compromise. Therefore the objective and the efficiency of a flow control device has always to be evaluated in a global context when considering a practical application.

Most often actuators are used that blow air from an orifice or a slot in the surface, either as steady or pulsed flow. Other actuator types include electromechanical and mechanical. A relatively new type of actuator used for flow control are dielectric barrier discharge (DBD) plasma actuators. They induce a wall parallel jet by ionizing the air and thereby generating a plasma through an alternating high voltage applied to them. Although the induced velocities and forces are comparatively low, they act near the wall where the boundary layer is most sensitive. Due to the absence of mechanical parts they act almost instantaneously, making them especially interesting for fast control schemes. Although first publications regarding discharge based flow control devices date back to the 1960s, the rapid increase in interest as a research field began in the late 1990s. However, even more than most active flow control devices, plasma actuator are still far away from a practical aerodynamic application.

Although the research activity in the field of flow control is thriving, few devices have reached the stadium of applicability. Most studies are conducted with the help of wind tunnel experiments or numerical simulations,

only few have been demonstrated in flight experiments. Nonetheless, flight experiments are of particular importance. In wind tunnel experiments, just as in numeric simulations, it is not feasible to reproduce realistic flight conditions. The turbulence intensity and its spectrum, as well as wind tunnel specific errors, result in a different flow field. This is especially important for flow control experiments, where small disturbances in the boundary layer can be very significant. However, in most cases the ultimate objective of the research is an application in flight. Therefore tests under realistic flight conditions have to be conducted as early as possible to identify difficulties and capabilities of the flow control technique. Thus, a key aspect of the ongoing research and of this study in particular is to test and to demonstrate application of these actuators under realistic flight conditions.

Flight experiments require a large organizational, logistical, risk management and legal effort and severely constrain the flow control and measuring equipment in terms of size and weight. Therefore most flow control actuators and measuring methods have to be modified and adapted, if at all possible, and it has to be ensured that the flow control effect is measurable with the equipment used. The devices have to be miniaturized and additional considerations regarding power supply, electromagnetic interference or safety aspects have to be made.

Duchmann [27, 29] carried out transition delay experiments with DBD plasma actuators on a Grob G109b motor glider, equipped with a wing glove setup. The main advantage of this approach is the comparably high payload capacity of the plane, allowing for extensive measurement equipment. Furthermore, it is possible to fly in different atmospheric conditions and altitudes as well as adjust a reproducible and stable flight attitude. The setup allows measurements at relatively high Reynolds numbers in the order of 10^6, which is indicative for practical use of the actuators in future commercial aircraft. However, because of these high Reynolds numbers only a local influence on the flow is achieved with the flow control setup. The plane serves as a carrier for the experiment, a global effect of the actuator on the aircraft is not intended or feasible.

A different approach, pursued in this work, is the use of UAVs with small Reynolds numbers in the order of 10^5. Often these Reynolds numbers are mistakenly considered too small for practical purposes. Nevertheless, considerable research is conducted under these conditions, simply due to experimental limitations. As a consequence of the recent interest in UAVs of different sizes [16, 34], Reynolds numbers in the order of 10^5 to 10^6 are becoming increasingly relevant. These aircraft have a multitude of different

tasks and requirements, their design is less constrained and their cost of development is usually smaller. Therefore they emerge as a promising experimental platform for early practical flow control applications.

Flow control with DBD plasma actuators at high Reynolds numbers appears challenging since the actuators are not scalable and the induced wall-jet velocity appears to have a physical limitation [106]. The flow control authority at large Reynolds numbers is therefore expected to be weak, unless instabilities can be exploited. Additional problems are, as will be elucidated later in this thesis, the high voltages, causing electromagnetic disturbances and the currently limited reliability. UAVs therefore lend themselves also as a suitable testbed for new flow control technologies, since the risks for human life as well as financially can be kept considerably smaller.

In contrast to experiments with the motor glider, flow control experiments with a UAV are aimed to have an impact on the entire aircraft. Possible objectives are, amongst others, lift control for manoeuvering or drag reduction. The use of a UAV enables the transfer of successful wind tunnel tests to in-flight experiments under realistic conditions and thereby moves them closer to actual applications. This approach was followed during the European research project PLASMAERO to demonstrate successful flow control by plasma actuators in flight. Simultaneously the investigated flow control techniques are possible practical applications for the use on future UAV systems, replacing other actuators or control devices. A strict separation of the UAV measurement and control system and the flow control system is therefore desirable, to be able to easily transfer the effect to other aircraft and applications.

The UAV flight test platform described in this study was developed within the scope of the PLASMAERO European research project and is intended as a flight demonstrator for the investigated actuators and flow control effects. The acronym PLASMAERO stands for 'useful PLASMas for AEROdynamic control'. The research project was co-funded by the European Commission as part of the Seventh framework program, lasting from October 2009 to December 2012 and involving ten research institutions and universities with different focuses regarding plasma research and application.

The aim of the project was to investigate how surface and spark discharge plasma actuators can be used to control the aerodynamic flow on aircraft. Details about the project's results can be found in the ERCOFTAC Bulletin Special Theme issue on 'Plasma Aerodynamics' [10, 17, 18, 37, 38, 40, 60, 61, 71, 76, 79, 80, 105].

As part of the final workpackage 'Validation and Integration', a UAV was built to test the most promising actuator designs and configurations developed during the project under realistic flight conditions. The main inputs regarding the actuators and flow configurations were anticipated from other workpackages, especially from the flow separation research. The primary objective was to design, build and operate the UAV with a wingspan of approximately 2 m at the TU Darmstadt to integrate and validate those concepts and help to obtain conclusions and perspectives for plasma actuators as flow control devices.

1.2 Outline of the Thesis

First a short overview of the necessary theoretical and technical foundations is given in Chapter 2. An attempt to classify UAVs and provide an insight into this rapidly growing field is made. Special aspects of aerodynamics at low Reynolds numbers typical of small UAVs are discussed. The topic of active flow control, including objectives, efficiency considerations and actuator types is introduced. The foundations of dielectric barrier discharge plasma actuators are described in detail.

In Chapter 3 the pre-design considerations are discussed. The requirements and objectives of the PLASMAERO project are considered. The UAV for plasma flow control previously developed by Frey [39, 51], is described and the experience made during its operation are evaluated regarding sources of errors and possible improvements. Since at the beginning of the project the feasible flow control authority and possible constraints were unknown, a preliminary wind tunnel study with different conceivable flow control configurations was conducted. The results and the consequential additional requirements to ensure effective flow control are discussed.

Based upon those considerations, the final design of the PLASMAERO UAV is described in Chapter 4. An exhaustive description of the dimensioning, the design of the individual components and the electric system is given. The radio control equipment for manually piloted flights and excitation of the control devices is specified. For reproducible flight manoeuvres during experiments and to record measurement data, a flight control system is installed on board of the aircraft. The sensors, the data acquisition and processing and the flight controller are characterized. For the experiments a high voltage system as a power supply for the actuators has to be installed. The system itself, the measurement of its electrical parameters and the control of the power output by the actuators are described. Fi-

nally, the measures to ensure electromagnetic compatibility of the different systems are shown.

The entire system and its abilities as a flight test platform for flow control experiments are assessed in Chapter 5. The flight behavior and handling is analyzed. The data measured by the system and its quality, especially regarding electromagnetic interference, is described. The processing and interpretation of the data is depicted for the in-flight display as well as the post flight analysis.

In Chapter 6 the set-up for the flow control experiments are described. The different airfoils and the actuators are detailed and the realized combinations of both are given. Furthermore, the configurations of the wind tunnel and the free-flight experiments are explained and specified. The results of these experiments are reported, the success of the flow control for the different airfoil and actuator combinations is described and compared in detail.

Finally an overview of the whole project and the subsequent conclusions are presented in Chapter 7. The success and capability of the UAV as a flight test platform, as well as the actuators as flow control devices are evaluated. Moreover, an outlook and suggestions for further investigations with the developed UAV and further flow control set-ups is given.

2 Theoretical and Technical Foundations

2.1 Unmanned Aerial Vehicles

2.1.1 Classification of UAVs

A wide and expanding variety of UAVs exists at the moment, many of them with a military application, but with falling costs and easy availability also civilian applications are increasing. Many hobby modelers are building small UAVs, participating in the development of sophisticated open-source hard- and software. Possible uses for UAVs in the near future are observation and surveillance, for example for search and rescue, agricultural monitoring and remote sensing. In the long term many applications of currently manned aircraft could be assumed by UAVs. This has already happened in military applications, but could expand to civil transport aircraft.

The following listing of classifications is neither exhaustive nor exact, but gives an introduction to the different layouts, possibilities and requirements for unmanned aerial systems. A more thorough overview can for example be found in [34], additional classification systems exist for military uses.

2.1.1.1 Concept

- Fixed-wing aircraft are probably the most common type used. A multitude of novel configurations are used, since the confinements due to a pilot do not apply. Equipped with a propeller or jet engine these UAVs can reach relatively high speeds and altitudes, making them ideal for missions with longer range.
- Helicopters are highly manoeuvrable, but can only reach short flight times and thereby small range. They are suited for close range missions where manoeuvrability is required, such as urban environments.
- Multirotor configurations are even more maneuverable than helicopters, although with the same disadvantages. They are widely spread because of their suitability for automatic control engineering, many commercial, hobby and research project controllers exist. Their intended objective is often aerial photography and surveillance.

- Flapping-wing are usually very small. At very low Reynolds numbers this concept is interesting, since fixed-wing aircraft are aerodynamically very inefficient in this range. They are usually modeled on insects or birds, but more research is needed to fully understand the unsteady aerodynamics involved and only a few models exist.

- Airships offer very long endurance but only a low airspeed and are thereby suited for long-time surveillance and observation tasks in close range. They can operate for several days and can reach high altitudes.

- Conversions of existing manned aircraft to unmanned air systems are sometimes made to use an existing airframe and thus save development time and money.

2.1.1.2 Autonomy

- Remote controlled with direct line of sight: Can only be used for close range.

- Remote controlled via telemetry: Parts of or the whole flight is flown with the help of a visualization of the flight situation. Often a video downlink is used with additional instrumentation.

- Partially autonomous: Certain flight manoeuvres can be flown autonomously, while others, for example start and landing, are piloted remotely. This is probably the most common type.

- Fully autonomous: All manoeuvres can be flown autonomously.

2.1.1.3 Size

The following considerations of Reynolds number and wingspan are based on fixed-wing aircraft. Other types can more adequately be compared by their flight mass or payload.

- Micro aerial vehicles weigh only a few grams and have a wingspan in the order of 10^{-1} m. Often helicopters and multirotors are used, many researchers work on flapping-wing systems. Typical Reynolds numbers are below 10^5.

- Small UAVs can be considered as having a wingspan in the order of 10^0 m and a mass in the order of kilograms. Typical remote controlled model aircraft fall into this size category with a Reynolds numbers between 10^5 and 10^6.
- Medium sized UAVs feature a mass in the order of 10^2 kg and Reynolds numbers around 10^6.
- Large UAVs at the current state-of-the-art have a mass of several tons and wingspans up to 50 m.

2.1.1.4 Mission Profile

- Long endurance: Missions over a certain area for a long time, for example for observation and surveillance. The speed is of subordinate importance.
- Long range: Heading for a distant target, for example for reconnaissance or transport.
- Close range: Mission in the vicinity, for example reconnaissance in urban environments or agricultural monitoring and crop spraying.
- Expendable: For military use, non-reusable or likely loss, for example target simulation.

2.1.2 Existing UAVs for Flow Control Experiments

Although the multitude of UAV types is large, only few are actually airworthy UAVs for flow control experiments. More often manned aircraft are used to achieve higher Reynolds numbers. UAVs, especially multirotor designs, are frequently used for autonomous flight control, mapping or alternative propulsion research. Some flow control set-ups aim for UAVs, but are tested in wind tunnel experiments with non-airworthy mock-ups. In those cases no special measurement equipment, power supplies and control equipment is needed and no regard to payload, center of gravity, flight operations, legal, organizational or safety issues has to be payed. Due to these complex problems only few projects with UAVs venture towards flow control experiments in free flight, some of which are presented in the following.

Fung [41] describes a ducted-fan UAV with synthetic jet flow control devices in the stator. Thereby the flow can be directed, achieving rotational

and directional control of the UAV. It does not carry any measurement equipment, PIV investigations were made while the model was retained on the ground.

A UAV developed specifically for flow control experiments in flight is described by Gross [50]. It is a scaled down version of a Aeromot 200S SuperXimango motorized glider, the problems of scaling are discussed by Heine [54]. A wing glove is used to investigate the effect of active flow control on separation at different Reynolds numbers, additionally numerical and wind tunnel investigations are conducted.

The probably most extensive and sustained investigations were conducted by Seifert et al. [23, 92, 94]. The UAVs used are modified versions of existing vehicles to allow the installation of flow control airfoil sections and actuators. Lift and drag on the wing sections are controlled with pulsed jet actuators to generate roll and yaw moments to control the plane. The control inputs and resulting motions of the plane are measured and analyzed.

The precursor to the UAV developed in this work was built by Frey [39]. It is described in detail in section 3.1.2. It was used for leading edge separation control experiments with DBD plasma actuators. The measurement equipment consists of an airspeed sensor and logger for model airplanes. Although successful, the measured data was imprecise, failures of the equipment were encountered frequently and the plane's further possibilities were limited by payload and available space.

2.1.3 Legal Aspects

Unmanned aerial vehicles and their ground based components are classified as unmanned aerial systems when not used for sport or recreational purposes according to §1 of the German air traffic act [14]. For these systems a permission is required to fly, as specified in §16 of the air traffic regulations [15]. Therefore a permission is needed to operate a UAV for scientific purposes, irrespective of weight, noise emissions or degree of autonomy. The aircraft has to be in sight and under control of the pilot at all times, limiting the operational range and requiring a manual override for autonomous systems.

Furthermore a liability insurance, the consent of the land owner and a description of the system, used airspace and flight mission are required. The safety of the air traffic and the public may not be at risk, therefore restrictions regarding airspace used or time of day are imposed. When considering the place to fly an obvious choice is a model aircraft airfield. These

airfields have additional restrictions and limitations regarding airspace, altitude limit, temporal restrictions and weight limit , additional restrictions apply to internal combustion engines and rockets.

Further regulations apply to the radio connection. The 35 MHz band is allocated for model airplane remote control, although the 2.4 GHz band has by now become the standard. Although generally license-free, the maximum equivalent isotropical radiated power for both bands is limited to 100 mW, furthermore the components have to comply with CE legislation.

2.2 Relevant Aspects of Aerodynamics

2.2.1 Lift,Drag and Separation

The primary function of a wing or a control surface is to produce a force perpendicular to the flow to lift and control the aircraft. At the same time the drag has to be as small as possible to minimize the needed propulsion power. Usually the success of this optimization is expressed by the lift-to-drag ratio C_L/C_D. For maximizing the endurance of propeller-driven aircraft often also the endurance factor $C_L^{3/2}/C_D$ is used.

It has to be differentiated between the forces and coefficients on the whole aircraft, the wing, or a two-dimensional airfoil section. Lift and drag are closely interrelated by different flow phenomena shown in Figure 2.1.

For a given airfoil its theoretic lift coefficient is determined by the angle of attack towards the flow and its camber:

$$c_l = c_{l_\alpha} \, (\alpha - \alpha_0) \tag{2.1}$$

with the angle of attack at zero lift α_0 and the lift curve slope

$$c_{l_\alpha} = \frac{\mathrm{d}c_l}{\mathrm{d}\alpha} = 2\,\pi \tag{2.2}$$

from thin airfoil theory, for a finite wing this derivative is smaller due to the lift dependent self induced downwind. When separation occurs the above relation breaks down and the lift curve becomes nonlinear. Different types of separation can be distinguished:

- Trailing Edge: The separation begins at the trailing edge and moves forwards with increasing angles of attack. The slope of the lift curve gradually decreases until the flow is fully separated. The stall behavior is therefore very docile and this type of stall is aspired. It

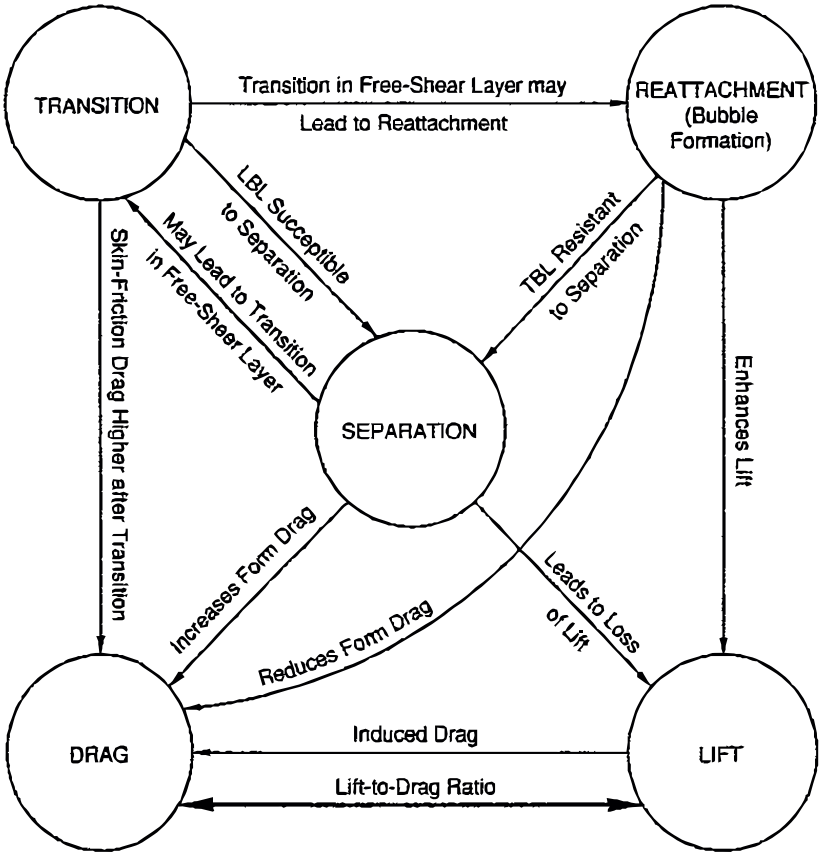

Figure 2.1: Overview of the interrelations between flow phenomenons on an airfoil (from [42]).

usually occurs on profiles of a thickness to chord ratio of $x/c \geq 15\%$, depending on the Reynolds number as shown in Figure 2.3.

- Leading Edge: Due to a relatively sharp leading edge a separation bubble occurs. The flow at the separation point is already unstable and transition occurs in the shear layer of the bubble [43]. The turbulent flow reattaches quickly, forming a short separation bubble. At higher angles of attack no reattachment is possible and the lift drops drastically. Therefore this stall behavior is dangerous and unwanted, it occurs at airfoils of $9\% \leq x/c \leq 12\%$.

- Thin airfoil: A longer separation bubble than in the above case is formed. The flow at the separation is still stable and transition occurs further downstream. The point of flow reattachment moves downstream with increasing angles of attack until the trailing edge is reached. The lift curve has a slight decline when the bubble begins to form and is rounded at the maximum lift. This type occurs at thin airfoils of $x/c \leq 6\%$.

- Combined: Combinations of the above mentioned types can occur, depending on the pressure distribution of the particular airfoil.

- Dynamic: The boundary layer reacts slowly to changes in the flow. Due to fast changes in angle of attack a much higher lift coefficient can be temporarily reached than in the static case. This occurs for example in flapping flight and helicopter and wind-turbine rotors, but is also relevant for fixed-wing aircraft due to gusts. The phenomenon is discussed by Leishman [70], amongst others.

On a wing the lift is reduced due to the three-dimensional flowfield with the trailing vortices at the wingtips. The airfoils and the wing twist have to be adjusted accordingly for good performance and flight behavior.

The drag of a wing D is composed of different contributions:

$$D = D_\mathrm{p} + D_\mathrm{f} + D_\mathrm{i} + D_\mathrm{w}, \tag{2.3}$$

where D_p is the pressure drag and D_f the skin friction drag. The pressure drag arises due to losses during the pressure recovery of the airfoil. Especially due to flow separation the pressure drag rises significantly. The friction drag is caused by the skin friction and depends on the gradient of the boundary layer velocity profile at the wall. For an airfoil in subsonic

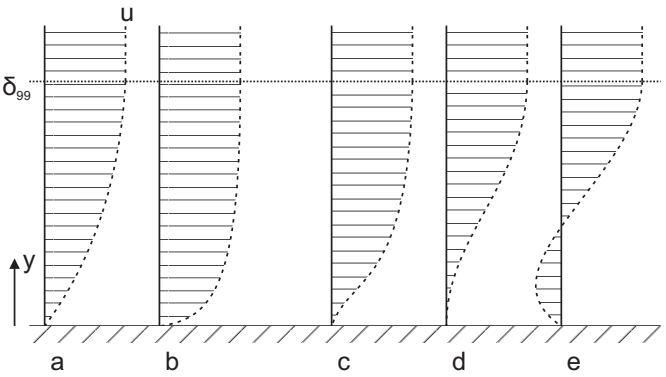

Figure 2.2: Boundary layer velocity profiles for laminar and turbulent flows and in vicinity of the separation point. A turbulent profile (b) has a much steeper velocity gradient at the wall and thus higher friction drag compared to a laminar (a) profile. It also contains more energy near the wall and is therefore less prone to separation. Due to adverse pressure gradients the flow is decelerated (c) until it flows backward (e) near the wall. At the separation point (d) the gradient at the wall is zero.

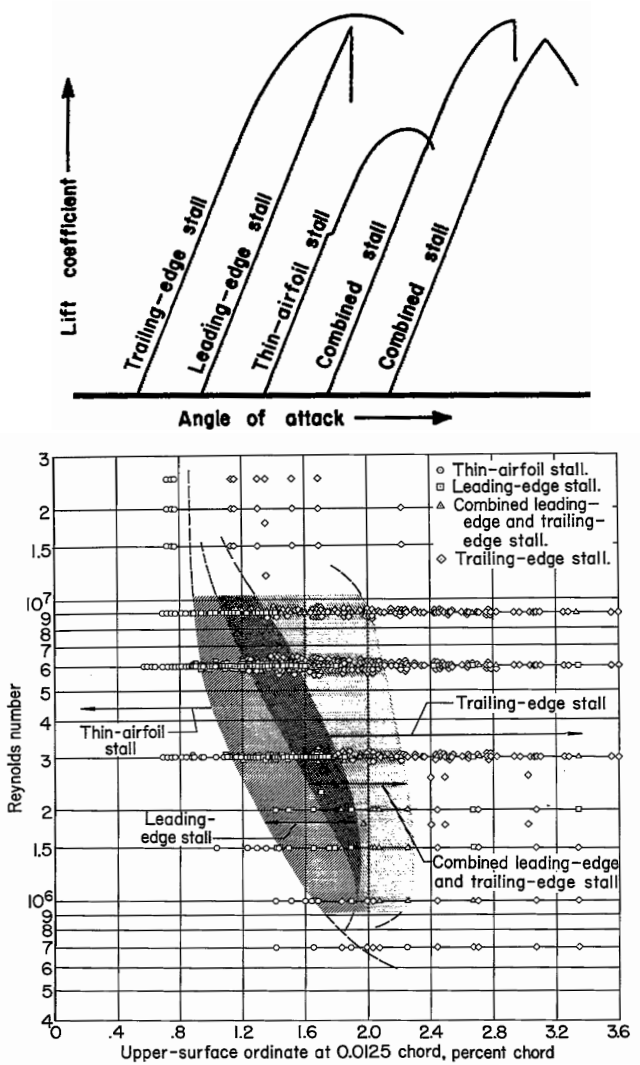

Figure 2.3: Lift curves for different stall types and occurrence depending on airfoil thickness and Reynolds number (from [44]). As a measure for the thickness, respectively the leading edge radius, the upper-surface ordinate at $0.0125\,x/c$ is used.

conditions only these two terms are relevant. When considering the three-dimensional flowfield of a finite wing the lift-induced drag D_i has to be included, the wave drag D_w occurs in trans- and supersonic cases.

A detailed account of aircraft aerodynamics is, for example, given by Anderson [3].

2.2.2 Low Reynolds Number Effects

At the relatively low Reynolds numbers typical for many UAVs, some special effects have to be considered. Most significant is the relatively large laminar region on the airfoil. As discussed in Section 2.2.1 laminar boundary layers are more prone to separation, below the critical Reynolds number Re_cr of the airfoil a laminar separation occurs. The separation limits the airfoils range of lift coefficients and corrupts its performance due to a high pressure drag, depicted in Figure 2.4. Above the airfoils critical Reynolds number the drag changes to a lesser extent, merely the drag due to friction decreases with increasing Reynolds number.

Airfoils designed and optimized for high Reynolds number applications can usually are inadequate for low Reynolds numbers, with a few exceptions such as the Clark Y. Low Reynolds number airfoils have to be specifically designed, with only a moderate increase in pressure over the airfoil to suppress separation. Selig [97, 98] and Lissaman [75] detail the design of such airfoils in the low 10^5 Reynolds number range. Computational tools for such a process are for example the inverse design routine of XFOIL [26] or the Eppler PROFIL code [33], although especially at very low Reynolds numbers subsequent wind tunnel testing is advisable. Commonly employed airfoils for model airplanes and UAVs include designs by Selig [97, 98] and Quabeck [85].

A key factor for the design is the control, in this case the promotion of transition. One method is the use of a transition ramp by which transition occurs over a thin separation bubble with a relatively small drag penalty. The ramp imposes a moderate, increasing rise in the pressure distribution, causing a short separation bubble which is moving with changing angle of attack. Airfoils for higher Reynolds number usually use a steeper, more abrupt pressure recovery, since the boundary layer is already turbulent. This can cause a long separation bubble or no reattachment at all at lower Reynolds numbers, with the according drag and lift penalties. A cruder method is the employment of a turbulator or trip, described in Section 2.3.3.1.

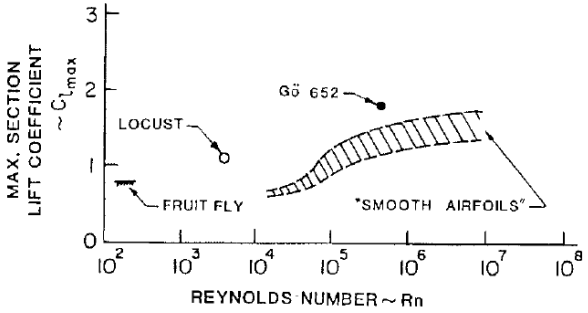

(a) Maximum lift coefficient

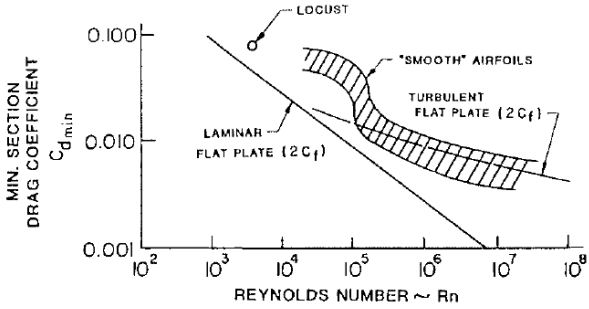

(b) Minimum drag coefficient

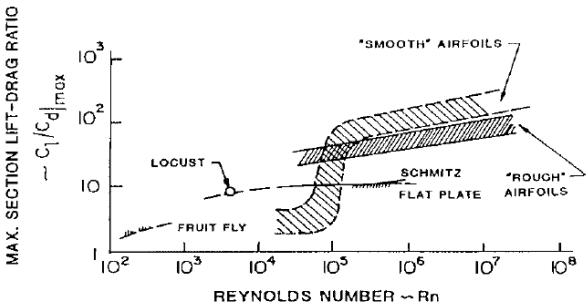

(c) Maximum lift-to-drag ratio

Figure 2.4: Maximum lift (a), minimum drag (b) and best lift-to-drag ratio (c) of generic airfoils against Reynolds number (from [77]).

2.3 Flow Control

2.3.1 Challenges and Historical Overview

Although flow control is a broad research area with many different applications, in this work the focus is on active flow control for use on aircraft. Generally, it can be distinguished between passive and active flow control. While passive devices such as vortex generators or drag-reducing surfaces are effective at all times, active flow control can be optimized for a special case. The advantage is that the device does not effect the flow negatively in off-design cases, for example additional drag caused by vortex generators during cruise flight.

The scientific foundation of flow control was provided by Prandtl [84] in 1904, by introducing the boundary layer theory and demonstrating active flow control by suction to delay separation. Although successful the field was not further pursued until the 1930s and the Second World War. In the following years the focus of the research was on laminar flow control, additionally vortex generators [48] and air jet actuators [5, 53] were investigated. In the 1960s the topic of circulation control became widespread, most frequently utilizing jet blowing on a Coanda [20] surface. In the following decades methods for drag reduction were researched using computational fluid dynamics and reactive flow control. In the 1990s zero net mass flux actuators, also called synthetic jets [100], and a few years later plasma actuators became widely investigated topics.

As can be seen in Figure 2.5 most current work is focused on flow control development and fundamentals, much more than on implementing and flight-testing. The actuators used are in most instances not particularly new or innovative, but are improvements to the concepts presented above. The currently most applied flow control devices are vortex generators to delay separation and thereby enhance lift. Other than that there are virtually no practical applications in non-research aircraft up to date, although flow control has been such an active research area for decades. The supposable reasons for this are manifold:

- Many flow control measures, although rated as successful in experiments are not or insufficiently effective for practical use and thereby irrelevant. An effect of the control only in narrow tolerances, such as a small range of angle of attack or a certain flight speed, can be deemed inadequate.
- The added weight and disadvantages during off-design flight regimes

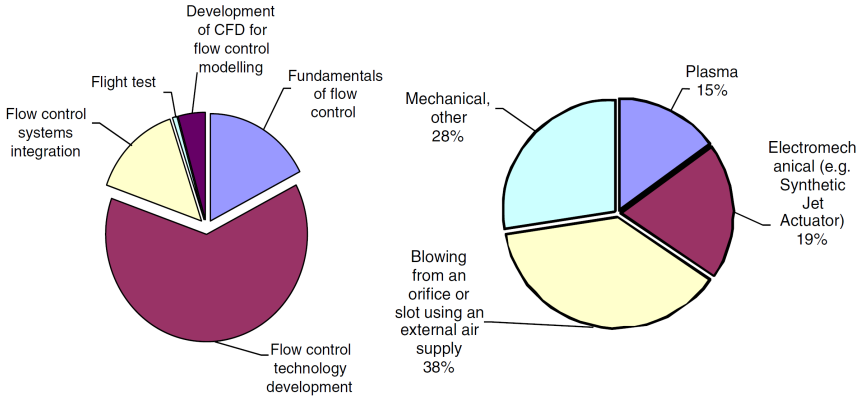

Figure 2.5: Flow control research activity broken down into type of research work undertaken and studied actuator, based on articles presented at the 3rd AIAA Flow Control Conference 2006 (from [22]).

can severely impact the efficiency of the flow control, as discussed in Section 2.3.5.

- The reliability of the whole system is often relevant to security, especially when considering high lift and manoeuvering control.
- The actuators have to function under challenging conditions, temperatures and pressures vary dramatically during a flight. Additionally, humidity, rain and ice may be encountered.
- Due to insects, hail or incautious handling on the ground actuators may be damaged, therefore they have to be as robust as possible.
- The manufacturing and maintenance can be challenging and thereby make the flow control non-economical.
- Due to the high costs, complex systems and long life cycles the aircraft industry in general is relatively conservative. New technologies and developments are adopted by and by, usually first in smaller aircraft.

A good and comprehensive overview of all aspects of the flow control research area can be found in [42], a detailed historic review up to the 1960s is given by Lachmann [69] and Wells [104].

2.3.2 Objectives

The usual superordinate objective of flow control applied to aircraft systems is to increase the lift-to-drag ratio L/D. There are obviously two approaches to this, either by increasing the lift L or by reducing the drag D. These two quantities are closely interrelated to each other by the phenomenons of transition, separation and reattachment as is discussed in Section 2.2.1. For applications also the indirect consequences are of importance, for example by minimized weight and thereby enhanced the lift-to-drag ratio, when substituting or enhancing conventional high lift devices or control surfaces.

2.3.2.1 Circulation Control

The produced lift L is dependent on the circulation, as given by the Kutta-Joukowski theorem:

$$L' = -\rho V \Gamma \tag{2.4}$$

For take-off and landing a high lift configuration is desirable to reduce the required velocities and thereby the take-off and landing distances. In this case flow control can be used to increase the maximum lift coefficient $C_{L,\max}$. The lift-to-drag ratio can usually be neglected during this phase of the flight, especially for landing, but has to be considered in terms of added drag and weight for the whole flight mission. The result has to be evaluated in comparison with other high lift configurations.

In the same way as for high lift, active flow control devices can also be used to substitute or enhance conventional control surfaces on aircraft. By selectively increasing or decreasing lift [94] or drag [23] at certain areas the aircraft can be manoeuvred. In this case the lift-to-drag ratio during the manoeuvre is again subordinate, if other advantages can be gained, for example a lower overall weight, higher safety or less radar reflection in military applications.

2.3.2.2 Drag Reduction

While pressure and lift-induced drag are defined by the geometric properties of the airfoil and fuselage respectively the wing planform the contribution to the drag due to skin-friction is a common target for flow control applications. It is usually influenced by delaying the laminar-turbulent transition, thereby reducing the skin friction drag.

However, a laminar boundary layer as shown in Figure 2.2 is more prone to separation, which leads to a dramatic increase in drag and a loss of lift. Therefore, an early transition can also be desired to either suppress a separation or help to reattach the flow. In the latter case the transition occurs within the separation bubble and by controlling the degree of the separation the lift can be influenced.

Sometime also an increase in drag is intended, for example at the wingtips for maneuvering around the yaw axis [23] or as landing aid to control the glideslope [30].

2.3.3 Device Types

In this section some relevant actuators and passive flow control devices are introduced briefly. The list is not exhaustive and limited to types directly or indirectly relevant to this work.

2.3.3.1 Passive

Vortex Generator Vortex generators are the most common flow control application in practical use and are used to delay separation by re-energizing the boundary layer. They are arranged in spanwise arrays and usually triangular, although other forms exist. Due to the flow-normal forcing a streamwise vortex is formed which transports high energy fluid into the boundary layer as shown in Figure 2.6. An array can be arranged to produce co- or counter-rotating vortices. Godard [46] discusses the optimum geometrical parameters, such as height, spacing and skew angle. Lin [74] reviews low-profile vortex generators, considerably smaller than the boundary layer thickness, which therefore promise less drag penalty.

Gurney Flap A gurney flap is a small flat plate perpendicular to the flow at the trailing edge, first described by Liebeck [72]. It has a length in the order of 1% chord length and increases the lift by shifting the rear stagnation point downward. The maximum lift coefficient is increased as well as the lift-to-drag ratio at high lift coefficients. Deployable microtabs similar to the Gurney flap are the subject of recent studies [19], using micro-electromechanical systems.

Turbulator Turbulators are used to force transition from laminar to turbulent flow, for example investigated by Gopalarathnam [47]. Since new

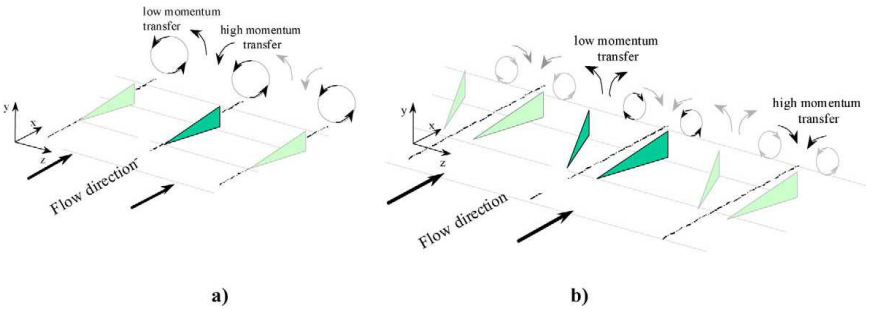

Figure 2.6: Co- (a) and counter-rotating (b) vortex generators (from [46]).

manufacturing processes enable the economical production of smooth surfaces natural laminar flow airfoils become more prevalent. Turbulators are usually used in places where laminar separation would otherwise occur or in front of control surfaces to avoid separation at high deflections. Several forms exist, such as zigzag trip or sandpaper strips with a height dependent on the local boundary layer thickness. This method is also often used in flow control experiments at low Reynolds numbers to emulate the turbulent boundary layer of the targeted high Reynolds number application. Conversely it also assures that the flow control effect measured is not due to the actuator working as a turbulator, ineffective for the target application.

2.3.3.2 Fluidic

Jet Jet actuators employ steady or unsteady blowing of fluid from the wall into the flow, either from bores or slots. Due to the normal or at obtuse angles to the wall ejected fluid the mixing rate of the boundary layer is increased, delaying separation.

Another approach is tangential blowing to enrich the shear layer with high momentum fluid. Additionally the Coanda [20] effect can be used, for example on leading edges of flaps or on rounded trailing edges. Thereby the flowfield can be substantially altered and very high maximum lift coefficients are reached [31].

Pulsed jets can be more efficient and also more effective when driven at an appropriate frequency, interacting with the instabilities in the flow [96].

Synthetic Jet Synthetic jets are zero mass-flux devices are described in [45]. In contrast to standard jet actuators, the fluid is sucked back into the actuator during the relaxation phase. Different actuators such as surface or cavity mounted piezo elements, speakers and others are described in [91].

2.3.3.3 Electro- and Magnetohydrodynamic

Some actuators utilize electro- or magnetohydrodynamic forces of an according field on a fluid. In magnetohydrodynamic actuators the Lorentz force is used, in electrohydrodynamic the Coulomb force. Additionally, effects from Joule heating can play a role. The fluid present has to be electrically conductive, which is not the case for air under normal atmospheric conditions. With the help of different methods a partly or fully ionized plasma can be produced, thus making the air susceptible to electric and magnetic fields. This can be accomplished for instance by corona, glow, arc or spark electric discharges, microwaves, lasers or thermal heating.

The advantage of electrohydrodynamic actuators is the use of a single high voltage field to generate a plasma and apply a force to it simultaneously. Therefore the design of the actuator is very simple, requiring only at least two electrodes and a power supply.

The different plasma regimes are shown in Figure 2.7 and explained in detail by Kriegseis [62]. At low voltages a dark discharge occurs, with corona discharges at local irregularities in the field. Above the breakdown voltage a glow discharge develops. When further increasing the voltage the transition to an arc-discharge occurs.

DBD plasma actuators operate in the glow discharge regime and produce a weakly-ionized, non-equilibrium plasma at near-atmospheric pressures. The actuators used in this work are described in detail in Section 2.4.

2.3.4 Control Strategies

Different control strategies can be applied for active flow control, as shown in Figure 2.8, in general predetermined and reactive strategies can be distinguished.

In the predetermined case the actuator is active regardless of the state of the flow. No sensors and controllers are needed, but the efficiency may be suboptimal.

Reactive control on the other hand can be further divided into feed-forward and feedback strategies. For feed-forward control a significant flow variable is measured at an upstream location and the actuator controlled

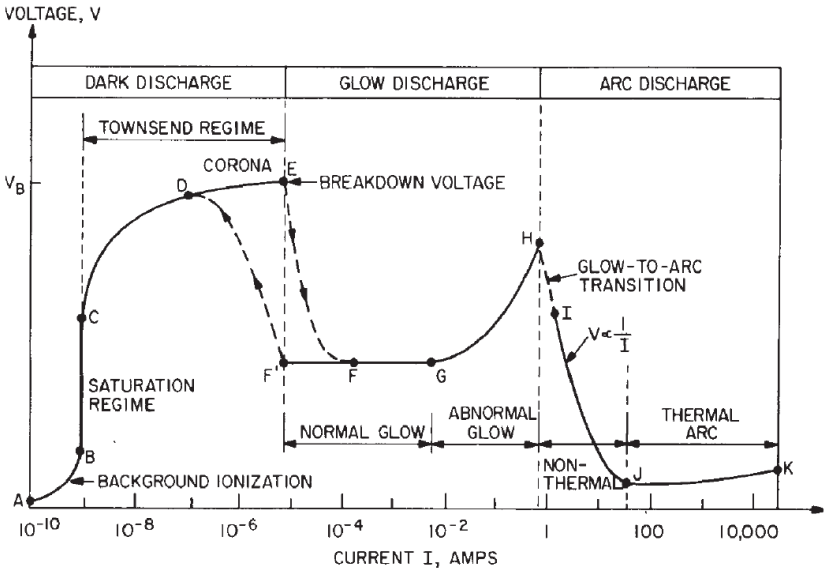

Figure 2.7: Discharge regimes of the classical DC electric discharge (from [87]).

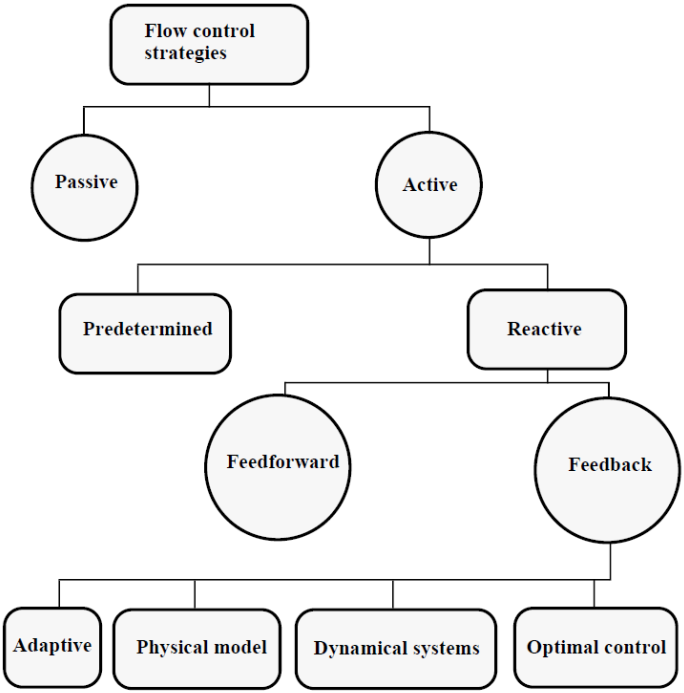

Figure 2.8: Classification of flow control strategies (from [42]).

according to predefined control laws. In feedback systems a sensor directly measures the controlled variable downstream of the actuator. Different controllers can be used, such as adaptive or model-based schemes, described in detail by Gad-el-Hak [42].

2.3.5 Efficiency Considerations

Specifying an efficiency for a flow control effort is not straightforward, since the whole system has to be considered. In general the efficiency can be defined as the ratio of output power P_O to input power P_I:

$$\eta = \frac{P_O}{P_I}. \tag{2.5}$$

The output power in this case is the savings due to flow control, the input power of the flow control system itself can relatively easy be quantified. For a DBD plasma actuator the efficiencies of the individual steps from input power to fluid mechanic power are discussed in Section 2.4.5.

However, when taking into regard the impact of the flow control on the whole aircraft, several further aspects have to be considered. An obvious approach is the consideration of the change in the lift-to-drag ratio of the aircraft. An aerodynamic figure of merit for flow control applications based on this is proposed by Seifert [95]:

$$AFM_1 = \frac{V\,L}{(V\,D + P_\mathrm{I})\,\left(\frac{L}{D}\right)_\mathrm{bl}}, \tag{2.6}$$

where P_I is the power input provided to the flow control system.

A further consideration is the added weight of the flow control system, respectively the net weight change ΔG when replacing conventional systems, which results in a changed lift and therefore drag.Thus a second figure of merit is proposed in [91]:

$$AFM_2 = \frac{V\,(L - \Delta G)}{(V\,D + P_\mathrm{I})\,\left(\frac{L}{D}\right)_\mathrm{bl}}. \tag{2.7}$$

A further addition to this definition can be made by applying a factor μ_PL to the weight change, taking in account the ratio between gross weight of the aircraft and usable payload:

$$AFM_3 = \frac{V\,\left(L - \frac{\Delta G}{\mu_\mathrm{PL}}\right)}{(V\,D + P_\mathrm{I})\,\left(\frac{L}{D}\right)_\mathrm{bl}}. \tag{2.8}$$

However, the approaches described above only consider the instantaneous efficiency during flow control operation. Rather the typical flight mission profile and the ratio of active control during it has to be considered. The overall efficiency in this case has to be a comparison of overall input energy to accomplish this particular mission, an universally valid value can therefore not be specified.

2.4 DBD Plasma Actuators

2.4.1 Design and Principle of Operation

A dielectric barrier discharge (DBD) plasma actuator consists of two electrodes separated by a dielectric as depicted in Figure 2.9. The grounded electrode is covered by the dielectric, the high voltage electrode is above it and staggered towards the grounded. Different materials can be used for the construction of an actuator:

- Electrodes: A conductive material has to be used, most often an adhesive copper tape. More complicated electrode geometries can be produced by chemical etching or metal spraying. Alternatively a wire can be used as exposed electrode.
- Dielectric: Most often polyimide is used, in form of a Kapton adhesive tape or Cirlex sheets. In general the material has to be homogeneous and of constant thickness to achieve a homogeneous distribution of the plasma.
- Surface: The surface has to be of a non-conducting material, such as acrylic glass (PMMA) or glass-fibre reinforced plastic (GRP). To improve the flow quality the actuator can be placed in a groove in the surface.

Many actuators are made by hand from copper and Kapton tapes. Although a fast and simple method, it is relatively imprecise.

By supplying a high alternating voltage with a peak-to-peak voltage V_{pl} in the order of kV and a frequency f_{pl} in the order of kHz a weakly ionized plasma is generated. Due to the electric field present the ionized particles experience a force, resulting in an acceleration of the whole fluid in wall-normal direction due to particle collisions. Although the force field reverses its orientation with the supplied AC voltage a net acceleration from upper towards lower electrode occurs and a wall-jet develops. The details and mechanism of the momentum transfer are not yet fully understood and are being discussed [4, 12, 32, 35, 36, 73, 83].

2.4.2 Induced Wall Jet and Impact on Flow

Fluid is sucked into the plasma region from before and above the actuator and accelerated, resulting in a wall-parallel jet. The jet broadens while

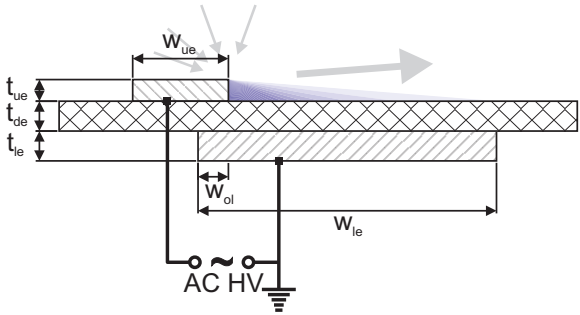

Figure 2.9: Cross section of a generic single DBD plasma actuator, consisting of upper electrode (ue), dielectric barrier (de) and lower electrode (le). The electrodes can have a slight overlap w_{ol} or gap between them. Due to a high voltage AC supplied to the electrodes a plasma is created and the fluid accelerated in wall-normal direction.

moving away from the actuator and moves away from the wall, as shown in Figure 2.10. The flowfield in the vicinity of the actuator during activation, operation and deactivation are described in depth by Kriegseis [63].

The force and thrust production was examined by Kriegseis [64, 68], based on PIV measurements. A part of the force applied to the fluid is consumed by wall-friction due to the high velocity gradient at the surface, so the net thrust is considerably smaller than the force transferred to the flow.

If the actuator operates in non-quiescent air, the added momentum alters the boundary layer. Depending on the actuator momentum and the incoming flow directly behind the actuator an increase or even a local maximum occurs in the velocity profile near the wall, resulting in a fuller profile further downstream. This delays separation and has a stabilizing effect on a laminar boundary layer, as discussed by Duchmann [29].

When operating the actuator in an unsteady mode, i.e. pulsed, instabilities of the flow can be utilized for separation control. In this case the additional parameters duty-cycle and burst frequency are used to describe the actuation. Benard [8, 9] showed that for leading-edge separation an actuator pulsed at certain frequencies can result in a more effective and efficient control result. For transition control pulsed actuation can be used for active wave cancelation as discussed by Forte [38].

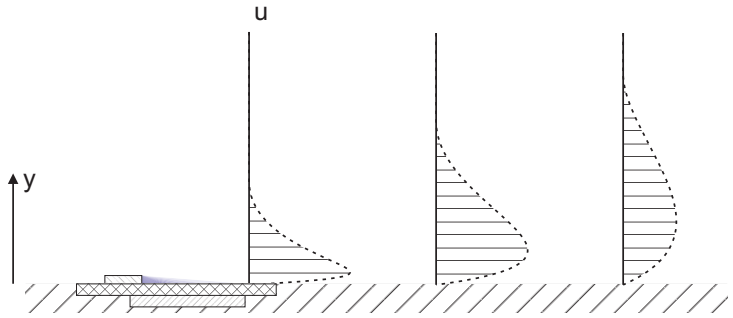

Figure 2.10: Wall jet velocity profiles behind a DBD plasma actuator in quiescent air. The jet detaches from the wall and broadens while moving away from the actuator.

A thorough review of plasma actuators, their electrical parameters, produced force and their use as flow control devices is given in [62].

2.4.3 Limitations and Practical Considerations

Although DBD plasma actuators have many advantages such as almost instantaneous reaction time, relative ease of installation and no moving parts, the produced force and influence on the flow is comparably small. Wilke [106] proved that the velocity of the wall-jet of a single DBD plasma actuator is limited by physical constraints. Therefore the application at higher Reynolds numbers is only supposable by exploiting flow instabilities or using other secondary mechanisms such as vortex generation.

For flight applications the changing conditions in the atmosphere have to be considered. Pressure, temperature and humidity change drastically with altitude [55], weather conditions and locally, i.e. when flying through a cloud.

The most obvious parameter is the velocity of the incoming airflow. To characterize the impact on the actuator, Kriegseis [65] defines a relative performance dependent on the Mach number Ma

$$\Pi_{P_{\mathrm{PA}}} = \frac{P_{\mathrm{PA}}\,(Ma)}{P_{\mathrm{PA}}|_{Ma=0}}, \tag{2.9}$$

in this case with the plasma-actuator power P_{PA}, and an according relative performance drop

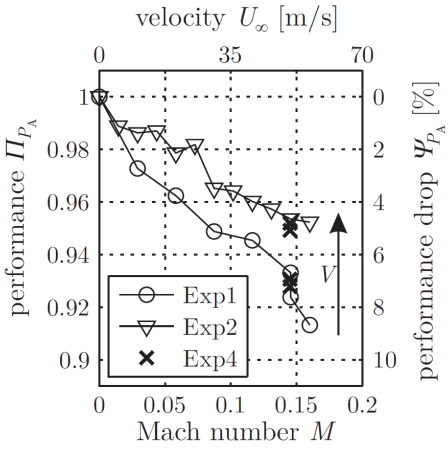

Figure 2.11: Relative performance and performance drop of a plasma actuator due to airflow, based on actuator power (from [65]). Depicted are the results from three experiments at different voltages and plasma frequencies.

$$\Psi_{P_{\mathrm{PA}}} = 1 - \Pi_{P_{\mathrm{PA}}}. \tag{2.10}$$

As can be seen in Figure 2.11 the performance drop at the free-stream velocities relevant to this work is in the order of 1 to 5%.

Benard [6] investigated the impact of ambient pressure on the electrical characteristics and produced jet of DBD plasma actuators. He found an increase of the plasma region for greatly decreased pressures. The wall-jet has a fuller velocity profile with a less distinct peak for pressures down to 40% of the standard pressure. An optimum can be found in Figure 2.12 between 40% and 60% standard pressure, below this pressure the airflow of the actuator is reduced.

The influence of high temperatures was examined by Versailles [103]. He found a higher net force production for higher temperatures and explains this by the reduced air density. Although only high temperatures were measured it can be assumed from Figure 2.13 that at lower temperatures, typical of higher altitudes, a smaller force can be expected.

Another environment variable is the humidity. Benard [7] investigated the influence of relative humidity, Figure 2.14 shows the mass flow rate

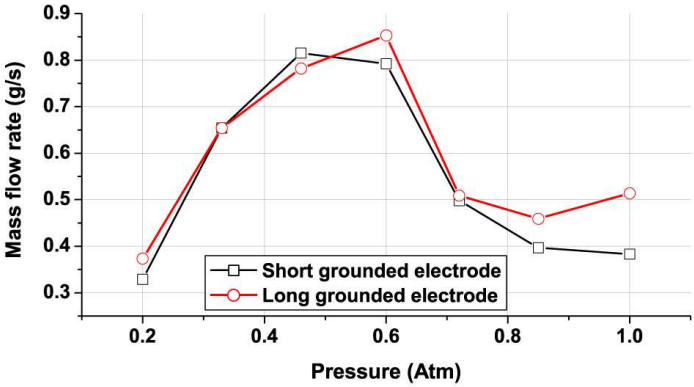

Figure 2.12: Impact of the ambient pressure on the airflow produced by a DBD plasma actuator (from [6]).

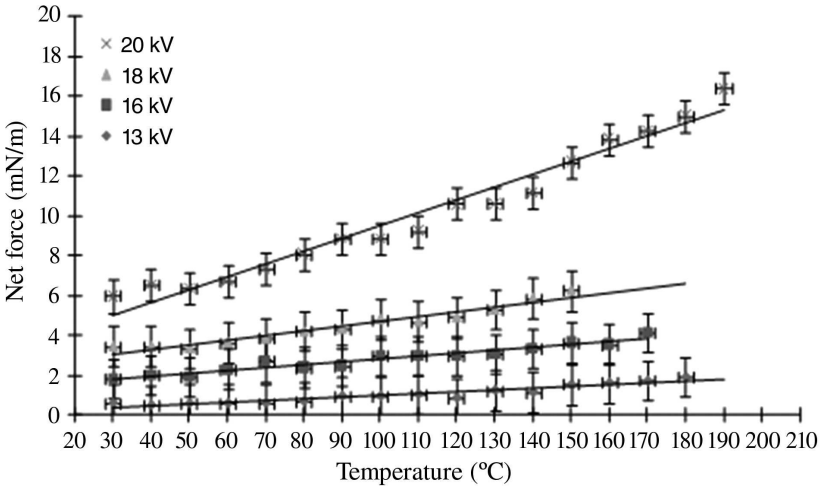

Figure 2.13: Impact of the ambient temperature on the force produced by a DBD plasma actuator (from [103]).

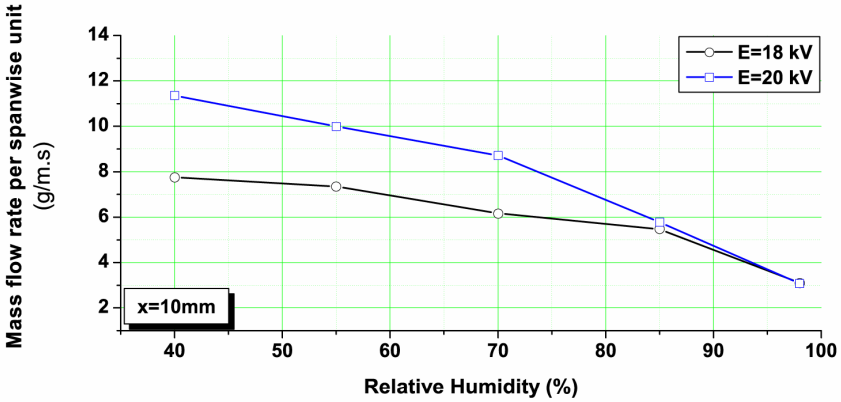

Figure 2.14: Impact of the ambient humidity on the mass flow rate produced by a DBD plasma actuator (from [7]). The rate was measured 10 mm downstream of the actuator.

at different streamwise positions behind an actuator. It can be seen that it is lower at higher humidities, at very high humidities of about 98% it drops significantly, possibly due to small droplets or condensation on the actuator. In the case of a DBD actuator mounted on a wing the relative humidity changes due to the pressure distribution of the wing. In humid air this can lead to condensation on the suction side of the wing. This effect as well as flight through clouds and precipitation could lead to liquid on the actuator surface and result in a poor effectiveness or breakdown.

A related practical problem is the impact of insects on the wing, which could cause short circuits and damages to the actuator surface. Other problems and dangers include electrocution, the emission of ozone and other potentially harmful gases, and electromagnetic interference with other systems, as discussed in Section 4.3.5 for the UAV. Another consideration is the relatively short durability of the actuators, depending on the used materials and applied voltage. Especially the dielectric material is prone to deterioration. Therefore also the electric parameters of the actuator change over time and the input should be adjusted accordingly, if possible.

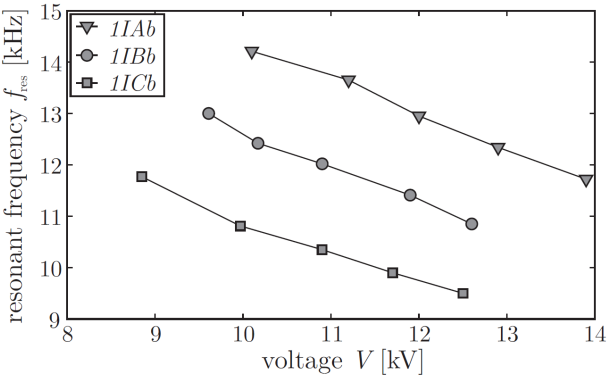

Figure 2.15: Resonance frequency for three different DBD plasma actuators, depending on applied voltage (from [62]).

2.4.4 High Voltage Supply

Different types of high voltage generators can be used to supply the actuators. Commonly used generators consist of a signal generator, producing a pulsed voltage waveform, and an amplifier, transforming the signal to a high voltage output.

Simplified, the inductance L of the amplifier and the capacitance C of the DBD plasma actuator form a LC circuit, with a resonance frequency of

$$f_{\text{res}} = \frac{1}{2\,\pi\,\sqrt{L\,C}}. \tag{2.11}$$

Depending on the voltage the extent of the plasma changes and thereby the capacitance of the actuator, as discussed by Kriegseis [62]. A higher voltage therefore results in a lower resonance frequency as shown in Figure 2.15. To maximize the actuator input power and efficiency an operation near the resonance frequency is favorable and the plasma frequency has to be adjusted accordingly.

The electrical power consumed by the actuator was found to be dependent upon voltage and frequency in experiments by Kriegseis [62]:

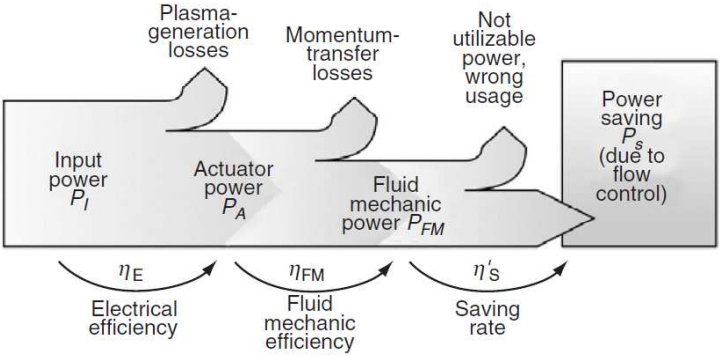

Figure 2.16: Power flow, losses and efficiencies of a DBD plasma actuator (from [66]).

$$P_{\mathrm{PA}} \propto V_{\mathrm{pl}}^{\frac{7}{2}} \tag{2.12}$$

$$P_{\mathrm{PA}} \propto f_{\mathrm{pl}}^{\frac{3}{2}} \tag{2.13}$$

He thus proposes a scaling number which is constant for a particular actuator configuration:

$$\Theta_{\mathrm{PA}} = \frac{P_{\mathrm{PA}}}{l_{\mathrm{PA}}\, f_{\mathrm{pl}}^{\frac{3}{2}}\, V_{\mathrm{pl}}^{\frac{7}{2}}} \tag{2.14}$$

2.4.5 Efficiency

The overall efficiency of a flow control system can only be defined by looking at the complete system, in this case the aircraft and its flight mission. Nonetheless the efficiencies of the single conversions in the flow control system can be specified [66] according to Figure 2.16.

The input power P_{I} is supplied by the batteries to the high voltage generator. Due to losses in the transformer and during plasma generation the electrical power at the actuator P_{PA} is smaller. The according electrical efficiency is

$$\eta_{\mathrm{E}} = \frac{P_{\mathrm{PA}}}{P_{\mathrm{I}}} \tag{2.15}$$

and is dependent on the high voltage generator, actuator, especially the dielectric material, and matching of the impedance of the components. For an actuator operated at the resonance frequency it can be assumed to be around 60% [28].

The fluid-mechanic kinetic output power P_{FM} is further reduced due to thermal radiation, chemical reactions and light and sound emissions. The fluid-mechanic efficiency is given by

$$\eta_{\mathrm{FM}} = \frac{P_{\mathrm{FM}}}{P_{\mathrm{PA}}} \tag{2.16}$$

or non-dimensionless with the produced thrust T

$$\eta^{*}_{\mathrm{FM}} = \frac{T}{P_{\mathrm{PA}}}, \tag{2.17}$$

since the fluid-mechanic power can be difficult to determine.

The result of the flow control effort can be evaluated by the saved power P_{S}. As already discussed in Section 2.3.5 this quantity can only be specified with respect to the overall aircraft system. The saving rate

$$\eta^{'}_{\mathrm{S}} = \frac{P_{\mathrm{S}}}{P_{\mathrm{FM}}} \tag{2.18}$$

is the factor by which the savings exceed the fluid-mechanic energy input and can be maximized by optimizing the position and timing of the actuation.

The overall efficiency

$$\eta^{'}_{\mathrm{fc}} = \eta_{\mathrm{E}}\,\eta_{\mathrm{FM}}\,\eta^{'}_{\mathrm{S}} = \frac{P_{\mathrm{S}}}{P_{\mathrm{I}}} \tag{2.19}$$

describes the efficiency of the overall system and should be greater than unity for successful flow control. At the current state of the art this objective is not reached with DBD plasma actuators. Duchmann [28], for example, measured a drag reduction of 11% of the actuator power P_{PA}, due to stabilization of the boundary layer in free-flight experiments.

2.4.6 Actuator Configurations for Separation Control

2.4.6.1 SDBD Actuators

The SDBD actuator reinforces the boundary layer by directly introducing energy near the wall. Although the momentum is comparatively small,

successful separation control experiments were conducted at low Reynolds numbers. To achieve the best effect the position of the actuator has to be directly in front of the separation line.

To increase the effect a pulsed actuation is suitable [9]. When the according frequency is used instabilities are excited and vortices produced. They increase the mixing of the boundary layer and thereby transport high energy fluid to regions near the wall receptive to separation.

2.4.6.2 MDBD Actuator

Single DBD plasma actuators are limited in terms of induced velocity and the area affected by the actuation. Since the actuators can not be arbitrarily scaled, a solution to both limitations are actuator arrays. However, when creating an array with conventional actuators, the interaction between them limits their minimum spatial separation. During the PLASMAERO project several solutions to this problem were investigated, as described in [80].

In a multi-DBD setup several actuators are placed as an array with the use of additional, unconnected electrodes with a floating potential, as depicted in Figure 2.17. These floating electrodes are supposed to act as either grounded or high-voltage electrode, depending on the phase. The effect of interference between the actuators and counterflow is minimized in this configuration. The cumulative effect of the actuators enables induced velocities unobtainable by single DBD actuators [106]. The induced velocities seem to approach a saturated state over the extent of the actuator, especially visible for low voltages.

During the project also the characteristics of a serrated exposed electrode as pictured in Figure 2.18 were investigated [11]. It was found that the discharge starts a lower voltage compared to a smooth electrode, beginning at the tip of each sawtooth. Higher induced velocities are achieved, especially at low voltages.

2.4.6.3 VGDBD Actuators

In order for the actuators to control separation, energy has to be introduced to the boundary layer near to the surface. An indirect way to achieve this is the creation of streamwise vortices by streamwise oriented actuators, similar to conventional vortex generators. The spanwise forcing creates a crossflow near the surface, inducing a vortex. A short distance downstream of the actuator the vortex develops further, until it degenerates due to

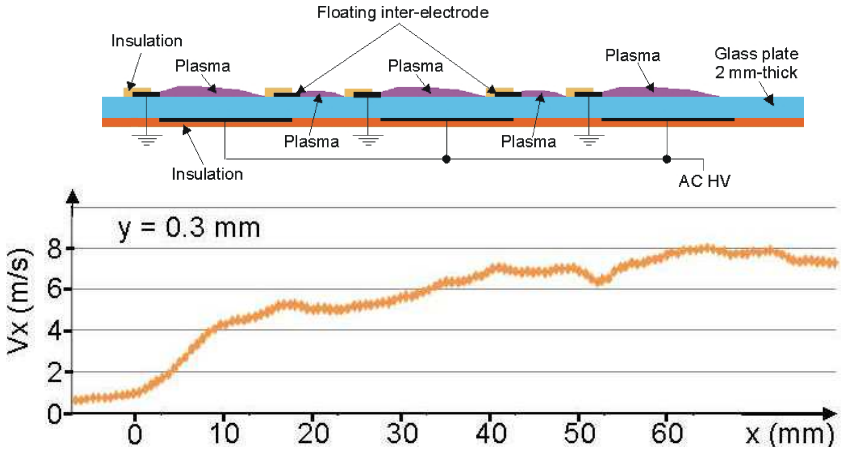

Figure 2.17: Schematic of a floating electrode MDBD plasma actuator array and mean wall-jet velocity achieved (from [80]). The velocity was measured 3 mm above the actuator at a voltage of $V_{\mathrm{pl}} = 26$ kV with a frequency of $f_{\mathrm{pl}} = 1.5$ kHz.

friction and finally dissipates. High velocity fluid from outside the boundary layer is brought to the near-wall region by this vortex, as shown in Figure 2.19.

To achieve an effect along a larger spanwise extent of the wing several of these actuators are combined as an array. Different configurations are conceivable, in the co-rotating case all actuators produce a force in the same direction, resulting in an array of co-rotating vortices. Counter-rotating vortices are accordingly achieved by actuators forcing in alternating directions. The created vortices interact and influence each other, additional parameters are the angle between flow and actuator, the spacing between actuators and their length. Jukes [59] found, that a counter-rotating configuration orientated perpendicular to the flow is most effective.

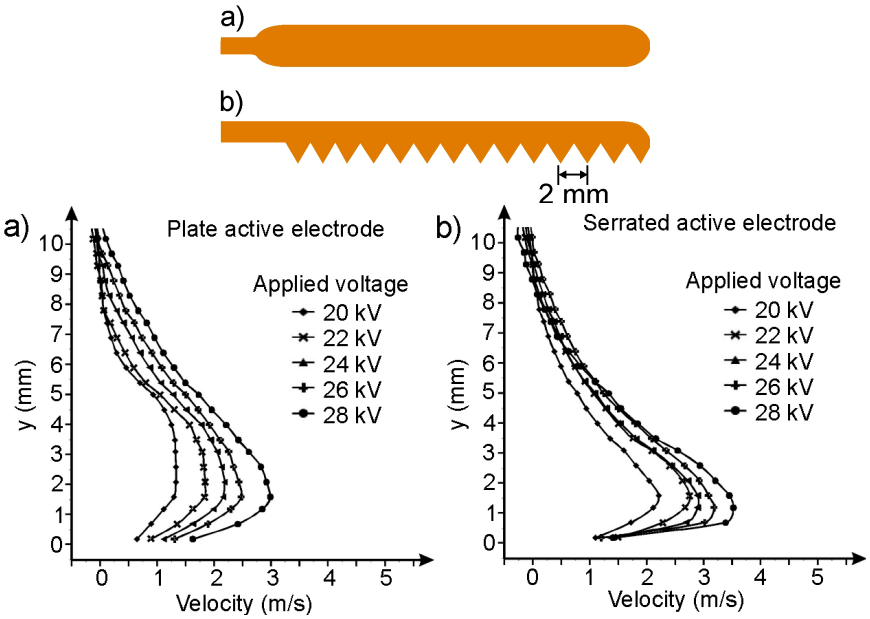

Figure 2.18: Smooth (a) and serrated (b) electrode and their induced wall-jet velocities (from [80]).

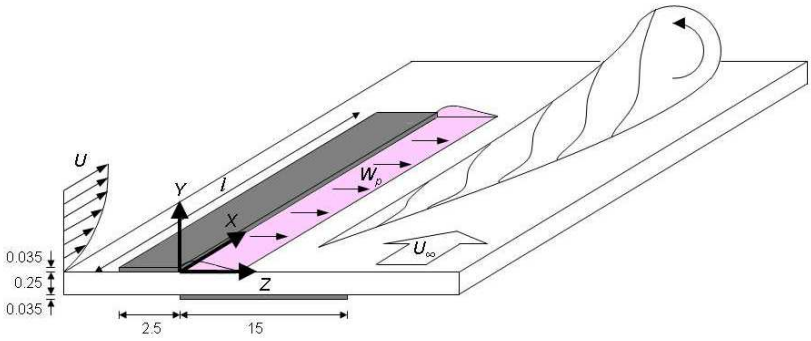

Figure 2.19: Vortex generated by a single DBD vortex generator (from [80]).

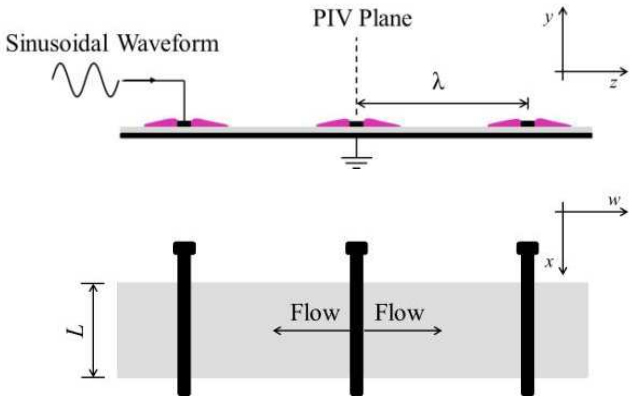

Figure 2.20: Front and plan schematic view of a counter-rotating DBD vortex generator array (from [105]).

3 Pre-Design

3.1 Objectives and Constraints

3.1.1 Objectives defined by the PLASMAERO Project

Since the UAV was developed as part of the PLASMAERO research project, different objectives and limitations were stipulated. The statement of requirements provided by the projects Description of Work [1] defines the following objectives:

- Develop, build and operate a UAV flight platform for subsonic flight experiments in realistic conditions.
  - Design and develop the new 2 m span UAV including the design flight speeds and propelling system.
  - Integrate a comprehensive flight-data logging system, to record all available flight data, such as velocity, height and angles.
  - A free programmable control system will be on board which can operate the HV-generators and acquires data for closed-loop control circuits. The control system will be used to develop an automated separation control system and an automated system for flight stabilization against gusts using DBD plasma actuators as flow control devices.
  - The UAV will be tested in the large wind tunnel of the TU Darmstadt during the development phase of the UAV and of the control systems. This ensures safe and quick development without dependency on weather conditions or with the danger of flight accidents with newly developed control systems.
  - The entire UAV including the operator and pilot will be available for all participants of PLASMAERO to develop their own flow control systems for in-flight experiments.
- Integrate the necessary power supplies for all the actuators to be tested.

  - Develop the second generation of the miniature HV-generator. High-voltage switches for the operation of different surface plasma actuators on each wing will be designed and developed by TU Darmstadt in collaboration with the partners.
  - The plane will have two HV-generators, one built inside each wing. The high voltage generators will be capable of switching between several plasma actuators on each side (e.g: pressure and suction side, leading edge, etc) which yields maximal flexibility for the circulation control necessary for manoeuvring.
  - Wind tunnel tests will be performed at TU Darmstadt to verify the effectiveness of plasma actuators on different aerodynamic profiles at the given chord lengths. An effective separation control as well as an effective circulation control on the chosen profile should be guaranteed during this phase.

- Validate and integrate the best flow control concepts on real flight platform condition.
  - The aerodynamic flow control systems with the plasma actuators and the closed-loop control systems will be applied on the previously developed wing.
  - Different actuators and different control protocols developed by the partners in the work packages WP1 (Plasma devices, investigations, developments and improvements), WP2 (Physical modeling, coupling and fluid dynamic simulations) and WP3 (Wind tunnel tests investigations for flow control), will be integrated in the flight platform and in-flight experiments.
  - Work will be focused on the development of in-flight closed-loop control strategies for the application of plasma actuators as separation control device and as rudder replacement.
  - Strategies and computer programs will be developed for the following tasks: Detection and automated prevention of flow separation, automated optimization of the operating parameters for the separation-control, circulation control for rudder-less manoeuvring and flight-stabilization against wind and gusts.

- Measure the energy balance (power consumed by actuator vs. lift and lift / drag increase).

- Give the conclusions and perspectives in flow control by plasmas.

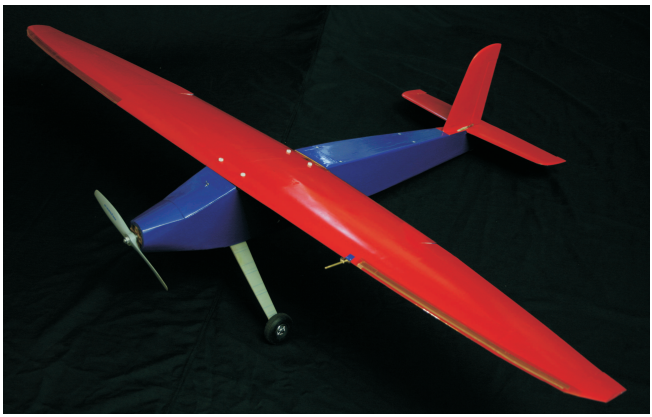

Figure 3.1: Previous UAV at TU Darmstadt designed and built by Frey [39].

3.1.2 Operating Experience from Previous UAV

At the TU Darmstadt a UAV was built in 2008 [39, 51] for plasma actuator experiments, with the objective to demonstrate the feasibility of plasma flow control in real flight conditions. The plane has a wingspan of 1800 mm, a flying mass of about 4 kg and a mean chord of about 180 mm. Minimum Reynolds numbers of around 130.000 are reached. The aircraft is powered by an electric motor in the front of the fuselage and can carry one Minipuls 0 high voltage generator. Details concerning the design, the construction and the conducted experiments can be found in [39]. The Minipuls 0 HV generator is the forerunner model of the Minipuls 0.1 generator described in Section 4.3.4.1.

This UAV was used for separation control experiments with DBD plasma actuators. Actuators were applied over a total of 900 mm wingspan on both sides. The stall speeds for the unactuated and actuated cases were measured using a pitot-static tube on the the left wing. The data was recorded by a small Unilog system designed for model aircraft use.

The critical aspects and the need for improvements for the new UAV become clear when looking at the restrictions and problems with the existing UAV:

- The electric system, especially the measurement equipment, was prone to interference from the plasma actuation. Several electric motors,

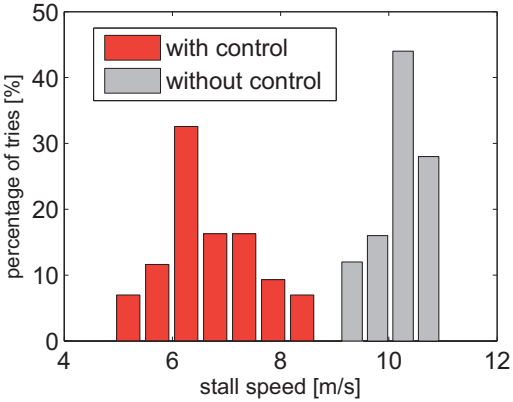

Figure 3.2: Stall speed measurement results with and without DBD plasma actuator on previous UAV (from [51]).

batteries and data recording devices were heavily affected or destroyed. It can be assumed that these problems were in large part due to the proximity to the high voltage generators and their cables.

- The measurements results show a high variation. This can be explained by two factors: Gusts, and the influence of the pilot. Gusts can only be avoided by flying in relatively calm air, usually in the morning and evening. However, the influence of the pilot can be ruled out by using a system for autonomous control for the experimental manoeuvres. Additionally, due to the high angles of attack and the pitch velocity during stall the measurement data was imprecise and difficult to evaluate.

- During the project different flow control concepts and high voltage generators are to be developed. The use on the existing UAV is not possible due to its restricted payload and available space as well as the construction of the wing as one piece. For the use with different actuator and flow configurations a bigger and more modular platform is needed.

3.2 Conceptual Design

3.2.1 Size

A big challenge in conducting flight experiments with small UAVs is the very limited payload and usable space. In addition to the actuators and their power supply systems the measurement equipment has to be carried. Due to the small size and low flight speeds of the plane the weight is reduced considerably. The provided lift scales with wing area, respectively the square of the chord length c for constant aspect ratio, and flight speed:

$$L \sim c^2 V^2 \tag{3.1}$$

On the other hand the control authority of the actuator declines with increasing chord length and flight velocities. Therefore a compromise between payload and control authority has to be found, ensuring the aptitude of the aircraft for successful flow control experiments.

3.2.2 Modularity

Due to the unknown constraints regarding the configuration of the experiments, power supplies or airfoils of the project partners the layout has to be as modular as possible. A modular wing concept to facilitate the use of different airfoils has to be used. This can for example be achieved by a wing glove [27], though this adds weight and increases the Reynolds number for the experiments. For this work a wing with interchangeable sections was chosen, the flow control sections can be exchanged to feature different airfoil and actuator setups.

Furthermore a spacious fuselage is desired to accommodate different payloads, such as high voltage generators, batteries and measurement equipment. A long fuselage is beneficial to move the payload so that an acceptable center of gravity can be adjusted.

A self-reliance and separation of the plasma actuation system from other systems was pursued to simplify the evaluation of the flow control effort and the transfer to other aircraft and applications.

3.2.3 High Voltage Generator Placement

When looking at the different requirements stated above, it can be seen that they are ambiguous and partially contradictory. For the requested installation of the high voltage generators in the wing the used airfoil has

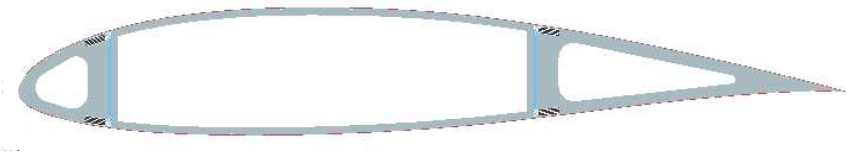

Figure 3.3: Sketch of an airfoil with a two-spar design for accommodation of a high voltage generator inside the wing.

to provide a sufficient cross section. By using a two-spar design as depicted in Figure 3.3 the available cross section can be maximized. The typical maximum airfoil thickness is about $t = 15\%\, c$, yielding an approximate cross section of $10\%\, c$ height and a width of $50\%\, c$.

The Minipuls 0 high voltage generator has a height of 22 and 30 mm and a width of 72 and 79 mm, for high voltage and signal generator board respectively. Therefore a wing with a chord length $c \geq 300$ mm would be required to house the generators. Since the generators to be used were not yet developed during this phase of the design even larger chord lengths might be required.

For a first approximation a chord length of 400 mm was assumed, a rectangular wing with a span of $b = 2000$ mm would thus have an aspect ratio of

$$\Lambda = \frac{c^2}{S} = 5. \tag{3.2}$$

For such a low ratio the flow around the wing would be highly three-dimensional. Therefore two concepts were devised and are compared in the following. The first is a 3.5 m span version with 400 mm chord length, with a half model for wind tunnel testing. The second features 2 m span and 300 mm chord length, with the high voltage generators installed in the fuselage.

3.2.4 Weights, Speeds and Reynolds Numbers

A rough estimation of the anticipated payload for 2 and 3.5 m span versions is given in Table 3.1. The values for the structural weight were estimated based on existing aircraft of comparable size with an additional weight penalty due to the interchangeable experiments. The weight of the propulsion system is dependent on the gross weight of the aircraft and was

Table 3.1: Estimation of the anticipated mass of the individual components. The given values are mostly rough estimates, some are interdependent and were generated iteratively.

	Mass 2 m span version [g]	Mass 3.5 m span version [g]
Structure		
Fuselage	3000	4000
Wings	3000	4000
Stabilizer	500	1000
Propulsion		
Engine	1000	1500
Batteries / fuel	1000	1500
Payload		
HV generator	800	800
HV batteries	200	200
Flight control system	1000	1000
Flight mass	10500	14000

therefore assessed iteratively. The mass of the payload was estimated on the basis of existing systems with an addition to render further extensions possible.

The flight speed can be calculated as

$$V = \sqrt{\frac{2\,L}{\rho\,S\,C_L}} \tag{3.3}$$

when the lift L, the wing area S and the lift coefficient of the wing C_L are known. For horizontal flight the lift can be assumed as equal to the weight G of the aircraft:

$$L = G = m_\mathrm{g}\,g. \tag{3.4}$$

The velocity range is defined by the maximum lift coefficient on the lower limit and the maximum propulsion power or structural and aeroelastic confinements on the upper.

The maximum lift coefficient $C_{L,\max}$ of a wing is smaller than the maximum lift coefficient $c_{l,\max}$ of its airfoil. At the wingtips no lift is produced due to the flow around the tip, towards the middle the lift increases. To

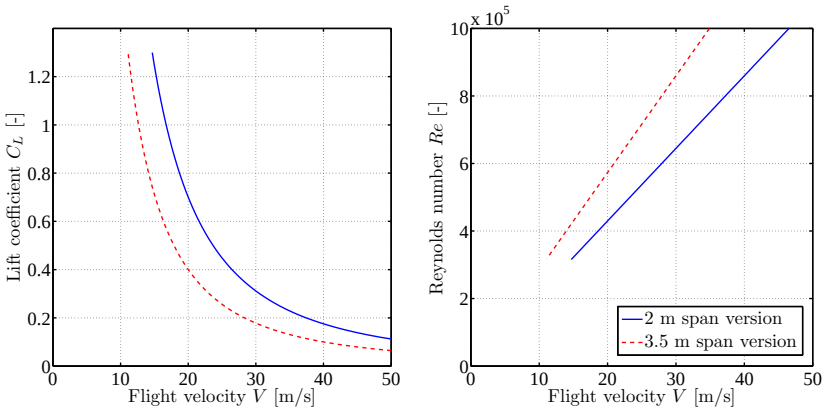

Figure 3.4: Lift coefficient and Reynolds number against flight velocity for 2 m and 3.5 m span version. In both cases a rectangular wing planform and a maximum lift coefficient $C_{L,\max} = 1.3$ is assumed.

ensure control of the plane at low speeds approaching stall conditions the flow separation has to occur first inboard and last at the ailerons. An empirical maximum lift coefficient for the wing of $C_{L,\max} = 1.3$ was assumed here. Since the flight speed

$$V \sim \frac{1}{\sqrt{C_L}}, \tag{3.5}$$

a change in maximum lift coefficient causes only a slight change of the stall speed, the resulting error is acceptably small.

The resulting speeds and Reynolds numbers are shown for both conceived versions in Figure 3.4. It can be seen that although the stall speed for the 2 m version is higher due to the higher wing loading, the resulting Reynolds numbers are approximately equal.

3.2.5 Airfoil

As already discussed in Section 2.2 airfoils specifically designed for the occurring low Reynolds number should be used. Since in the 3.5 m span concept the high voltage generators are to be placed in the wing a thick

profile is required. For the smaller version this is also favorable for structural reasons. Due to the modular concept the full thickness can not be utilized for the spar. The targeted flight speeds are as low as possible for better control authority of the actuator. Therefore the airfoil should be optimized for a relatively high lift coefficient, realized by a high camber. On the other hand thick airfoils at low Reynolds numbers tend to have lower maximum lift coefficients.

In Figure 3.5 an overview of different low Reynolds number airfoils with high thickness and relatively high maximum lift coefficients is given. Their lift-to-drag ratio against lift coefficient from XFOIL computations is shown in Figure 3.6. Although the Selig/Donovan SD 7062 and the Wortmann FX 63-137 offer a good performance the space inside the wing is comparably small. The Quabeck HQ/W-2,5/15 and the Selig/Giguere SG 6040 wind turbine airfoil have a very similar shape and performance. The HQ/W airfoil was chosen because of the slightly more docile stall behavior and the availability of a whole series of airfoils with finely graduated thicknesses and camber. On the right side of Figure 3.6 its performance is shown for different thicknesses and cambers. It can be seen that an increase in thickness or a decrease of camber causes a smaller maximum lift coefficient. On the other hand a decrease of thickness, which in this case is unwanted, or an increase of camber leads to a higher maximum lift coefficient and a better performance. The HQ/W-2,5/15 airfoil was chosen as best compromise for the wing of the UAV.

3.2.6 Plasma Actuator Momentum

Neither the maximum momentum of a DBD plasma actuator nor the thickness of its wall-jet can be altered arbitrarily, but are determined by its geometric and electrical parameters. Nonetheless, to estimate the potential of a flow control configuration, comparative values are needed to describe the correlation between flow and actuator.

To describe the boundary layer the local Reynolds number at a position x from the leading edge in streamwise direction is given as

$$Re_x = \frac{\rho V x}{\eta}. \tag{3.6}$$

The boundary layer thickness at this position is in the order of

$$\frac{\delta(x)}{x} = O\left(\frac{1}{\sqrt{Re_x}}\right) \tag{3.7}$$

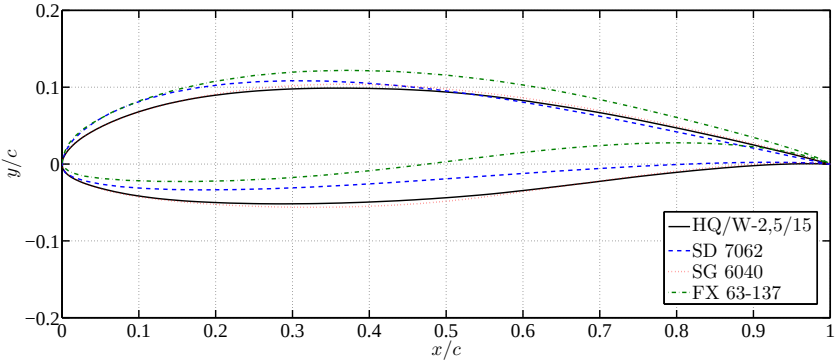

Figure 3.5: Airfoil geometries of the model aircraft airfoil Quabeck HQ/W-2,5/15, the Selig/Donovan SD 7062, the Selig/Giguere SG 6040 wind turbine airfoil and the low Reynolds number airfoil Wortmann FX 63-137.

for a laminar boundary layer on a flat plate. Thus the thickness scales with

$$\delta(x) \sim \sqrt{\frac{x}{V}}. \tag{3.8}$$

The same local Reynolds number and boundary layer thickness can be achieved for different combinations of V and x.

A commonly used measure for the impact of an actuator on the flow is the momentum coefficient

$$C_J = \frac{J}{c\,q} \tag{3.9}$$

with the actuator momentum to the flow

$$J = \int_0^\infty \rho\, u^2 \,\mathrm{d}y. \tag{3.10}$$

The momentum from a plasma actuator as used in this work is approximately around $1 \cdot 10^{-2}$ N/m for continuous operation [52]. This yields momentum coefficients in the order of $1 \cdot 10^{-3}$ in slow flight. This is more

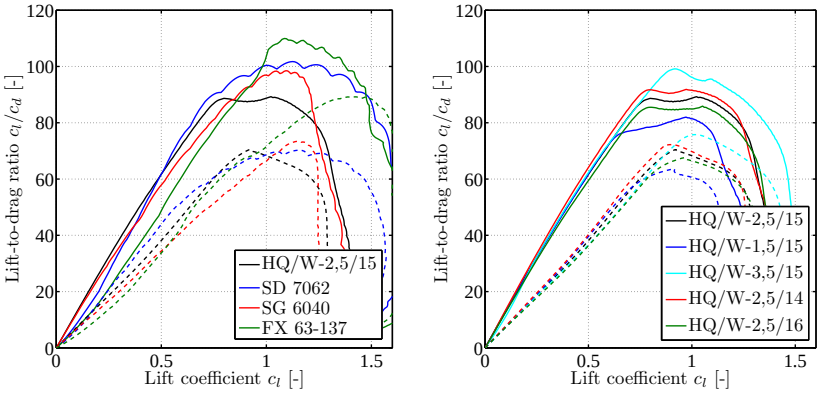

Figure 3.6: Lift-to-drag ratios against lift coefficient for different airfoils, shown are XFOIL computations for Reynolds numbers of 200.000 (dashed line) and 500.000 (solid line). In the left diagram the HQ/W-2,5/15, the Selig/Donovan SD 7062, the Selig/Giguere SG 6040 wind turbine airfoil and the FX 63-137 are compared. On the right variations of the HQ/W-2,5/15 with 1.5% and 3.5% camber and 14% and 16% thickness are compared.

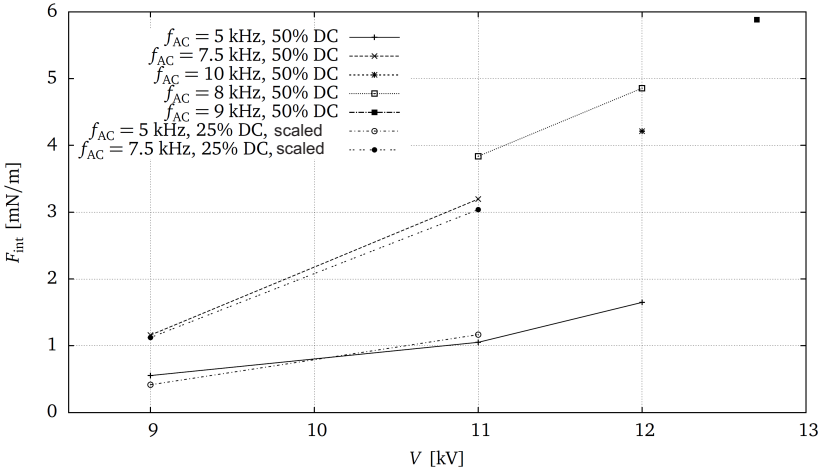

Figure 3.7: Thrust produced by a plasma actuator driven with the Minipuls 0 high voltage generator for different voltages, frequencies and duty cycles. The measurements were performed using a weight balance, as described in detail by Kriegseis [62].

than an order smaller than most values found in literature for circulation control airfoils [2, 31, 58, 81], although lower coefficients can be effective [93] as well as for drag reduction [45]. Therefore approaches using the instabilities of the flow are to be considered. Several promising flow control concepts from literature were chosen for the tests, as described in the following section.

3.3 Preliminary Tests of Control Authority

3.3.1 Experimental Set-Up

The preliminary tests were conducted in the Niedergeschwindigkeitswindkanal NWk 1 at the TU Darmstadt. This closed return wind tunnel has a test section of 2.4 m $\times$ 2.9 m, the maximum velocity is 68 m/s, in this study the range from 10 to 30 m/s was used. Further details regarding the flow quality and the wind tunnel scale are given in Section 6.2. No wind tunnel corrections were applied, since only the changes in the coefficients due to flow control are of interest.

To test different flow control concepts at various Reynolds numbers, wings of different chords were placed in the wind tunnel. The wings consists of three sections on a spar with the actuator covering the span of the middle one. They were vertically mounted on the wind tunnel balance to measure the lift and drag forces. A Minipuls 2 high voltage generator was used and installed below the wind tunnel. It was assured that neither interferences due to the high voltage nor forces due to the connections distort the measured results.

Modifications of the original airfoil, namely separation ramps, were constructed by applying styrofoam profiles on the middle wing section, covered with plastic sheet. This enables a fast change of configurations, but the achievable surface quality is relatively poor. To achieve a 2-dimensional flow boundary layer fences were used.

3.3.2 Discussion of Results

3.3.2.1 Unchanged Low Reynolds Number Airfoil

Three chord lengths 200, 400 and 500 mm at velocities of 10 and 30 m/s were tested. In the unactuated case the separation of the airfoil begins at the trailing edge and moves forward with increasing angle of attack, the lift curve slope has a relatively flat peak. Different approaches were tried to

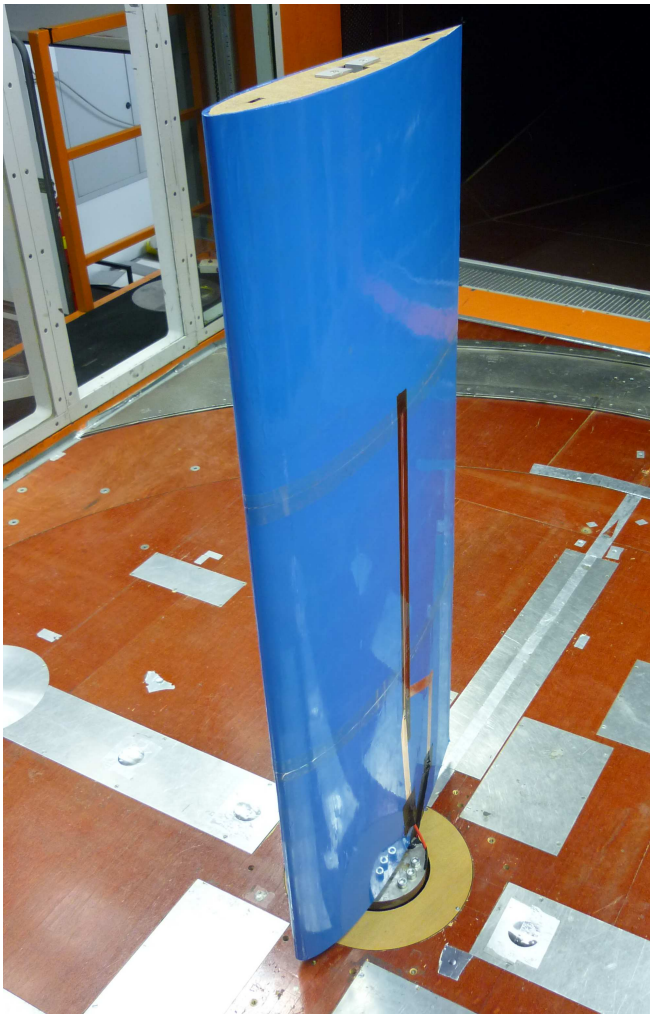

Figure 3.8: Wing in the NWk 1 wind tunnel for preliminary flow control tests with a SDBD plasma actuator mounted on the middle of the three spanwise sections.

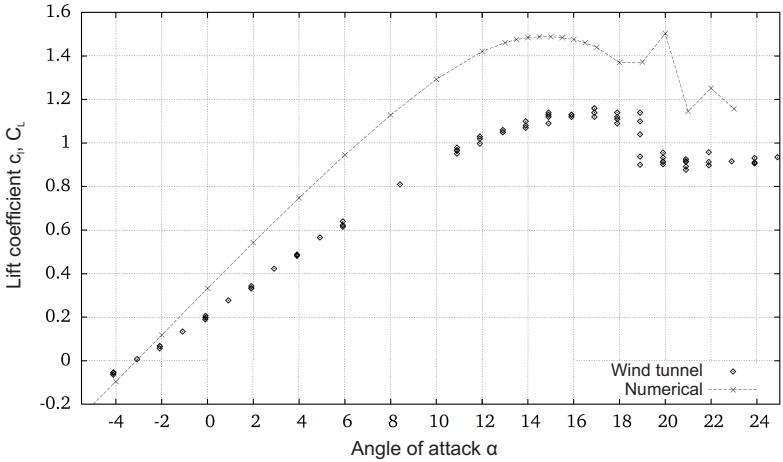

Figure 3.9: Lift over angle of attack of the unchanged HQ/W-2,5/15 low Reynolds number airfoil from numerical simulation and for the wing in the wind tunnel. The lower lift curve slope in the experiment is due to the finite span of the wing, the zero lift angle were adjusted to match.

delay separation. Single DBD plasma actuators were placed at the leading edge respectively in front of the separation and operated continuously or pulsed at different frequencies.

Previously numerical simulations were conducted to optimize the placement and pulse frequencies and reduce the number of experiments necessary. The simulation was conducted with OpenFOAM, using Reynolds Averaged Navier-Stokes (RANS) equations and a Spalart-Allmaras turbulence model. The simulation was found to be in good accordance with the experimental data.

The results of the SDBD actuators placed at the leading edge showed no significant effect of the actuator.

The placement of the actuator in front of the separation at 40 respectively 50% x/c results in an unchanged or slightly higher maximum lift coefficient at a higher angle of attack, depending on the configuration. The effect is limited to a very small range in angle of attack, since the separation line moves as shown in Figure 3.10.

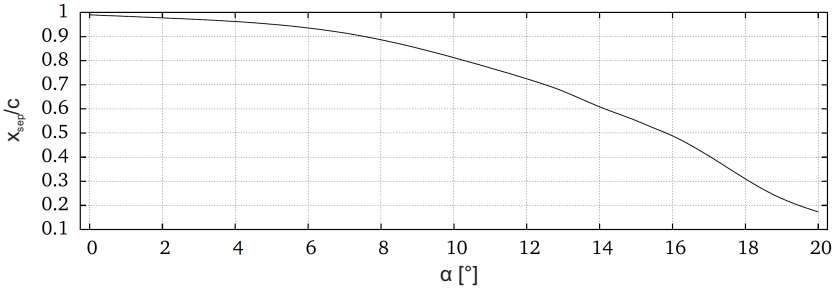

Figure 3.10: Position of separation against the airfoils angle of attack for the HQ/W-2,5/15 airfoil from numerical simulation.

Gurney flaps have a relatively large effect by changing the local flow field at the trailing edge. In order to mimic this effect a SDBD plasma actuator was placed at the trailing edge of the airfoil. Different configurations were applied with an actuator on the suction side forcing in flow direction, on the pressure side forcing upstream and around the trailing edge, but no significant effect was found for either of these configurations.

3.3.2.2 Separation Ramp

In order to control circulation the modification of a separation promises relatively large effects with small flow control effort. To create a fixed separation line a ramp on the airfoil is introduced. The position and the geometry of the ramp influence the strength of the separation. If placed in the front of the airfoil the flow is more likely to reattach, further downstream the boundary layer is weaker and more receptive to flow control effects.

Different configurations with a ramp at approximately 40 and 80% x/c, as well as at the trailing edge, were investigated for a chord of 400 mm. SDBD actuators and vortex generating VGDBDs actuator arrays were used.

The separation ramp at 040% x/c was found to be most susceptible to flow control. SDBD actuators in continuous and pulsed mode, as well as the VGDBD array increased the lift coefficient. While the SDBD actuator only produced a relatively small increase, the VGDBD changed the lift coefficient by up to 0.1 over a relatively wide range of angle of attacks.

The separation ramps at 80% x/c and at the trailing edge were found

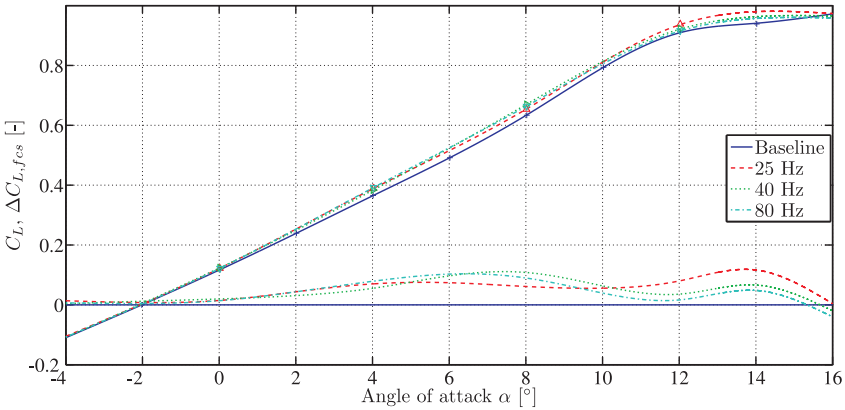

Figure 3.11: Wing lift coefficient and change in lift coefficient of flow control section for VGDBD array in front of the 40% x/c separation ramp. Shown are the changes in lift coefficient based on the actuated segment $C_{L,\mathrm{fcs}}$ for different burst frequencies. The actuator was operated at 40 W input power, the flow velocity was set to 10 m/s.

to produce no significant effect with any actuator. It is assumed that the deflection of the flow due to the actuation was not sufficient to achieve a reattachment, respectively prevent a separation.

3.3.3 Conclusion

In summary the preliminary flow control experiments showed that a significant effect is hard to obtain using DBD plasma actuators. Nonetheless, small effects were reached for an adequate range of angles of attack, although with an artificial flow configuration specifically designed for maximum effect. Since improvements of the actuators and an augmentation of their impact on the flow were key objectives of the PLASMAERO project, they were expected to be available after completion of the measurement platform. Nonetheless, to achieve the maximum effect the design of the smaller of the both conceived version of the UAV was pursued.

4 Design of the UAV

4.1 Physical Design and Dimensions

The general layout chosen after the pre-design considerations and tests described in Chapter 3 is a kite configuration featuring a rectangular shoulder wing with a chord c of 300 mm and a span b of 2380 mm. This chord combined with an anticipated stall speed V_S of 12 to 15 m/s, depending on the feasible weight, results in a minimum Reynolds number between $260,000$ and $320,000$. A structural mass of approximately 6 kg and a gross flight mass m_g of 10 kg are scheduled, as listed in Table 3.1.

The kite configuration was chosen because of the undisturbed airflow in front of the flow control sections of the wing and the simpler layout, especially for different airfoils on the wing. In a canard configuration wing and canard would have to be adjusted to each other to allow for acceptable stall behavior and longitudinal stability. Due to the relatively high wing at the top of the fuselage the plane is stable along the roll axis without adding any dihedral, simplifying modular interchangeability.

The propulsion system consists of two propellers in a pusher configuration mounted inboards on the wing. This allows the mounting of sensors, e.g. pitot-static tube, in front of the fuselage, and a relatively undisturbed airflow at the flow control sections on the wing.

Overall, this configuration facilitates the best possible conditions for flow control experiments on the wing as well as the easy measurement of the incoming airflow.

4.1.1 Wing

4.1.1.1 Overview

The wing has a rectangular planform, no dihedral and no aerodynamic or geometric twist. This allows for easy interchangeability of different flow control sections for the experiments. The wing sections are installed on a continuous spar with a constant profile along its length. Overall the wing has a span s of 2384 mm with a constant chord c of 300 mm.

Figure 4.1: Picture of the PLASMAERO UAV ready for flight.

Table 4.1: Specifications of the Plasmero UAV.

Dimensions			
Wingspan	b	2380	mm
Length		2075	mm
Height		615	mm
Wing area	S	0.714	m^2
Center of gravity	x_{cg}	30% x/c	
Mass			
Flight mass	m_g	10500	g
Structure		6000	g
Propulsion		2000	g
Flight control system		1000	g
Plasma actuator system		1000	g
Aerodynamic			
Stall speed	V_S	≈ 13	m/s
Reynolds number range	Re	$2.8–6 \cdot 10^5$	

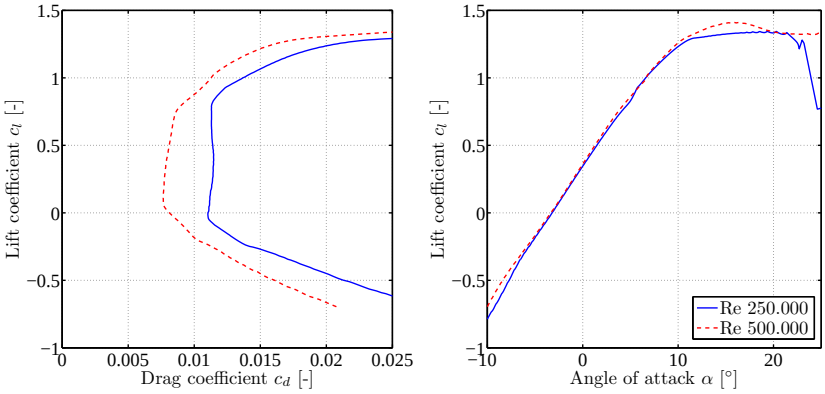

Figure 4.2: Lift over drag and angle of attack for the HQ/W-2,5/15 airfoil at Reynolds numbers of 250.000 and 500.000, calculated with XFLR5.

The default airfoil used is the Quabeck HQ/W 2,5/15 model aircraft airfoil with a thickness of $t/c = 15\%$ and a maximum camber $m/c = 2.5\%$. It is specifically designed for low Reynolds numbers and therefore has a good performance over a wide range of angles of attack, while exhibiting a docile behavior during stall. A polar curve for two typical Reynolds numbers is shown in Figure 4.2. Further characteristics in comparison with other airfoils are already discussed in Section 3.2.5. For the experiments other airfoils can be used on the actuator sections, with limitations regarding thickness and aerodynamic behavior.

4.1.1.2 Load assumptions

To dimension the spar for the wing an analysis of the loads was carried out. First an assumption regarding the maximum occurring loads was made, due to manoeuvring or gusts the load on the wing can be increased several fold compared to stationary horizontal flight. In this case a maximum load factor of $n_{\max} = 10$ was assumed, setting the design manoeuvring speed

$$V_A = \sqrt{n}\, V_S = 3.16\, V_S. \tag{4.1}$$

Above this speed the wing is able to produce a higher lift than the structure is designed for. Thus it should only be exceeded in quiescent air and

Table 4.2: Geometric parameters of the wing.

Wing			
Airfoil		HQ/W 2,5/15	
Chord	c	300	mm
Thickness	t/c	15	%
Camber	m/c	2.5	%
Incidence	ε	5	°
Area	S	0.714	m^2
Wingspan	b	2380	mm
Half-span	s	1190	mm
Aspect ratio	Λ_W	7.93	
Dihedral		0	°
Sweep		0	°
Lever arm z	l_z	≈ 100	mm
Lift curve slope	$\frac{dC_{L,W}}{d\alpha}$	4.9	
Wing reference volume	V_W	1.05	m^3
Aileron			
Span	b_{ail}	400	mm
Chord	c_{ail}	75	mm
Effect	$\frac{\partial\alpha}{\partial\xi}$	≈ 0.5	
Maximum deflection	ξ_{max}	-15–$+10$	°

with only small control surface deflections applied. Usually, as can be seen in Figure 4.3, the envelope is limited by a slightly decreasing load factor for higher velocities and the design maximum speed V_D.

In Figure 4.4 the load factors due to vertical gusts of the velocity U_G are shown, they can be estimated by

$$n = 1 \pm \left(\frac{\frac{k_\mathrm{G}}{2}\,\rho\, U_\mathrm{G}\, V\, \frac{\mathrm{d}C_L}{\mathrm{d}\alpha}}{\frac{m\,g}{S}} \right) \tag{4.2}$$

with the gust alleviation factor [57]

$$k_\mathrm{G} = \frac{0.88}{1 + 2.65\,\frac{\rho\, c\, S}{m}\,\frac{\mathrm{d}C_L}{\mathrm{d}\alpha}} = 0.66. \tag{4.3}$$

Since the UAV operates in low altitudes, the gust velocities to be expected are relatively small with an assumed vertical speed of $U_\mathrm{G} = 20\,\mathrm{ft/s} \equiv 7.62\,\mathrm{m/s}$. Nonetheless, due to the low wing loading $\frac{m\,g}{S}$ the resulting load factors of $n = 1 \pm 5.15$ are relatively high. This gives rise to the rather high maximum load factor assumed for the design of the aircraft.

To calculate the resulting bending moment from this maximum lift on the spar an assumption of the lift distribution has to be made. The easiest is a constant distribution along the wing span, as the planform of the wing is rectangular. Since the outboard sections do produce a smaller part of the lift due to the wingtip vortices this assumption would lead to a significantly higher estimated bending moment. To get a better assumption a simple model of the airplane was evaluated using the software XFLR5 [24, 25]. The calculated lift distribution in Figure 4.5 shows the anticipated smaller lift outboards as well as a drop in the vicinity of the fuselage.

The correspondent lift forces can be calculated from the equation

$$L = m_\mathrm{g}\, n\, g \tag{4.4}$$

$$= \frac{\rho}{2}\, V_\mathrm{A}^2 \int_{-\frac{s}{2}}^{+\frac{s}{2}} c_l(y)\, c\, \mathrm{d}y \tag{4.5}$$

solved for the design manoeuvering speed V_A, which is then inserted in the equation for the lift per unit span

$$L'(y) = \frac{\rho}{2}\, V_\mathrm{A}^2\, c_l(y)\, c. \tag{4.6}$$

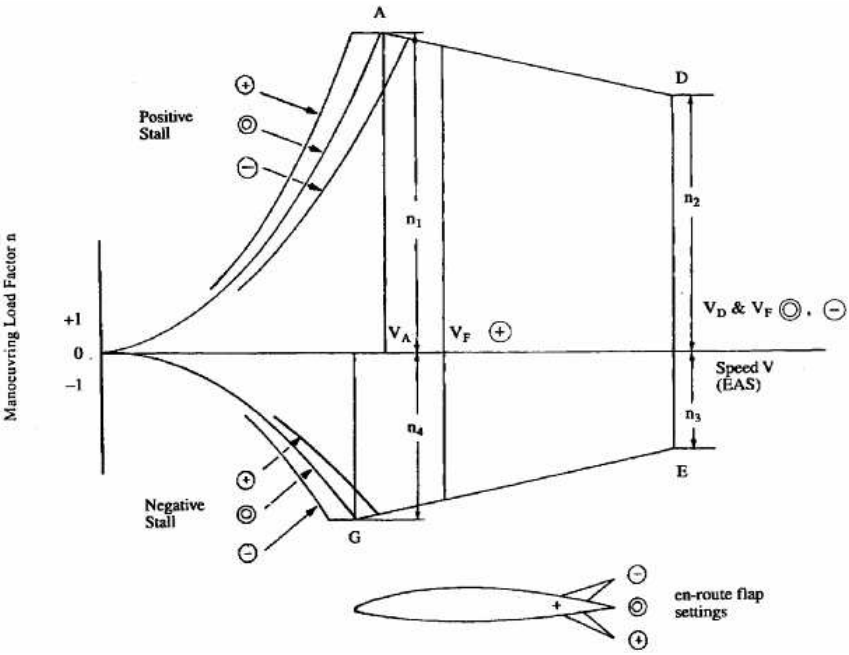

Figure 4.3: Generic aircraft manoeuvring envelope (from [57]).

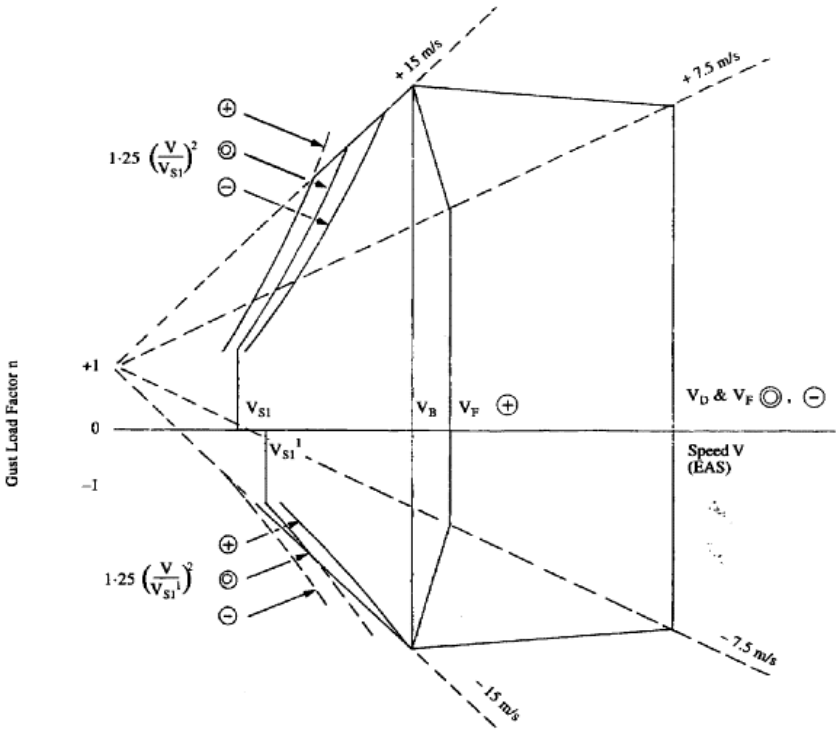

Figure 4.4: Generic gust envelope (from [57]).

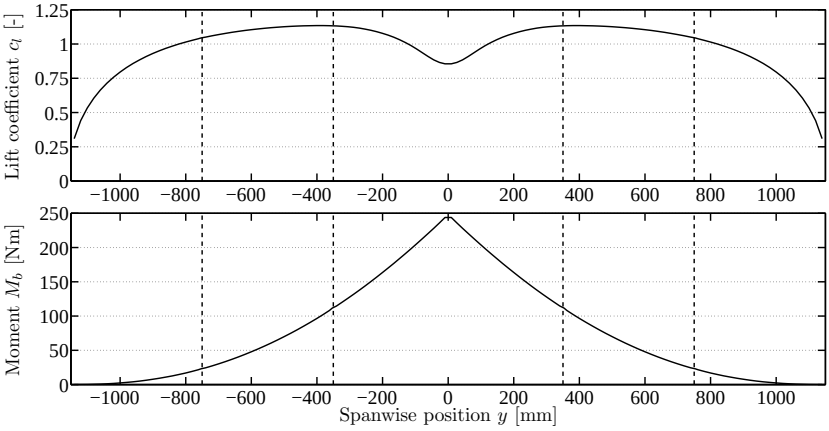

Figure 4.5: Lift distribution and bending moment along the wing span for maximum load.

The shear force Q and the bending moment M_b on the spar resulting from the lift distribution can be calculated by integration, the moment is shown in Figure 4.5. The self-weight of the wing was neglected, leading to a rather conservative assumption.

4.1.1.3 Spar

The spar consists of a light weight balsa wood bar with CRP caps and a GRP shear web. The height of the spar was set to 35 mm, allowing clearance towards the covering of the wing, which is around 2.5 mm thick. With an assumed maximum bending moment of 244 Nm mid-span the spar was dimensioned.

With a fibre parallel strength $R_\parallel$ of the CRP of 600 N/mm^2 the required cross section of carbon fibres in the spar cap can be calculated to 11.62 mm^2. The necessary amount of roving is assessed by dividing by the cross section of one roving while taking into account the resin, a fibre volume fraction of $\varphi \approx 0.5$–0.6 is assumed. The cross section of one roving can be calculated by its mass per length unit, 800 tex, and the density of the fibre, $1,8$ g/cm^3. This yields an amount of 15 roving in the highest loaded point in the middle of the wing. A safety factor of 1.5 was applied in this case, with 23 roving in the middle. Outboards this amount is gradually reduced according to the local bending moment.

The roving are applied on an rectangular balsa wood bar, slightly smaller then the final dimension of the spar. A layer of GRP is applied around the spar, acting as shear web. The thickness of the shear web can be calculated with the maximum shear force $Q_{\max}$ and the shear resistance of the GRP $R_{\perp\parallel}$. With the maximum shear force in the middle of the wing $Q_{\max} = 500$ N and assuming a shear resistance $R_{\perp\parallel} = 50$ N/mm^2, a thickness of 0.142 mm is yielded. Two layers of GRP with a 105 g/m^2 heavy glass fabric were applied, resulting in a thickness of 0.22 mm. The spar was put in a mould during the curing process of the resin to achieve the exact final dimensions.

4.1.1.4 Wing sections

The middle section has a span s_{mid} of 700 mm and is mounted on top of the fuselage. The two pusher propellers including electric motors, controllers and batteries are placed in a housing 250 mm outboard in the back of the wing, the propellers are as far inboard as possible while having a sufficient clearance to each other and the fuselage. The propulsion system is described in detail in Section 4.1.3.

The adjoining sections are those for the flow control experiments with a span s_{fcs} of 400 mm each.

The outer sections also have a span s_{out} of 400 mm and comprise the ailerons over their full span. The wingtip consists of a laser-sintered plastic part.

The individual wing sections are slid onto the spar, allowing for an easy exchange of experiments. To achieve this, a GRP sleeve is built into each wing section as guide for the spar. The sleeve is attached to the ribs and the covering of the sections on both suction- and pressure-side. In between the sections small wing fences are installed to achieve an preferably two-dimensional flow over the flow control section. The wing tips are covered with a laser-sintered plastic part with a small wing tip fence.

For the wing covering 400 mm, respectively 700 mm for the middle section, span moulds, consisting of pressure and suction side part are used. A white UP pre-gel is applied as coating before applying the laminate. It consists of GRP with 50 g/m^2 fabric on the surface, followed by 100 g/m^2 glass, 2 mm foam sandwich material, and 100 g/m^2 glass on the inside. Ribs are placed at the ends of each section to transmit the moments, and in their middle to support the covering. They are made of lasercut 2.5 mm air-plywood, glued in one half of the mould, together with the sleeves for the spar. Additionally that half has an overlap at the nose radius for joining

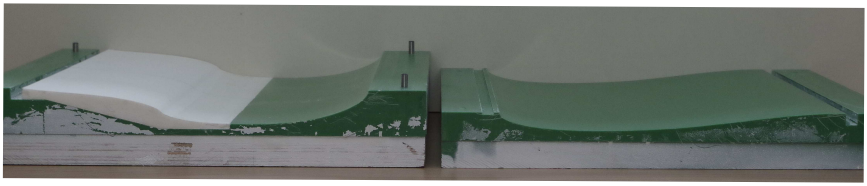

Figure 4.6: Mould for the 400 mm span flow control and outer wing sections with a modified HQ/W-2,5/15 airfoil. Modifications to the airfoil are realized by plastic inserts on the suction side.

the two sides together.

The torsional moment is transmitted at the joints via torsion bolts in the front and back of the wing ribs. The moment at the highest loaded joint between middle and flow control section can be calculated by adding up the maximum pitching moments of the outer and flow control sections:

$$M_{\max} = \frac{\rho}{2} V^2 \sum c_{m,i}\, c_i^2\, s_i \tag{4.7}$$

The maximum pitching coefficient c_m for unchanged airfoil and with deflected flap can be derived from Figure 4.7. The maneuvering velocity is derived from according to Equation 4.1, yielding a maximum moment of 17.34 Nm around the 25% x/c axis. The moment around the spar can be calculated by including the lift coefficient, resulting in a moment of 14.86 Nm. The torsion bolts in the wing ribs are 6 mm in diameter and placed 89 mm respectively 106 mm from the spar.

4.1.1.5 Ailerons

The ailerons enable the aircraft to roll by changing the local lift coefficient. A moderate roll rate is sufficient for the planned manoeuvres, so a spanwise length of 400 mm, over the whole outer section is sufficient. The chordwise length of the aileron is restricted by the airfoil. For the chosen airfoil a chordwise length of around 20% is recommended, a length of 25% was chosen after examination of XFLR5 [24] computations. The rolling moment for an elliptic wing is given by

$$C_{l\xi} = -\frac{4}{3\,\pi} \frac{\pi\,\Lambda}{\sqrt{\left(\frac{\pi\,\Lambda}{C_{L\alpha}}\right)^2 + 4} + 2} \frac{\partial \alpha}{\partial \xi} \left(1 - \eta_{\text{ail}}^2\right)^{\frac{3}{2}} \tag{4.8}$$

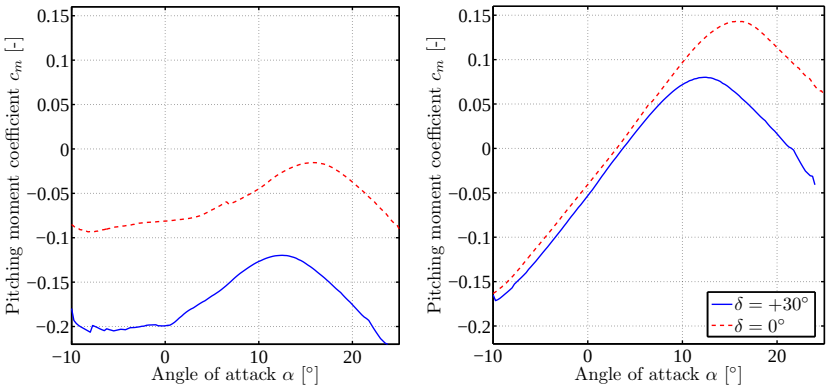

Figure 4.7: Pitching moment coefficient around the 25% x/c axis (left) and the spar (right) of HQ/W-2,5/15 airfoil at a Reynolds number of 500.000 for an unchanged airfoil and with a $\xi = 30°$ deflected flap hinged at 75% chord.

with $(1 - \eta_{\text{ail}})$ being the dimensionless spanwise length of the aileron and $\frac{\partial \alpha}{\partial \xi}$ the aileron effect, again derived from a XFoil computation.

The ailerons are constructed by adding a peel ply to the suction side covering which acts as a hinge after removing the rest of the laminate. On the pressure side a gap is cut into the covering to allow the aileron to move freely to a deflection of approximately 10° downwards and 15° upwards. The gap is closed with convex seal tape. The linkage is installed on the outer-most position and connects to a servo motor, further described in section 4.3.2.3.

4.1.2 Tail Section

The function of the tail section is to stabilize and control the plane around the yaw and pitch axis. It consists of the horizontal stabilizer in an all-moving tail configuration, the vertical stabilizer and the rudder.

The horizontal all-moving tail configuration was chosen because of its simple design and the capability to adjust for different pitching moments of the exchangeable wing sections. The axis of rotation of the stabilizer is at the 25% x/c position, in combination with a symmetric airfoil very small torque occurs in the operating range. Each half of the stabilizer is

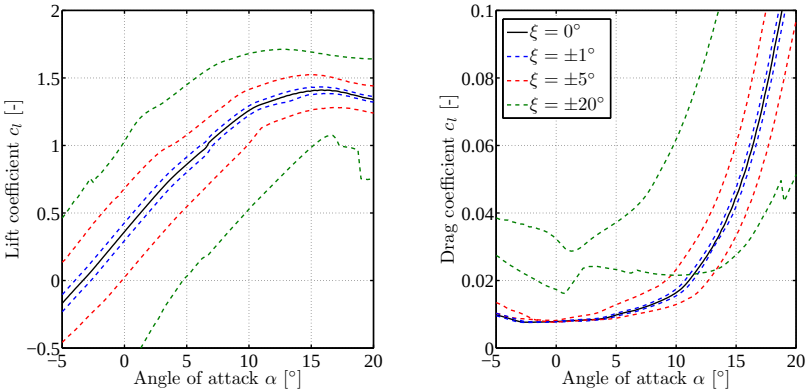

Figure 4.8: Lift and drag coefficients for different aileron deflections ξ from XFoil.

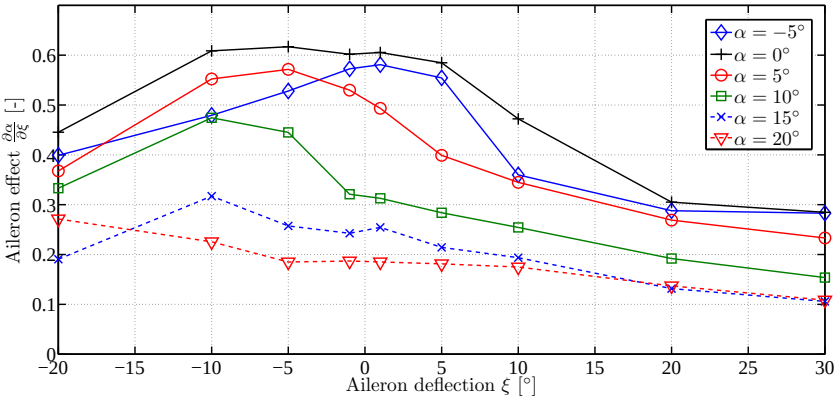

Figure 4.9: Effect of aileron deflection for different angles of attack from XFoil computations.

independently revolvable and linked to a servo motor to assure redundance. The motors are installed in the back of the tail to achieve ample spatial separation from the high voltage generators and plasma actuators. The stabilizer has a half-span of 325 mm and a tapered planform with a chord length of 200 mm at the root and 150 mm at the tip. This results in a stabilizer area of 0.113 m^2 and an effective horizontal tail volume [102] of

$$V_{\mathrm{H}} = C_{L_{\alpha_{\mathrm{H}}}} l_{\mathrm{H}} S_{\mathrm{H}} = 0.4 \text{ m}^3, \tag{4.9}$$

with the lift curve slope estimated as

$$C_{L_{\alpha_{\mathrm{H}}}} = \frac{\mathrm{d}C_{L_{\mathrm{H}}}}{\mathrm{d}\alpha_{\mathrm{H}}} = \frac{2\,\pi\,\Lambda_{\mathrm{H}}}{2 + \sqrt{\Lambda_{\mathrm{H}}^2 + 4}}. \tag{4.10}$$

The tail moment arm

$$\frac{l_{\mathrm{H}}}{c_{\mu}} = 0.3167 \tag{4.11}$$

has to be relatively short, due to the high weight of the servo motors in the tail. Moreover the non-dimensional volume

$$\frac{V_{\mathrm{H}}}{V_{\mathrm{W}}} = 0.38 \tag{4.12}$$

is comparably small [102], but adequate due to the high effectiveness of the all-flying tail.

The vertical stabilizer has the same dimension as one half of the horizontal stabilizer, but is fixed and has a 25% chord length rudder. It is positioned 860 mm forward of the horizontal stabilizer for sufficient clearance at full deflections of both control surfaces. Again, the vertical stabilizer volume is calculated as

$$V_{\mathrm{V0}} = \frac{\mathrm{d}C_{L_{\mathrm{V0}}}}{\mathrm{d}\beta}\, l_{\mathrm{V0}}\, S_{\mathrm{V0}} = 0.12 mem^3, \tag{4.13}$$

respectively

$$\frac{V_{\mathrm{V0}}}{S\,b} = 0.071. \tag{4.14}$$

Although this is a relatively large value, the stability around the yaw axis was found to be marginal during first test flights due to the large fuselage. Therefore a fin in front of the stabilizer was installed, increasing the stabilizer area and volume slightly.

Table 4.3: Geometric parameters of the horizontal stabilizer.

Horizontal stabilizer			
Airfoil		HQ/W 0/10	
Mean aerodynamic chord	$c_{\mu,\mathrm{H}}$	177	mm
Thickness	$(t/c)_{\mathrm{H}}$	10	%
Camber	$(m/c)_{\mathrm{H}}$	0	%
Area	S_{H}	0.113	m^2
Wingspan	b_{H}	650	mm
Half-span	s_{H}	325	mm
Aspect ratio	Λ_{H}	3.74	
Dihedral		0	°
Sweep		0	°
Elevator effect	$\frac{\partial \alpha_{\mathrm{ele}}}{\partial \eta}$	1	
Maximum deflection	$\eta_{\max}$	± 15	°
Dynamic pressure	$\frac{q_{\mathrm{H}}}{q}$	1.3	
Lever arm	l_{H}	950	mm
Lift curve slope	$\frac{\mathrm{d}C_{L,\mathrm{H}}}{\mathrm{d}\alpha_{\mathrm{H}}}$	3.77	
Stabilizer volume	V_{H}	0.4	m^3

Table 4.4: Geometric parameters of the vertical stabilizer.

Vertical stabilizer			
Airfoil		HQ/W 0/10 plus fin	
Mean aerodynamic chord	$c_{\mu,\mathrm{V}}$	177	mm
Thickness	$(t/c)_{\mathrm{V}}$	10	%
Camber	$(m/c)_{\mathrm{V}}$	0	%
Area	S_{V0}	0.0565	m^2
Wingspan	b_{V}	325	mm
Aspect ratio	Λ_{V0}	1.87	
Dihedral		0	°
Sweep		0	°
Dynamic pressure	$\frac{q_{\mathrm{V}}}{q}$	1.3	
Lever arm x	l_{V}	860	mm
Lever arm z	$l_{z,\mathrm{V}}$	≈ 100	mm
Lift curve slope	$\frac{\mathrm{d}C_{L,\mathrm{V0}}}{\mathrm{d}\beta}$	2.48	
Stabilizer volume	V_{V0}	0.12	m^3
Area with fin	S_{V}	0.081	m^2
Aspect ratio with fin	Λ_{V}	1.3	
Lever arm x with fin	$l_{x,\mathrm{V}}$	800	mm
Lift curve slope with fin	$\frac{\mathrm{d}C_{L,\mathrm{V}}}{\mathrm{d}\beta}$	1.86	
Stabilizer volume with fin	V_{V}	0.121	m^3
Rudder			
Chord	$c_{\mu,\mathrm{rud}}$	44	mm
Effect	$\frac{\partial\beta_{\mathrm{rud}}}{\partial\zeta}$	≈ 0.5	
Maximum deflection	$\zeta_{\max}$	± 15	°

4.1.3 Propulsion System

In general there are two different conceivable types of propulsion for this type and size of UAV, a jet engine or a propeller drive. Although jet engines of the required size are commercially available, a propeller drive is more economical in terms of power efficiency, as well as maintenance and usability.

Two propellers were chosen to be installed on the wing in a pusher configuration, to facilitate the use of the plane for flight experiments. For this different sensors are installed, and at least barometric and dynamic pressure sensors need to be positioned in a preferably undisturbed flow. This can either be done on the wing, if the propeller is in the front of the fuselage, or in front of the fuselage for wing-mounted propellers. Sensors in the wing are prone to disturbances by nearby mounted plasma actuators, pressure probes on the wing with flexible tubes to sensors in the fuselage have the disadvantage of relatively long time lag, increasing the response time [99]. The added connection is also a further complexity and source of error when exchanging wing sections.

Also the experiments are conducted on the wings, the flow there should also be as undisturbed as possible. Therefore a tractor configuration with the flow control sections directly behind the propellers is to be avoided. Nevertheless, also in the pusher configuration an influence on the upstream flow control section is present, due to the pressure gradient at the propeller. Therefore they are mounted as far inboard as possible without colliding with the tail boom or each other, so that only a small portion of the flow control section is directly upstream.

A further decision is the choice of the engine for propulsion, internal combustion engine or electric motor. There are several disadvantages of internal combustion engines compared to electric motors:

- The fuel is highly flammable, however the aircraft will have high voltage systems on board which can emit sparks, posing a serious hazard.
- The vibrations caused by the engine are considerably higher than for an electrical motor. This could cause problems with the inertial measurement system used and falsify measurements.
- An internal combustion engine is comparatively complicated and has to be frequently adjusted and serviced.
- Due to the higher noise emission stricter regulations may apply.

- The weight of the plane is not constant, it changes due to the used fuel. This can complicate evaluation and comparability of measurements.

An important factor when considering the choice of the engine is the weight of the system. Generally an internal combustion engine is slightly heavier than an electrical motor of the same power as can be seen in Figure 4.10. The mass of the system, including fuel, respectively batteries, can be expressed as

$$m_{\mathrm{ICE,res}} = m_{\mathrm{ICE}} + \frac{\rho_{\mathrm{Fuel}}}{u_{\mathrm{Fuel}}\,\eta_{\mathrm{ICE}}} \int_0^{t_{\max}} P_{\mathrm{P}}(t)\,\mathrm{d}t, \tag{4.15}$$

respectively

$$m_{\mathrm{EM,res}} = m_{\mathrm{EM}} + \frac{m_{\mathrm{Bat}}}{E_{\mathrm{Bat}}\,\eta_{\mathrm{EM}}} t_{\max} \int_0^{t_{\max}} P_{\mathrm{P}}(t)\,\mathrm{d}t, \tag{4.16}$$

with u being the energy density and $t_{\max}$ the maximum flight time. The efficiency η of the engines were assumed to be 0.2 for a two-stroke, 0.3 for a four-stroke internal combustion engine [82] and 0.8 for a brushless direct current (BLDC) motor, being of course only coarse approximations. Fuel has a far higher specific energy compared to state-of-the-art batteries, thus an internal combustion system has a considerably weight advantage at longer flight times. Since in this application they are relatively short, the advantages of the electric motor prevail and a BLDC motor was chosen.

The power and thrust needed can be estimated for the planned flight mass of the UAV m_{g}. Considering the obstacles, such as trees and power lines, around a typical model aircraft airfield, a high angle of climb γ is favorable. For an arbitrarily set angle $\gamma = 30°$ a thrust of

$$T = 0.5 \left(\sin(\gamma)\; m_{\mathrm{g}}\, g + \frac{\rho}{2}\, S\, C_D\, V^2 \right) \tag{4.17}$$

can be appraised for each propeller. With a flight velocity of $V = 20$ m/s the resulting force amounts to $F_{\mathrm{T}} = 30$ N. The thrust power needed is given by

$$P_{\mathrm{T}} = T\, V = 600 \text{ W}. \tag{4.18}$$

The propeller thrust can be written as

$$T = \dot{m}_{\mathrm{P}}\; (V_{\mathrm{P}} - V)\,, \tag{4.19}$$

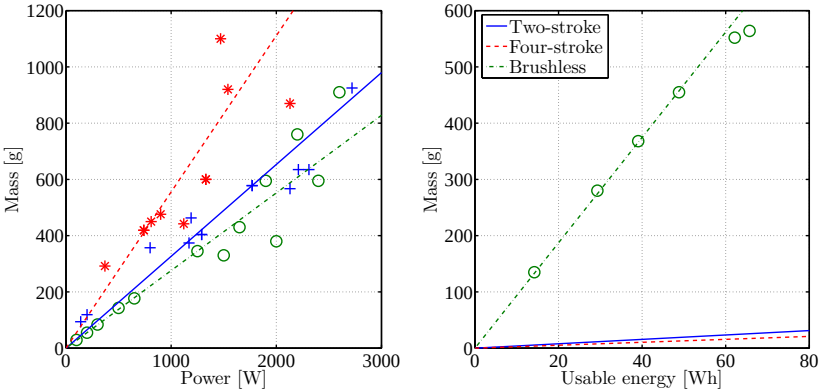

(a) Mass against power of typical model aircraft engines.

(b) Mass of fuel, respectively batteries, against usable energy ηE.

Figure 4.10: Mass against power of typical model aircraft engines from different manufacturers and mass against usable energy ηE for the different engine types.

the power applied to the propeller which is needed for this thrust is given by

$$P_\mathrm{P} = (1 + \zeta_\mathrm{P}) \left(T V + \frac{\dot{m}_\mathrm{P}}{2} \left(V_\mathrm{P} - V \right)^2 \right), \tag{4.20}$$

with ζ_P being the loss coefficient and V_P the velocity of the flow behind the propeller. The mass flux through a propeller with a diameter d_P is

$$\dot{m}_\mathrm{P} = \frac{\pi}{4} \rho \, d_\mathrm{P}^2 \, \frac{V_\mathrm{P} + V}{2}. \tag{4.21}$$

The efficiency of a propeller can be written as

$$\eta_\mathrm{P} = \frac{1}{1 + \zeta_\mathrm{P}} \, \frac{2 \, \nu_\mathrm{P}}{1 + \nu_\mathrm{P}} \tag{4.22}$$

with the velocity ratio

$$\nu_\mathrm{P} = \frac{V}{V_\mathrm{P}}. \tag{4.23}$$

For larger diameters the velocities approach each other and the efficiency is maximized. In this case two 16 inch propellers are used and the required velocity V_P calculated by applying Equation 4.21 to Equation 4.19:

$$V_\mathrm{P} = \sqrt{\frac{F_\mathrm{P}}{\frac{\pi}{4}\,\rho\,d_\mathrm{P}^2} + V^2} = 27.9 \text{ m/s} \tag{4.24}$$

The power to the propeller is then calculated with Equation 4.20 and an assumed loss coefficient $\zeta_\mathrm{P} = 0.7$ to 1222 W.

With a maximum rotation speed of model aircraft propellers of usually 8000 rpm a pitch of 8.23 inch is calculated and 8 inch pitch propellers selected. This setup is very well suited to the low speed flight regime of the experiments, but limits the maximum stationary horizontal flight speed to approximately 30 m/s. Other propellers with a smaller diameter and larger pitch can be installed, if this is deemed necessary for a specific task.

The propellers turn in opposite directions to compensate the torque. This is relatively easy to accomplish with BLDC motors by interchanging the connection cables or reprogramming the controller. To determine the rotational direction the following consideration was made: Due to the position of the propulsion above the center of gravity it creates a pitching moment. This can be dangerous during an aborted landing, due to the sudden change in thrust the plane pitches down. The slipstream of the propeller hits the horizontal stabilizer, the core of its slipstream is approximately at the tips of the stabilizer. A downstream component of the slipstream on the stabilizer results in a negative lift component on it and thereby in a reduced pitching moment on the aircraft.

4.1.4 Fuselage

The fuselage has a multitude of functions, the most fundamental being the ability to accommodate the required payloads. Since in this case the payloads were partially unknown during the development process a rather spacious fuselage was realized. The known payload components include a flight control and measurement system as described in Section 4.3.3, two small Minipuls devices and a power supply in form of batteries. The interior cross section of the payload section was chosen to be rectangular with 166 mm × 166 mm and a length of 540 mm in front of the wings. The sides of the section consist of a GRP-foam sandwich, the outside is covered by a curved layer of styrofoam and GRP which protects the payload in case of a crash. The flight control system is installed in the front. The two

Minipuls high voltage generators are installed on the side below the wings. They are covered by laser-sintered plastic parts with air in- and outlets to avoid overheating.

Another critical function of the fuselage is to connect all parts of the aircraft and transfer the resulting loads during flight, but also on the ground. To this avail a highly reinforced section was constructed which connects the wings, the tail boom and the main landing gear. Wings and landing gear are connected via screws and glued-in threads in the fuselage. The tail boom connects to a fitting tube glued into the fuselage and is held against axial and torsional movement by a bolt.

In the front a nose cone of laser-sintered plastic is installed which features air inlets and can hold a pitot-static probe with 3 mm diameter. Behind the wings another laser-sintered plastic part is mounted as covering on the tail boom.

The gear consists of a main gear with a 480 mm wheel gauge behind the center of gravity and a steerable nose gear in the front, with 150 mm, respectively 100 mm diameter wheels.

4.2 Flight Mechanical Properties

4.2.1 Coordinate Systems and Denotation

Several different coordinate systems are used to describe the flight mechanical properties of the aircraft. The geodetic system is used to describe the absolute position of the aircraft and gravity, for aerodynamic forces and moments the aerodynamic system is used. The primary coordinate system used in this case is the body fixed coordinate system, with the x-axis pointing in direction of the fuselage, the y-axis towards the right wing and the z-axis towards the bottom of the aircraft. Since the body fixed system commonly used in robotic applications is in front-left-up notation, it is also used in the software of the flight control system, and converted later. The variables can be transformed between the different coordinate system, in the following section the coordinate system used is the body system with the denotations as shown in Figure 4.11, if not explicitly mentioned.

4.2.2 Equations of Motion

The aerodynamic forces on the aircraft can be written in the aerodynamic coordinate system as

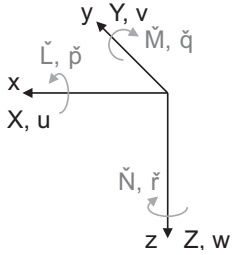

Figure 4.11: Axis, force, velocity, moment and rotational velocity denominations of the body coordinate system.

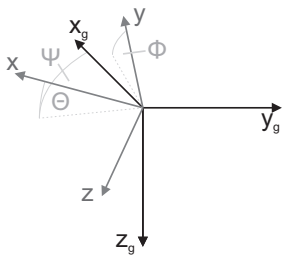

Figure 4.12: Transformation from geodetic to body coordinate system. The system is first rotated around the z-axis with the course angle Ψ, then around y with the pitch angle Θ, and finally around the x-axis with the roll angle Φ.

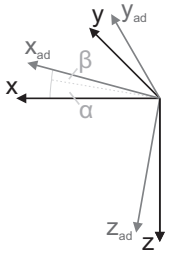

Figure 4.13: Transformation from body coordinate system to aerodynamic system. The system is first rotated around the y-axis with the angle of attack α, then around z_{ad} with the yaw angle β.

$$\vec{F}_{\mathrm{ad,a}} = q\,S \begin{bmatrix} C_{X,\mathrm{a}} \\ C_{Y,\mathrm{a}} \\ C_{Z,\mathrm{a}} \end{bmatrix} = q\,S \begin{bmatrix} -C_D \\ C_{Y,\mathrm{a}} \\ -C_L \end{bmatrix}_{\mathrm{ad}} \tag{4.25}$$

and the moments as

$$\vec{M}_{\mathrm{a}} = q\,S \begin{bmatrix} s\,C_{\check{L},\mathrm{a}} \\ c\,C_{\check{M},\mathrm{a}} \\ s\,C_{\check{N},\mathrm{a}} \end{bmatrix}. \tag{4.26}$$

The coefficients C_x are given as:

$$C_{X,\mathrm{a}} = -C_D = -C_{D,1} - k\,(C_L - C_{L,1})^2 \tag{4.27}$$

$$C_{Y,\mathrm{a}} = C_{Y_\beta}\,\beta + C_{Y_\xi}\,\xi + C_{Y_\zeta}\,\zeta + \frac{b}{2\,V}\left(C_{Y_{\check{p}}}\,\check{p} + C_{Y_{\check{r}}}\,\check{r}\right) \tag{4.28}$$

$$C_{Z,\mathrm{a}} = -C_L = -C_{L,2} - C_{L_\alpha}\,\alpha - C_{L_{\check{q}}}\,\frac{c}{V}\,\check{q} - C_{L_\eta}\,\eta \tag{4.29}$$

$$C_{\check{L},\mathrm{a}} = C_{\check{L}_\beta}\,\beta + C_{\check{L}_\xi}\,\xi + C_{\check{L}_\zeta}\,\zeta + \frac{b}{2V}\left(C_{\check{L}_{\check{p}}}\,\check{p} + C_{\check{L}_{\check{r}}}\,\check{r}\right) \tag{4.30}$$

$$C_{\check{M},\mathrm{a}} = C_{\check{M},2} + C_{\check{M}_\alpha}\,\alpha + C_{\check{M}_{\check{q}}}\,\check{q}\,\frac{c}{V} + C_{\check{M}_\eta}\,\eta \tag{4.31}$$

$$C_{\check{N},\mathrm{a}} = C_{\check{N}_\beta}\,\beta + C_{\check{N}_\xi}\,\xi + C_{\check{N}_\zeta}\,\zeta + \frac{b}{2V}\left(C_{\check{N}_{\check{p}}}\,\check{p} + C_{\check{N}_{\check{r}}}\,\check{r}\right) \tag{4.32}$$

In the same manner the propulsion force and moment is written as

$$\vec{T} = \begin{bmatrix} T \\ 0 \\ 0 \end{bmatrix} \tag{4.33}$$

and

$$\vec{M}_T = \begin{bmatrix} 0 \\ z_T\,T \\ 0 \end{bmatrix}. \tag{4.34}$$

The weight is given in the geodetic coordinate system by

$$\vec{F}_{\mathrm{gs,g}} = \begin{bmatrix} 0 \\ 0 \\ m_{\mathrm{g}}\, g \end{bmatrix}_{\mathrm{gs}}. \tag{4.35}$$

Converting all forces and moments into the body coordinate system and adding them yields the total forces $\vec{F}$ and moments $\vec{M}$. The equations of motion are expressed as

$$\vec{F} = \begin{bmatrix} X \\ Y \\ Z \end{bmatrix} = m \left(\dot{\vec{V}} + \vec{\Omega} \times \vec{V} \right) \tag{4.36}$$

$$\vec{M} = \begin{bmatrix} L \\ M \\ N \end{bmatrix} = \mathbf{J}\, \dot{\vec{\Omega}} + \vec{\Omega} \times \left(\mathbf{J}\, \vec{\Omega} \right) \tag{4.37}$$

with $\vec{V}$ being the velocity vector, $\vec{\Omega}$ the rotational velocities and $\mathbf{J}$ the inertia matrix. The used derivatives for the aerodynamic forces are mostly approximations and are listed in the following section, a more extensive description can for example be found in [13].

4.2.3 Derivatives of the Longitudinal Motion

4.2.3.1 Lift

The lift of the wing and the undeflected elevator is represented as

$$C_L = C_{L,2} + C_{L_\alpha}\, \alpha \tag{4.38}$$

with the lift coefficient $C_{L,2}$ at $\alpha = 0$ and the lift curve slope derived from a XFLR5 calculation.

The derivatives of the lift with respect to pitch velocity q and elevator deflection η are

$$C_{L_q} = V_{\mathrm{H}}\, \frac{1}{S\, c}\, \frac{q_{\mathrm{H}}}{q} \tag{4.39}$$

and

$$C_{L_\eta} = C_{L_{\alpha_{\mathrm{H}}}}\, \frac{S_{\mathrm{H}}}{S}\, \frac{q_{\mathrm{H}}}{q}, \tag{4.40}$$

with the horizontal stabilizer volume and its lift curve slope according to Equations 4.9 and 4.10.

4.2.3.2 Drag

The drag can not be calculated accurately with reasonable effort, although a sufficing estimation can be made. Expressing the drag as

$$C_D = C_{D,1} + k\,(C_L - C_{L,1})^2 \tag{4.41}$$

and using values from the simulation of the wing and tail using XFLR5, a first approximation of the drag can be made.

Since the fuselage is not yet considered, the non lift-dependent factor $C_{D,1}$ needs to be adjusted. The friction drag of the fuselage is calculated by considering it as a $l_\mathrm{F} = 1.3$ m long flat plate. The boundary layer is assumed to be turbulent over the whole length, since transition is likely to occur at the connection between nose and main section or even before due to roughness. The friction coefficient for a turbulent boundary layer according to Blasius is given by [101]:

$$c_\mathrm{f} = \frac{0.0572}{\sqrt[5]{Re_{l_\mathrm{F}}}} \tag{4.42}$$

where

$$Re_{l_\mathrm{F}} = \frac{\rho\, V\, l_\mathrm{F}}{\eta} = \frac{V\, l_\mathrm{F}}{\nu} \tag{4.43}$$

is the Reynolds number based on the length of the plate. With the assumed flight velocity range a Reynolds number range of $Re_{l_\mathrm{F}} = 1.34$–$2.68 \cdot 10^6$ is yielded. The Blasius law is valid for

$$5 \cdot 10^5 < Re < 1 \cdot 10^7, \tag{4.44}$$

therefore Equation 4.42 is applicable. The resulting friction coefficient c_f is based on the surface of the flat plate, respectively the fuselage, S_F and has to be converted based to the wing surface S. Additionally, the factor

$$\delta_\mathrm{F} = \frac{d_\mathrm{F}}{l_\mathrm{F}} \tag{4.45}$$

with the maximum fuselage diameter d_F is introduced to consider the pressure drag of the fuselage [90]. The resulting overall drag coefficient of the fuselage based on the wing surface is therefore given by

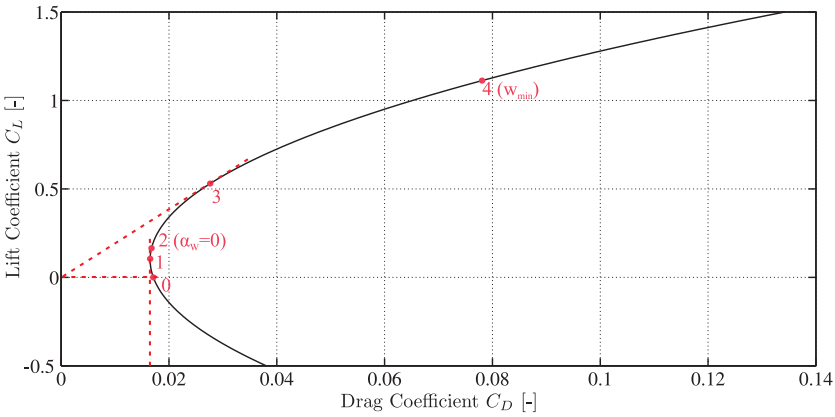

Figure 4.14: Drag polar calculated from XFLR5 simulation of wing and tail surfaces and estimation of the fuselage drag. The points marked in red are at zero lift (0), minimum drag (1), zero angle of attack (2), maximum glide ratio (3) and minimum sink speed (4). Due to the limitation of the calculation to flows without separation the point of maximum lift is not shown.

$$C_{D,\mathrm{F}} = c_\mathrm{f} \frac{\pi\, d_\mathrm{F}\, l_\mathrm{F}}{S} \left(1 + 0.5\, \delta_\mathrm{F}\right) \tag{4.46}$$

$$= \frac{0.0572}{\sqrt[5]{\frac{V\, l_\mathrm{F}}{\nu}}} \frac{\pi\, d_\mathrm{F}\, l_\mathrm{F}}{S} \left(1 + 0.5\, \delta_\mathrm{F}\right). \tag{4.47}$$

Although dependent on lift, $C_{D,\mathrm{F}} \sim C_L^{-1/10}$, the influence is small, so that a flight velocity of $V = 20$ m/s is assumed. The lift-independent drag in Equation 4.41 is adjusted.

The estimated drag polar is shown in Figure 4.14, the maximum lift-to-drag-ratio is $L/D = 19$ at a lift coefficient of $C_L = 0.53$.

4.2.3.3 Pitching Moment

The pitching moment is calculated in the form of

$$C_{\check{M}} = C_{\check{M},2} + C_{\check{M}_\alpha}\, \alpha. \tag{4.48}$$

Pitch velocity and elevator deflection inflict additional moments, the derivatives being

$$C_{\check{M}_q} = -C_{L_q} \frac{l_\mathrm{H}}{c} \tag{4.49}$$

and

$$C_{\check{M}_\eta} = -V_\mathrm{H} \frac{1}{S\,c} \frac{q_\mathrm{H}}{q}. \tag{4.50}$$

4.2.3.4 Propulsion

The thrust of the propulsion system is expressed as

$$T = D_\mathrm{thr}\, T_{i,\max} \left(\frac{V}{V_i}\right)^{-1} \left(\frac{\rho}{\rho_i}\right)^{0.75} \tag{4.51}$$

as function of throttle position D_thr, velocity V and air density ρ.

4.2.4 Derivatives of the Lateral Motion

4.2.4.1 Side Force

The side force of the vertical stabilizer and the fuselage are dependent on the yaw angle β, the derivatives being

$$C_{Y_\beta,V} = \frac{\mathrm{d}C_{Y_\mathrm{V}}}{\mathrm{d}\beta_\mathrm{V}} \frac{S_\mathrm{V}}{S} \frac{q_\mathrm{V}}{q} \tag{4.52}$$

$$= \frac{2\,\pi\,\Lambda_\mathrm{V}}{2 + \sqrt{\Lambda_\mathrm{V}^2 + 4}} \frac{S_\mathrm{V}}{S} \frac{q_\mathrm{V}}{q} \frac{\beta_\mathrm{V}}{\beta} \tag{4.53}$$

and

$$C_{Y_\beta,\mathrm{F}} = -0.2\, \frac{V_\mathrm{F}^{3/2}}{S}. \tag{4.54}$$

Since the wing has no dihedral

$$C_{Y_\beta,\mathrm{W}} = -C_D\, \beta \tag{4.55}$$

is assumed.

An additional force is created due to the rotational velocity of the vertical stabilizer during roll and yaw, with the derivatives

$$C_{Y_{\hat{p}}} = C_{Y_{\beta},\mathrm{V}} \frac{b_{\mathrm{V}}}{2\,b} \tag{4.56}$$

and

$$C_{Y_{\hat{r}}} = -C_{Y_{\beta},\mathrm{V}} \frac{l_{\mathrm{V}}}{2\,b}. \tag{4.57}$$

Since the wing has no dihedral the changed lift due to a deflection of the aileron does not induce a side force and $C_{Y_{\xi}}$ is zero.

The derivative wit respect to the rudder deflection ζ is expressed as

$$C_{Y_{\zeta}} = C_{Y_{\beta},\mathrm{V}} \frac{\partial \beta_{\mathrm{rud}}}{\partial \zeta} \tag{4.58}$$

with the rudder efficiency of $\frac{\partial \beta_{\mathrm{rud}}}{\partial \zeta}$.

4.2.4.2 Roll Moment

Since the vertical stabilizer is above the center of gravity a force on it due to a yaw angle causes a roll moment. The derivative is calculated as

$$C_{\check{L}_{\beta},\mathrm{V}} = C_{Y_{\beta},\mathrm{V}} \frac{\partial \beta_{\mathrm{V}}}{\partial \beta} \frac{l_{z,\mathrm{V}}}{2\,b}. \tag{4.59}$$

Furthermore the air flow from the side around the fuselage creates an antipodal change in angle of attack at the wing. An effective dihedral

$$\begin{aligned} \upsilon_{\mathrm{eff}} &= 3 \left(\frac{r_{\mathrm{F}}}{b}\right)^2 \left(\frac{z_0}{r_{\mathrm{F}}} \sqrt{1 - \left(\frac{z_0}{r_{\mathrm{F}}}\right)^2} + \arcsin\left(\frac{z_0}{r_{\mathrm{F}}} - \pi \frac{z_0}{b}\right)\right) \\ &= 0.0345 \end{aligned} \tag{4.60}$$

is estimated, the derivative is

$$C_{\check{L}_{\beta},\upsilon} = -\frac{4}{3} \frac{\Lambda}{2 + \sqrt{4 + \left(\frac{\Lambda}{2}\right)^2}} \upsilon_{\mathrm{eff}}. \tag{4.61}$$

The derivative with respect to the roll and yaw angular velocities are

$$C_{\check{L}_{\check{p}}} = -\frac{1}{4}\,\frac{\pi}{1+\frac{4}{\Lambda}} \tag{4.62}$$

and

$$C_{\check{L}_{\check{r}}} = -\frac{C_L}{4}\left(1+\frac{1+\sqrt{\frac{\Lambda^2}{4}+1}}{2+\sqrt{\frac{\Lambda^2}{4}+4}}\right) - C_{Y_\beta,V}\,\frac{l_\mathrm{V}}{2\,b}\left(\frac{l_{z,\mathrm{V}}}{b}-\frac{l_\mathrm{V}}{b}\,\alpha\right). \tag{4.63}$$

The effect of aileron and rudder deflection are described with

$$C_{\check{L}_\xi} = -\frac{4}{3}\,\frac{\Lambda}{2+\sqrt{4+\left(\frac{\Lambda}{2}\right)^2}}\,\frac{\alpha}{\xi}\left(1-\frac{2\,{b_\mathrm{ail}}^2}{b}\right)^{3/2}, \tag{4.64}$$

and

$$C_{\check{L}_\zeta} = C_{Y_\beta,\mathrm{V}}\,\frac{l_\mathrm{V}}{2\,b}\,\frac{\beta_\mathrm{V}}{\zeta}\left(\frac{l_{z,\mathrm{V}}}{l_\mathrm{V}}-\alpha\right). \tag{4.65}$$

4.2.4.3 Yaw Moment

The yaw moment is influenced by the yaw angle, the impact of the fuselage is estimated by the factor

$$k_\mathrm{F} = -0.9. \tag{4.66}$$

The derivative is then given by

$$C_{\check{N}_\beta} = -\frac{2\,k_\mathrm{F}\,V_\mathrm{F}}{S\,s} - C_{Y_\beta,\mathrm{V}}\,\frac{l_\mathrm{V}}{2\,b}\,\frac{\beta_\mathrm{V}}{\beta}. \tag{4.67}$$

The derivatives with respect to the roll and yaw velocity are

$$C_{\check{N}_{\check{p}}} = -\frac{C_L}{4}\,\frac{1-\frac{2}{\Lambda}}{1+\frac{4}{\Lambda}} - C_{Y_\beta,\mathrm{V}}\,\frac{l_\mathrm{V}}{2\,b}\,\frac{b_\mathrm{V}}{2\,b} \tag{4.68}$$

and

$$C_{\check{N}_{\check{r}}} = -\frac{2}{3}\,C_D + C_{Y_\beta,\mathrm{V}}\,\frac{l_\mathrm{V}}{2\,b}\,\frac{l_\mathrm{V}}{2\,b} \tag{4.69}$$

Due to a deflection of the ailerons also the drag changes, therefore differential ailerons are used to minimize the effect, which is neglected here.

The effect of a rudder deflection is estimated by

$$C_{\check{N}_\zeta} = -C_{Y_\beta,\mathrm{V}} \frac{l_\mathrm{V}}{2\,b} \frac{\beta_\mathrm{V}}{\zeta}. \tag{4.70}$$

4.2.5 Moments of Inertia

To calculate the moments of inertia the plane was represented by rectangular segments of appropriate densities, according to the individual components. Since the aircraft is symmetrical the terms J_{xy} and J_{yz} are zero, furthermore J_{xz} was neglected, resulting in the body coordinate system being a principal coordinate system. The inertia of the segments was calculated and superimposed, yielding the total moments of inertia:

$$\mathbf{J} = \begin{bmatrix} 1.522 & 0 & 0 \\ 0 & 1.479 & 0 \\ 0 & 0 & 2.741 \end{bmatrix} \ \mathrm{kgm}^2. \tag{4.71}$$

4.2.6 Simulation

To design the flight controller a simulation of the aircraft is needed, which has to be linearized for a state space representation. The general form is

$$\dot{\vec{x}} = \mathbf{A}\,\vec{x} + \mathbf{B}\,\vec{u} \tag{4.72}$$

$$\vec{y} = \mathbf{C}\,\vec{x} + \mathbf{D}\,\vec{u} \tag{4.73}$$

with $\mathbf{A}$ being the state matrix, $\mathbf{B}$ being the input matrix, $\mathbf{C}$ being the output matrix and $\mathbf{D}$ being the feedthrough matrix. The vector $\vec{x}$ is the state vector, $\vec{u}$ the control vector and $\vec{y}$ the output vector.

The linear state space representation is derived from the equations discussed in the previous section and was implemented as simulation using the MATLAB Simulink software.

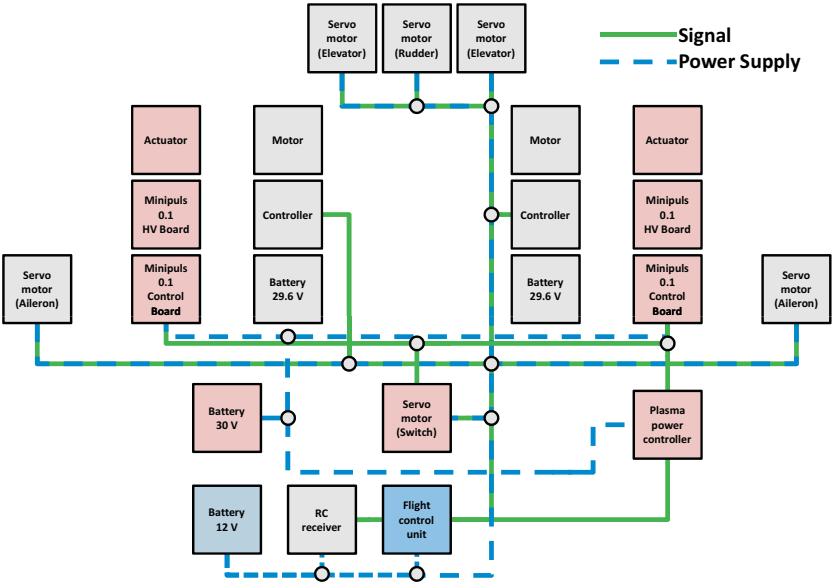

Figure 4.15: Overview of the electrical system of the UAV. Components of the RC equipment are colored grey, of the flight control system blue and of the plasma actuation system red.

4.3 Electrical Components

4.3.1 Overview

The electrical components of the UAV can be attributed to three main systems, the radio control equipment, the flight control system and the plasma actuation system. These systems are connected to each other as depicted in Figure 4.15, but can also interact due to undesirable effects, namely electromagnetic interference, as discussed in Section 4.3.5.

4.3.2 Radio Control Equipment

Since remote controlled model aircraft are a mass-market, many sophisticated, reliable and relatively cheap components are available. These were

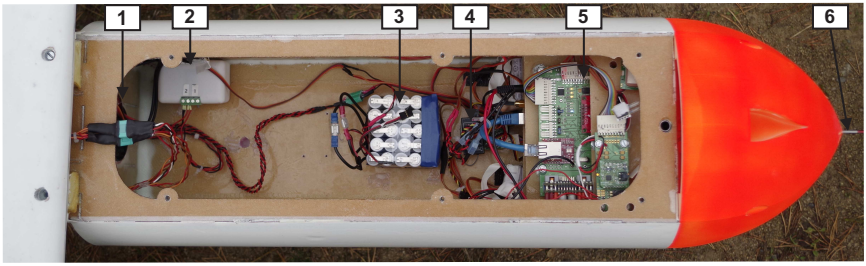

Figure 4.16: Electrical system installed in the payload section of the fuselage. Visible are the servo connections to wing and tail (1), the plasma switch(2), the battery of the plasma actuator system (3), the receiver and servo board (4), the flight control system (5) and the base of the pitot-static tube (6). The flight control system consists of extension board, GPS receiver and airspeed sensor mounted at the top, the interface board beneath, and the flight-PC and batteries, not visible here, in the lower platforms.

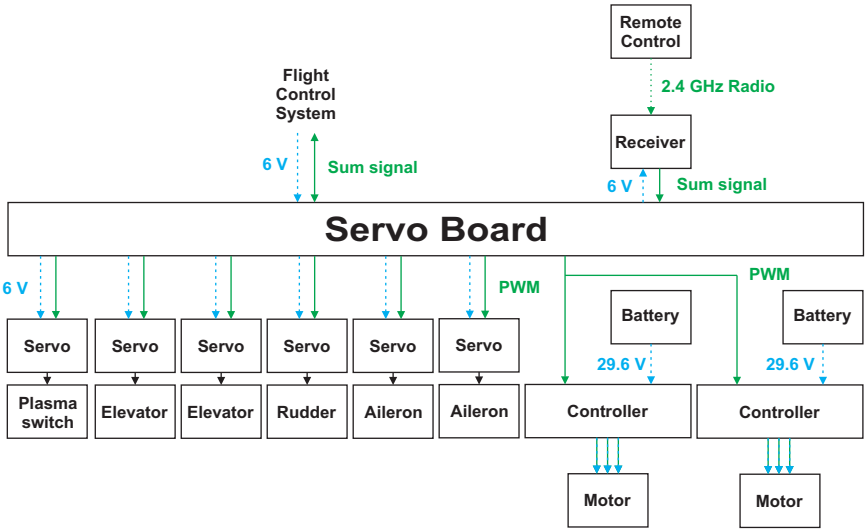

Figure 4.17: Overview of the radio control system of the UAV.

used for large parts of the control system of the UAV. In the following section the relevant parts and their technologies are introduced where necessary, while other parts are considered as black boxes.

The remote control setup for the UAV consists of the following components:

- The remote control, operated by the pilot.
- A satellite receiver and the servo board of the flight control system, which converts the signal from the remote control to a signal for the servo motors and motor controller.
- Servo motors for each control surface, as well as for the plasma actuation switch.
- Electric motor, electronic speed control and batteries for the propulsion system.
- Batteries as power supply for the receiver and servo motors, via the flight control system.

4.3.2.1 Remote Control

A typical hand-held radio transmitter is used, consisting of two control sticks for elevator, aileron, throttle and rudder, and switches to control the plasma actuation system, activate the autonomous control and to modify the deflections of the control surfaces. Seven channels are transmitted for elevator, rudder, each aileron, throttle, autopilot and the high voltage generators. To program the control and to display crucial information, such as battery voltage and flight time, a display screen and buttons are installed.

The inputs are converted to signals for each channel and sent to the receiver via a radio connection. The remote control operates in the 2.4 GHz band which was found to be insensitive to interferences from the plasma actuation system. Additional features to ensure safety, such as channel shifting and error correction techniques are used by default. The range of typical setups in the 2.4 GHz spectrum is 2 to 3 km in ideal conditions, but can be reduced by radio shadows due to the plane or objects on the ground, other systems operating in the spectrum, like other radio controls or WLAN, and electromagnetic disturbances.

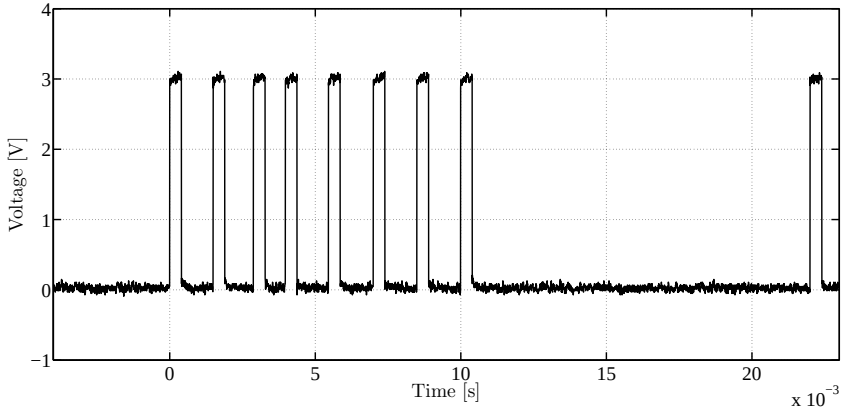

Figure 4.18: Remote control sum signal with one signal for each control channel from satellite receiver. The pulse width is determined by the combined length of the high part of 400 µs and a variable length low part, resulting in a length of 1000 to 2000 µs. The servo board splits the received signal into the separate signals, converts them to a PWM signal and outputs them to the according servo motors.

4.3.2.2 Receiver and Servo Board

The receiver used is a satellite receiver normally used as backup system in the case of radio shadows at the main receiver. In contrast to a normal receiver it does not split the signal for each servo but instead transmits a sum signal as depicted in Figure 4.18 to the main receiver.

The sum signal is in this case needed as input for the servo board of the flight control system. The servo board evaluates if the aircraft is to fly autonomously or manually, and converts the signal from either the flight control unit or from the receiver to a pulse width modulated signal for each servo motor and motor controller. In addition the servo board supplies the servos with power.

In the case of a radio failure the receiver outputs predefined signals in a fail-safe mode, i.e. killing the engine and adjusting the elevator to glide to the ground with minimal damage.

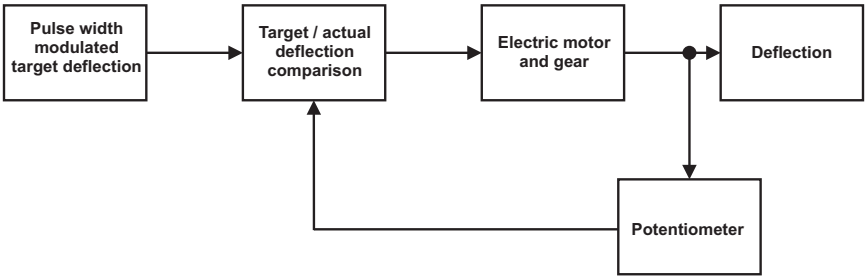

Figure 4.19: Schematic of a servo motor. The pulse width modulated target deflection is compared to the actual deflection, as measured by a potentiometer, and an according impulse is given to the electric motor. The comparison and the control of the motor are accomplished by a small electronic circuit board.

4.3.2.3 Servo Motors

A servo motor consists of an electronic board, a direct current electric motor, a gear turning a crank arm and a potentiometer to detect its actual deflection. This deflection is compared to the target deflection from the receiver, to this avail the pulse width modulated signal from the receiver is evaluated. This happens on the electronics board of the servo, which outputs an according impulse to the electric motor.

There are different types of servos, which can be compared by their torque, speed, travel, dead band width, weight, dimensions, standing torque, operating voltage and idle, running and stall currents. Different bearing, gear materials, motor and potentiometer types and electronics are used. Another distinction is between analog and digital servos, a digital servo actuates with a much higher frequency, resulting in higher speed and torque.

The servo motors were chosen according to the expected maximum loads. To this avail the aerodynamic loads of the control surfaces at maximum deflections and maneuvering speed were estimated. The usable deflections and the according torque at the hinge were calculated using XFLR5.

For the ailerons a maximum upward deflection of $\xi = -15°$ and downward deflection of $\xi = +10°$ was chosen, as discussed in Section 4.1.1.5. As can be seen in Figure 4.22, the maximum expected hinge moment coefficient is expected to be around $c_{H_{\text{ail}}} = 0.016$ before stall occurs. The resulting hinge moment is calculated as

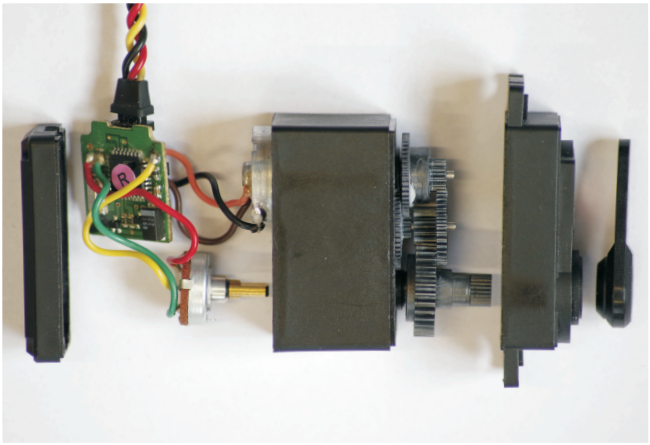

Figure 4.20: Exploded view of a servo motor, consisting of electronics board, motor, gear, crank arm and potentiometer.

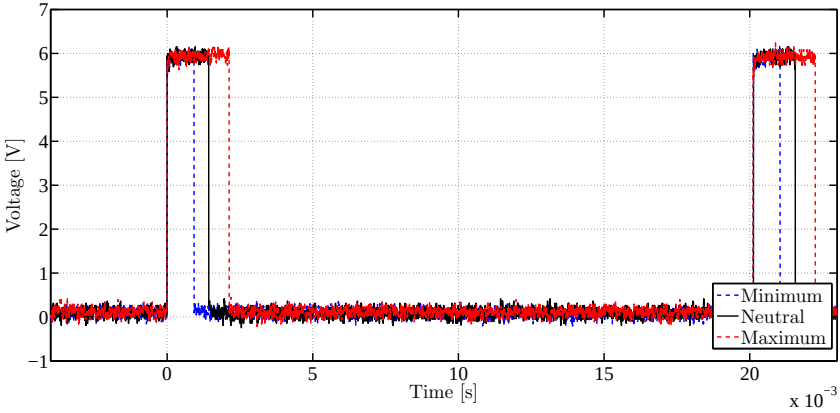

Figure 4.21: Pulse width modulated servo signal, the pulse width between 1000 and 2000 µs determines the servo target position, with the neutral position being at 1500 µs. The time between pulses amounts to approximately 20 ms.

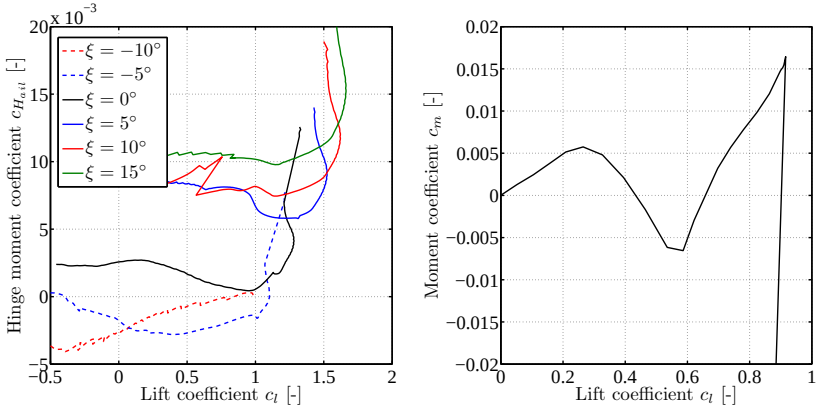

(a) Aileron (b) Elevator

Figure 4.22: Hinge moment coefficients for different deflections of the aileron at $Re = 500.000$, respectively the elevator at $Re = 400.000$ from XFLR5 . The unsteady course of the plots result from flow separations which can not be calculated reliably.

$$H_{\text{ail}} = \frac{\rho}{2} V_{\text{A}}^2 S_{\text{ail}} c_{\mu,\text{ail}} c_{H_{\text{ail}}} \tag{4.74}$$

with S_{ail} being the area of the aileron and $c_{\mu,\text{ail}}$ its mean aerodynamic chord. For the rudder a similar consideration was made, the findings are presented in Table 4.5.

In the case of the elevator a slightly different method has to be used since it is an all-flying configuration. Here the moment coefficient $c_{H_{\text{ele}}}$ around the hinge axis at 25% x/c has to be considered, as shown in Figure 4.75. The moment is calculated as

$$H_{\text{ele}} = \frac{\rho}{2} V_{\text{A}}^2 S_{\text{ele}} c_{\mu,\text{ele}} c_{H_{\text{ele}}} \tag{4.75}$$

with S_{ele} and $c_{\mu,\text{ele}}$ being the area and mean aerodynamic chord length of the whole elevator.

The nose gear servo is actuated together with the rudder and helps steering during take-off and landing.

Table 4.5: Overview over the hinge moments at the control surfaces and used servo motors. Missing values are not assessable or not specified by the manufacturer.

	Aileron	Rudder	Elevator	Nose gear	Plasma switch
Abbreviation	ail	rud	ele	nog	PA
Hinge moment [Nm]	0.05	0.006	0.16	-	-
Hinge deflection [°]	−15/+10	±15	±15	±20	±45
Servo name	2x Hitec HS-6635 HB	Hitec HS-6635 HB	2x Hitec HS-5495 BH	Hitec HS-81	Hitec HS-81
Servo torque [Nm]	0.06	0.06	0.064	0.03	0.03
Servo deflection [°]	±45	±45	±45	±45	±45
Servo voltage [V]	6	6	6	6	6
Servo running current [A]	0.5	0.5	-	0.28	0.28
Servo stall current [A]	2.5	2.5	-	-	-

All servos combined have a running current of about 3 A, the measured current during idle is around 0.5 A. The connections to the servos are split at the crossing to the wing and tail section for easier mounting.

4.3.2.4 Propulsion Motors

The electric motors most used in model airplanes today are brushless direct current motors (BLDC). They are synchronous motors and have the advantage of reduced maintenance and less friction over brushed electric motors, but a more complicated electronic controller is needed to drive them. The motor itself consists of the stator with coils, driven by the controller, and the rotor with permanent magnets. The rotor can either be in the core (called in-runner) or surrounding the stator (out-runner), the latter being used in this setup.

The propulsion system is controlled with a pulse-width modulated signal, as the servo motors. The controller produces an alternating current signal for each coil, to synchronize the magnetic field the position of the rotor has to be known. This can either be accomplished by Hall effect sensors or by measuring the electromagnetic force (EMF) in the currently undriven coil, the latter, also termed sensorless, being used in this case. To detect the rotor position and direction of rotation during start-up an arbitrary phase is used, which can result in the motor turning backwards for an instant.

The efficiency of BLDC motors is usually very good, but due to the controller additional losses occur, especially under partially-load operational conditions. To minimize conduction losses, motor, controller and batteries should be positioned close to each other. Due to the relatively low voltages of batteries the electric current is very high, in this case temporarily up to 70 A at 29.6 V.

A BLDC motor is usually characterized by nominal voltage V_{nom}, maximum current I_{max} and the motor speed constant

$$k_v = \frac{\omega}{V} \tag{4.76}$$

usually measured in rpm/V, giving the theoretic maximum speed without load for a given supply voltage. The speed constant is used to estimate the speed the motor will turn with the chosen battery and to match the motor with the propeller for different flight envelopes, e.g. a small, fast turning propeller with small pitch for aerobatics.

Until recently the most common battery types were nickel-cadmium and nickel metal hydride. For propulsion purposes they were largely replaced

Table 4.6: Overview over the different battery systems used for model aircraft. All values are typical values for practical use of commercially available products. Charge and discharge rates are given as multiples of the capacity C of the battery per hour.

	Nickel cadmium	Nickel metal hydride	Lithium polymer	Lithium iron phosphate
Abbreviation	NiCd	NiMH	LiPo	$LiFePO_4$
Nominal voltage [V]	1.2	1.2	3.7	3.3
Maximum voltage [V]	1.45	1.6	4.23	3.6
Minimum voltage [V]	0.85	1	3	2.8
Specific energy [Wh/kg]	40–60	60–120	100–200	90–110
Maximum charge rate [C 1/h]	1–3	1–2	1–15	4
Discharge rate [C 1/h]	< 40	3–20	20–130	30

by lithium-polymer batteries, offering a much better specific energy and high charge and discharge rates. A disadvantage is their sensitivity to mechanical and thermal damage and overly high currents, which can result in a malfunction and thermal runaway. The batteries usually consist of several pouch cells, interconnected for a higher voltage. Alternatives are lithium iron phosphate batteries, which feature a metal case and are thereby much more resistant to misuse, but feature a lower specific energy.

The layout was conducted with the parameters from Section 4.1.3 and the software tool DriveCalculator 3.4, a motor analysis tool with an extensive database of power trains for model aircraft. Two Hacker A-50-12L V2.1 14 Pole BLDC motor in combination with MasterSPIN 75 Pro OPTO controllers are used. The speed constant of the motors is $k_v = 348$ rpm/V and their maximum current 70 A. The controllers were modified using a cooling element and submitted to forced ventilation. At a voltage of 29.6 V, provided by two robbe ROXXY POWER 4-3300 ZX25C lithium polymer battery packs, each motor provides a short-term maximum power

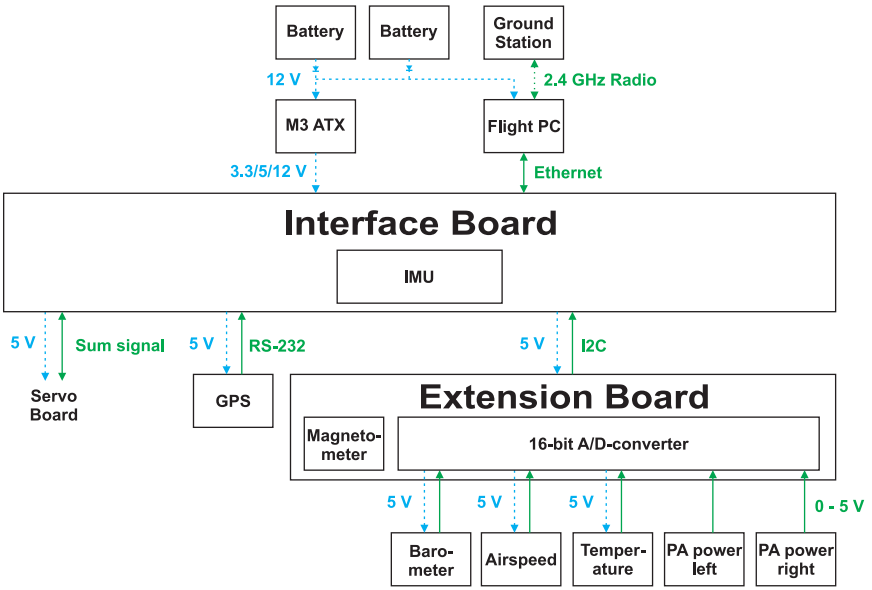

Figure 4.23: Overview of the flight control system of the UAV.

of 1650 W.

4.3.3 Flight Control System

4.3.3.1 Overview

The flight control system used for control and data acquisition on the UAV was developed by the Institute for Flight Systems and Automatic Control (FSR) at the Technische Universität Darmstadt [78]. It is a highly modular and flexible system which is successfully used on different platforms, including quadcopter and ground vehicles [49].

The two central components are the interface board and the miniature flight PC. The interface boards connects to all sensors, either directly or via extension boards, including the servo motors and the remote control receiver. It is connected via ethernet to the flight PC which records the data when required and uses it to compute the actual flight situation and the required servo outputs for autonomous control. The data can also be sent on enquiry to the ground station for telemetry purposes via WLAN

and saved onboard, enabling a complete post-flight analysis. The ground station consists of a portable computer and a WLAN router with three high gain omnidirectional antennas for maximum coverage.

As power supply for the flight control system, including the servo motors, NiMH batteries with reduced self-discharge are used. For redundancy two battery packs, separated by diodes, are installed, each consisting of 10 cells with a capacity of 1900 mAh in series.

4.3.3.2 Sensors, Data Acquisition and Processing

The sensors are installed on the interface board, on the extension board or connected to them. They include an inertial measurement unit, magnet field sensor, barometer, air speed sensor, temperature sensor, GPS device and A/D-converter inputs for discretionary sensors, as shown in Table 4.7. To counter vibrations, especially important for the inertial measurement unit, all boards are installed on rubber dampers.

The 6-DOF inertial measurement unit is installed directly on the interface board. To measure rotations a ST microelectronics LPR530AL dual axis MEMS gyroscope for roll and pitch axis and a LY530ALH single axis gyroscope are used, which allow measurements of angular velocities of up to $\pm 300°$ /s. An Analog Devices ADXL335 3-axis capacitive accelerometer measures acceleration of up to ± 3.6 g.

Directly connected to the interface board via a RS-232 serial connection is a GPS receiver Navilock NL-551ERS with a u-blox5 UBXG5000/UBXG0010 chip set. The determined position has a circular error probability of 5 m, while the velocity is up to 0.1 m/s accurate, when the number of received satellites is sufficient. Due to safety issues the maximum height and velocity up to which the receiver operates are limited to $18,000$ m, respectively 515 m/s.

Also connected to the interface board is the servo board. Equipped with an ATMEL ATMega 8 microcontroller, signals from the receiver are imported and signals to the servo exported.

On the extension board a 3-axis magneto-inductive magnetic sensor module PNI MicroMag3 is installed. Also mounted on the extension board is a Texas Instruments ADS8344 0–5 V analog-digital converter, featuring 8 channels with a resolution of 16 bit and 100 kHz conversion rate. All channels are equipped with an appropiate RC circuit to filter noise.

Connected to this converter and stationary mounted on the board are an Analog Devices TMP 36 temperature sensor and a Motorola MPXA6115A barometric pressure sensor.

Table 4.7: Boards of the flight control system and respective sensor data.

Board	Sensor	Measurand	Symbol
Interface board	Inertial measurement unit	Roll rate	$\check{p}$
		Pitch rate	$\check{q}$
		Yaw rate	$\check{r}$
		x-acceleration	$\dot{u}$
		y-acceleration	$\dot{v}$
		z-acceleration	$\dot{w}$
RS-232 to interface board	GPS receiver	GPS latitude (WGS 84)	φ_{gs}
		GPS longitude (WGS 84)	λ_{gs}
		GPS altitude (WGS 84)	h_{gs}
		GPS velocity u	u_{gs}
		GPS velocity v	v_{gs}
		GPS velocity w	w_{gs}
		GPS status	
		GPS service	
		GPS covariance	
		GPS covariance type	
Servo board	A/D-converter	Aileron deflection left	ξ_{l}
		Aileron deflection right	ξ_{r}
		Elevator deflection	η
		Rudder deflection	ζ
		Throttle position	D_{thr}
		Autopilot switch	S_{AP}
		Plasma actuator switch	S_{PA}
Extension board	Magnetometer	Magnetic field x-comp.	B_x
		Magnetic field x-comp.	B_y
		Magnetic field z-comp.	B_z
	Temperature sensor	Temperature	T
	Barometer	Static pressure	p
	Airspeed sensor	Dynamic pressure	q
	PA power measurement	PA power left	$P_{\mathrm{PA,l}}$
		PA power right	$P_{\mathrm{PA,r}}$

Additionally for the UAV an airspeed sensor Sensortechnics HCLA12X5DU differential pressure sensor was installed. It can measure dynamic pressures up to 1250 Pa, correspondent to 45.2 m/s. The static and total pressure are picked off by a KIMO Instruments type L 3 mm diameter pitot-static tube 150 mm in front of the aircraft nose. The tip of the probe is elliptical, the error is stated as less than 1% while maintaining an angle of below 10° towards the flow direction. Due to the wings incidence the angles of attack at the fuselage are in the range of -5 to $+10°$. An inferior accuracy is therefore only expected at very high angles of attack or yaw.

Furthermore the plasma actuator power measurement circuit, as described in Section 4.3.4.2, is connected to the analog-digital converter. Thereby the power output and health of the actuator system can be monitored during flight and evaluated during the post-flight data analysis.

All data is passed via an ethernet connection to the fitPC-2i flight PC. It has an Intel Atom Z530 32 bit single core processor with a clock speed of 1.6 GHz, 2GB DDR2-533 memory, two Realtek RTL8111C-VC-GR ethernet controllers and a 2.4GHz Qcom LR802UKN2 wireless LAN module. A Corsair Force CSSD-F60GB2-BRKT 60GB SSD hard drive was retrofitted to ensure resistance to physical shocks, especially during ground operation. A Linux Ubuntu 12.04.3 operating system is installed, as well as the ROS Robot Control Software, the Orocos Open Robot Control Software toolchain for real-time components and the UxV Control System developed at the Institute for Flight Systems and Automatic Control (FSR) of the TU Darmstadt. The ground station portable computer features the same software as the flight PC.

The data is converted from input voltages or digital values to physical dimensions, where necessary. Offset and conversion factors are determined by the sensor specifications or a calibration. The attitude, velocity and position of the aircraft is then estimated by an extended Kalman filter [88, 89], GPS and magnetic field sensor data are used to suppress drifting. The raw and processed data is published to the network in the form of different topics, each allocated with a time stamp. Additionally the data is stored on demand and can be converted into output files for each topic, which can be post-processed with MATLAB or other programs.

In Section 5.2 the measured quantities and their characteristics, such as sample rate and accuracy, as well as the converted output data are described and analyzed.

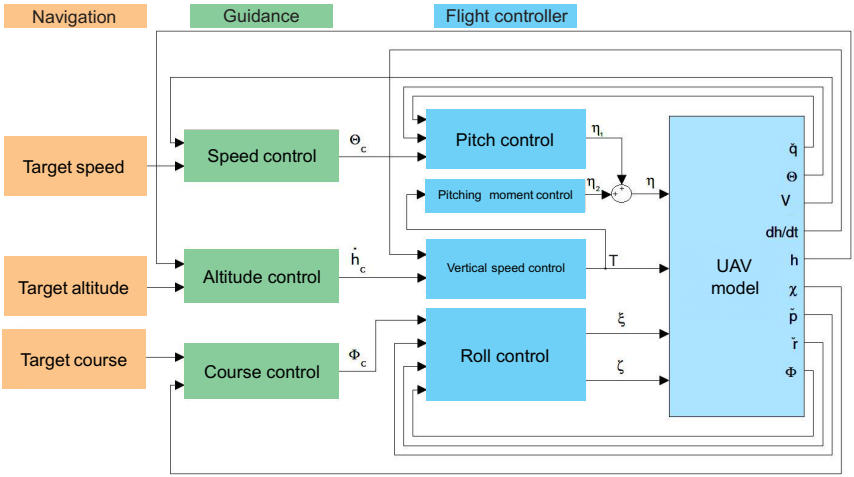

Figure 4.24: Overview of the flight controller.

4.3.3.3 Flight Controller

The controller for the autonomous flight control unit were designed and implemented using MATLAB Simulink Release 2011b, a graphical environment to analyze and design systems within MATLAB. It was configured and tested with the help of a simulation, derived from the parameters described in 4.2.

Different sensor inputs are used to compute the actual flight situation, which are used as inputs for the control loop. The control algorithm is divided into a navigation, autonomous guidance and flight controller loop, arranged in a cascade, as shown in Figure 4.24. The navigation controller defines a target speed, altitude and course, based on destinations input by the operator and is not discussed in detail here. Speed, altitude and course are controlled by the autonomous guidance controller on the base of these values, calculating the required pitch angle θ_c, vertical speed $\dot{h}_c$ and roll angle ϕ_c. The most important for the flight experiments is the flight controller, described below in detail, longitudinal and lateral motion can thereby be decoupled.

The longitudinal motion can be characterized by airspeed and altitude, respectively vertical speed, of the aircraft. The elevator deflection is used to control the airspeed of the plane, the vertical speed is controlled by

the power of the propulsion system. Since the propulsion also causes a pitching moment, due to the effects described in Section 4.1.3, it has to be considered for pitch control.

The innermost structure of the pitch controller is the pitch damper, controlling the elevator deflection based on the pitch rate. Due to a positive pitch rate a positive elevator deflection and thereby a negative pitching moment is employed to counter the phugoid mode. The pitch controller itself has a proportional and an integral part to reach the target pitch angle without residual steady-state error. The pitch angle is limited to $\pm 30°$, the elevator deflection to $\pm 10°$. Similarly all control surface deflections are limited to an amount that ensures that the physically maximal deflections are not exceeded and the plane cannot fly too severe manoeuvres. Connected ahead of the pitch controller is the speed controller, also of the PI-type. The acceleration is limited with the help of a PT1-filter to ± 1 m/s^2, with a time constant of 3 s to dampen velocity changes and achieve a stable flight behavior.

The vertical speed controller is the innermost cascade of the altitude controller, the vertical speed is adjusted by the throttle position. To achieve a sufficiently dynamic behavior, especially during turning, a PID-controller is implemented. The altitude controller itself is purely proportional and limited to a vertical speed of ± 3 m/s.

As previously mentioned, the throttle setting also has a direct, significant influence on the pitching moment, without an additional controller the aircraft enters an oscillation when changing the throttle position. Although stable and slowly decaying, this oscillation is undesirable, therefore a controller is used to adjust the elevator deflection accordingly. A P-type controller with a negative gain and a low-pass filter to suppress short-period oscillations is sufficient.

The control of the lateral movement of the UAV, i.e. yaw and roll control, can be decoupled from the longitudinal movement. The roll control uses the ailerons to fly a given heading, while the yaw control uses the rudder to avert a sideslip of the plane.

The yaw damper is implemented to lessen the Dutch-roll tendency of the aircraft, the yaw rate is countersteered by a rudder deflection. To allow yaw rates during turning a high-pass washout filter with a time constant of 1 s is used. The damper is a P-controller with a gain adjusted to the frequency of the Dutch roll mode of the UAV, the maximum deflection of the rudder is limited to $\pm 15°$.

To change the course, the plane has to fly a turn by rolling and thereby

Table 4.8: Parameters for the individual controllers of the flight control system.

Controller	k_p	k_i	k_d	Filter
Longitudinal				
Speed	−0.06	0.45		PT1 3 s
Pitch	−0.9	0.18		
Pitch damper	−0.6			
Pitching moment	−0.3			PT1 0.5 s
Altitude	0.3			
Vertical speed	0.08	0.05	0.07	
Lateral				
Course	1			
Roll	−1.8	−0.4	−0.4	PT1 1 s
Roll damper	−0.09			
Yaw damper	0.6			Washout 1 s

tilting the lift vector to the inside of the turn. The roll damper, as the innermost cascade, is a P-controller. The roll controller itself is of the PID-type, with a PT1-filter with a time constant of 1 s for the target roll angle. Again limitations were set to ±15° /s change in course, ±30° bank angle and ±10° aileron deflection.

The outermost cascade of the lateral controller is the course controller, since the process shows an integral behavior, a P-controller is sufficient. With the maximum allowed roll angle a course change of ±15° /s is possible.

4.3.4 Plasma Actuator System

Although other configurations are possible, up to date only the Minipuls 0.1 actuator system was used for in-flight experiments.

The system is activated by the remote control system via the plasma switch servo, which can be set to three different positions and is connected to the inhibit input of the Minipuls 0.1 high voltage generators. Therefore either the left or right generator can be switched on, or both if wired accordingly. The switch is constructed as fail-safe, to ensure a switch-off of the high voltage generators in case of disturbances in the RC system.

A battery pack of 25 NiMH cells in series with a nominal voltage of 30 V and a capacity of 1900 mAh is used. Although this setup is rather heavy

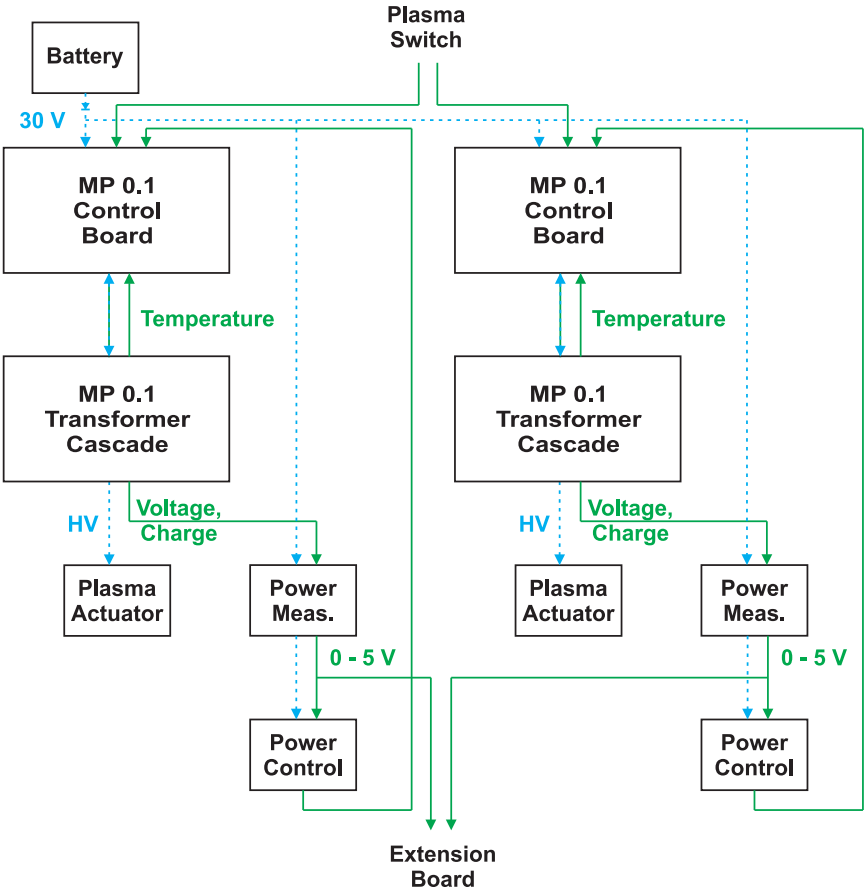

Figure 4.25: Overview of the plasma actuation system of the UAV.

and stores considerably more energy than needed for the experiments, it was proven necessary to ensure a stable power supply and minimize voltage fluctuations.

4.3.4.1 High Voltage Generators

The GBS Elektronik Minipuls 0.1 high voltage generator is a further development of the Minipuls 0 generator, specifically designed for the use in the UAV in terms of size and weight. It consists of a control board which creates a driving signal of the desired frequency and amplitude and a transformer cascade which amplifies the signal and supplies the high voltage to the actuators. Both boards combined weigh around 340 g, excluding cables and measure 64×105 mm, respectively 73×153 mm.

A voltage V_{pl} of up to 12 kV can be supplied at frequencies of 5 to 20 kHz and an output power of 30 W. An inhibit switch activates the generator when connected to ground, in the UAV this switch is actuated by a servo motor.

To protect the boards a 2 A fuse is installed as well as a temperature sensor on the cascade and a corresponding switch on the control board with adjustable switch-off temperature. Although during flight the temperatures remain relatively low due to the forced ventilation, overheating can occur on the ground. As protection against excessive output voltages a spark gap is installed on the transformer board.

Several parameters are adjustable by potentiometers on the control board, or by voltages supplied to the respective inputs, including phase, controlling the amplitude of the signal, burst frequency and duty cycle. The plasma frequency is only manually adjustable by potentiometers, since the resonance frequency is largely fixed for an actuator configuration.

4.3.4.2 Power Measurement

To measure the electrical power consumption of the plasma actuators an analog measurement circuit was developed. A common method for the online characterization of DBD actuators based on voltage-charge-cyclograms, also called Lissajous figures, is described in [67]. The consumed electrical power is calculated as

Table 4.9: Parameters and specifications of the Minipuls 0.1 high voltage generators.

General			
Control board mass		83 g	
Control board size		64×105 mm^2	
Transf. cascade mass		252 g	
Transf. cascade size		73×153 mm^2	
Env. temperature	T	0–35 °C	
Env. humidity	rh	0–80%	
Input			
Voltage	V_I	15–35 V	
Power	P_I	$\leq$ 30 W	Maximum mean power
Plasma			
Voltage	V_pl	$\leq$ 12 kV	Man. & ext. adjustable
Frequency	f_pl	5–20 kHz	Man. adjustable
Nominal load	C_pl	50/100 pF	
Pulsed operation			
Duty Cycle	DC_b	0–100%	Man. & ext. adjustable
Burst frequency	f_b	10–230 Hz	Man. & ext. adjustable

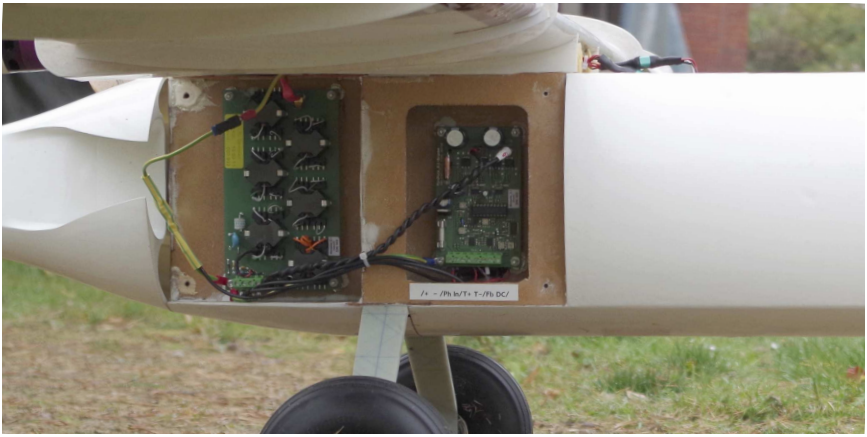

Figure 4.26: Minipuls 0.1 installed in the side of the fuselage. The control board is mounted ahead of the transformer cascade, the covering, removed in this photograph, features air ducts for forced ventilation of both boards.

$$P_{\mathrm{PA}} = f_{\mathrm{pl}} \oint Q(t)\,\mathrm{d}V \tag{4.77}$$

$$= f_{\mathrm{pl}} \oint C_{\mathrm{C}}\,V_{\mathrm{C}}(t)\,\mathrm{d}V. \tag{4.78}$$

To measure the charge $Q(t)$ of the actuator a capacitor and a large resistance are installed in parallel in the ground connection of the actuator, with C_{C} and $V_{\mathrm{C}}(t)$ being the capacity of, respectively the voltage across the probe capacitor. Although the signal-to-noise ratio of the thus obtained power consumption is superior compared to other methods, further processing of the measured data, i.e. filtering, is needed.

In this work a computationally less extensive way was chosen, the power is directly derived as

$$P_{\mathrm{PA}} = V_{\mathrm{pl}}(t)\,I_{\mathrm{pl}}(t) \tag{4.79}$$

$$= V_{\mathrm{pl}}(t)\,C_{\mathrm{C}}\frac{\mathrm{d}V_{\mathrm{C}}(t)}{\mathrm{d}t}. \tag{4.80}$$

The current $I_{\mathrm{pl}}(t)$ is measured using the previously described probe capacitor, the voltage supplied to the actuator $V_{\mathrm{pl}}(t)$ by a bleeder installed on the Minipuls 0.1 generator. Both signals, $V_{\mathrm{pl}}(t)$ and $V_{\mathrm{C}}(t)$, are low-pass filtered with a cut-off frequency of 10.7 kHz, but maintaining their phase difference to each other. The capacitor voltage is then differentiated to yield the current $I_{\mathrm{pl}}(t)$ and both signals multiplied by a AD734 circuit. The result is again low-pass filtered by an eight-order MAX293 with a cut-off frequency of 98 Hz to obtain a mean power over several cycles, and amplified to be used as input for the actuator power controller and the data acquisition system.

4.3.4.3 Control of Actuator Output Power

Due to changing atmospheric conditions, namely temperature, pressure and humidity, deterioration of the actuator or declining supply power, the actuator output power may change. However, for the experiments the power should be kept constant, therefore a controller was implemented.

A microcontroller Arduino Due, based on the Atmel SAM3X8E ARM Cortex-M3 CPU, is used on the UAV. The controlled variable is the voltage from the power measurement circuit described above, to remove scattering a moving average is generated. A PID-controller is used to regulate the power according to a target value set by a potentiometer. Since the desired power output for the experiments is usually at the upper limit of the capability of the system, an overshoot has to be avoided to protect high voltage generator and actuator.

4.3.5 Provisions against Electromagnetic Interference

Due to the high voltage, high frequency operation of the plasma actuator electromagnetic emissions from the actuator, its cables and the high voltage generator occur at various frequencies and strengths. These can be picked up by other electrical systems of the UAV in the form of disturbances and possibly induce malfunction and damages of differing degree, posing a danger to the aircraft and surroundings.

The most critical component in this regard is the remote control system. As can be seen in Figure 4.17, the disturbances can act on different critical systems and connections of the RC system, most mentionable the radio and the cable connections to the servo motors. Nonetheless, also less critical effects, such as the corruption of measurement data from the flight control system, can negate the suitability of the UAV as flight test platform for

plasma actuators. Therefore extensive tests of the electromagnetic interference were conducted prior to the construction of the aircraft and measures determined to ensure a fail-safe operation.

It was established that the plasma actuator system emits disturbances at different frequencies and intensities [21]. In the near-field of the source conductive, inductive and capacitive coupling are relevant, in the far field only radiative coupling occurs. The radius, above which the far-field is prevalent, is approximately [86]

$$r_{\text{far}} \approx 2\,\lambda \tag{4.81}$$

$$\approx \frac{2\,c}{f} \tag{4.82}$$

with c being the speed of light and $f \approx 50$ MHz [21] the maximum measured frequency of significant disturbance. With a resulting far field radius of $r_{\text{far}} \approx 12$ m the UAV itself can be considered as being in the near-field, below the relevant coupling mechanisms and provisions are introduced.

If source and victim are directly connected via a cable or a conducting material, conductive coupling occurs. In the case of the UAV the plasma system and other components are only connected via an analog-digital converter input to measure the actuator power. To this avail also the grounds of the batteries are connected to establish a common potential.

An inductive coupling occurs if a live lead induces a voltage in another lead due to its changing magnetic field, the signal of the victim is overlain by the induced voltage. Corneli [21] showed that the induced magnetic field is relatively weak and therefore not the primary coupling mechanism.

Nearby cables with different potentials can act as capacitor. Due to a change in the potential the electric field changes and a current is induced. This can especially happen in the servo cables in the wing sections, where high voltage cables and actuators are parallel and adjacent.

A fundamental feature for the abatement of disturbances is the spatial strength of the magnetic and electric field. For a live lead in vacuum the Biot-Savart law gives the magnetic field as a function of the distance r from the lead:

$$\Delta\vec{B} = \frac{\mu_0\, I}{4\,\pi\, r^3}\,\Delta\vec{s} \times \vec{r}. \tag{4.83}$$

The accordant function for the electric field is

$$\vec{E} = \frac{\lambda}{4\,\pi\,\varepsilon_0\,\varepsilon_\mathrm{r}}\,\frac{\vec{r}}{r^2}. \tag{4.84}$$

Evidently magnetic and electric field decrease with r^{-2}, respectively r^{-1}. This constitutes the spatial separation of interference sources and victims, where feasible.

The plasma actuation system creates two different kinds of emissions. The first one is due to the high voltage and occurs at the same frequency as the driving frequency of the generator, i.e. in the kHz range. It would also occur if the plasma actuator would not be present, but replaced by an appropriate resistance. The second kind of disturbance is at higher frequencies in the MHz range due to the gas discharge at the actuator. Additionally, very severe disturbances occur when the actuator system is damaged and the spark gap of high voltage generator is triggered.

To analyze the occurring disturbances and investigate countermeasures a mock-up of the aircraft was used. Especially the influence of the length and position of the cables was analyzed, since the rest of the plasma actuation system is largely fixed. Different high voltage cables were tested, including solid, stranded, PVC- and PTFE-insulated wires. Although the emission did not change significantly, a stranded wire with a PTFE-insulation for high voltages was chosen to avoid flash-overs. It was also ensured that high voltage and grounded cable of the actuator are placed conjoined to minimize disturbances.

Several methods for electromagnetic shielding of the interference source and victim were considered. Using a Faraday shield for source or victim is prohibitive heavy for the use in-flight, and impossible for the plasma actuator. When using a low-pass RC-circuit in the high voltage cable of the plasma actuator, emissions can be reduced significantly, though with a loss in actuator efficiency, on the other hand such a low-pass filter can significantly reduce the noise on the victim side. Additionally twisted cables are used for the servo connections in the vicinity of the high voltage systems.

To achieve a spatial separation the servos are placed in the back of the tail and the wingtips, while the flight control and RC system, together with all sensors, are positioned in the front of the fuselage. The servo and high voltage cables in the wing are placed as far apart from each other as possible.

A safeguard against the severe disturbances due to the spark gap in case of failure of an actuator was installed in form of the servo switch for the high voltage generators. If the RC system is disturbed in such a way that the

servo motors begin to move from their set positions, also the switch moves from the active position. Thus the high voltage generators are deactivated and control of the aircraft can be regained.

5 Assessment as Flight Test Platform

5.1 Flight Characteristics

The flight characteristics of the aircraft depend on the airfoil used for the flow control section mounted. While for the default and separation ramp airfoils the plane features a relatively docile stall behavior, it is challenging to fly at low airspeeds with the NACA0015 airfoil. The landing distance depends on the wind conditions, but is in general just under 100 m, the take-off distance needed is considerably shorter.

The plane is moderately stable around the pitch and yaw axis, around the roll axis is marginally stable. This a measurable roll rate even at small asymmetric changes in lift due to flow control efforts.

5.2 Measured Data and Interpretation

The flight control system described in the previous section measures and records the quantities listed and characterized in Table 5.1. All data is supplemented with a timestamp, indicating the time of creation, for synchronization. To achieve a solution for the state of the aircraft, the IMU, GPS, barometer and magnetometer data is transformed and delivered as input for the flight controller and the post-flight analysis, as listed in Table 5.2. An extended Kalman filter, described by Savage [88, 89], is used to estimate the position and orientation of the aircraft. To avoid gimbal lock the orientation of the UAV is calculated as quaternion, consisting of a vector giving the rotation axis and a scalar giving the angle of rotation. The Euler rotations are given by

$$\begin{bmatrix} \Phi \\ \Theta \\ \Psi \end{bmatrix} = \begin{bmatrix} \text{atan2}\left(2\ \left(q_w\, q_x + q_y\, q_z\right),\ 1 - 2\ \left(q_x^2 + q_y^2\right)\right) \\ \arcsin\left(2\ \left(q_w\, q_y - q_x\, q_z\right)\right) \\ \text{atan2}\left(2\ \left(q_w\, q_z + q_x\, q_y\right),\ 1 - 2\ \left(q_y^2 + q_z^2\right)\right) \end{bmatrix}, \tag{5.1}$$

with atan2 being the two argument arctangent function, taking into account the signs of both arguments and thus returning the appropriate quadrant of the calculated angle.

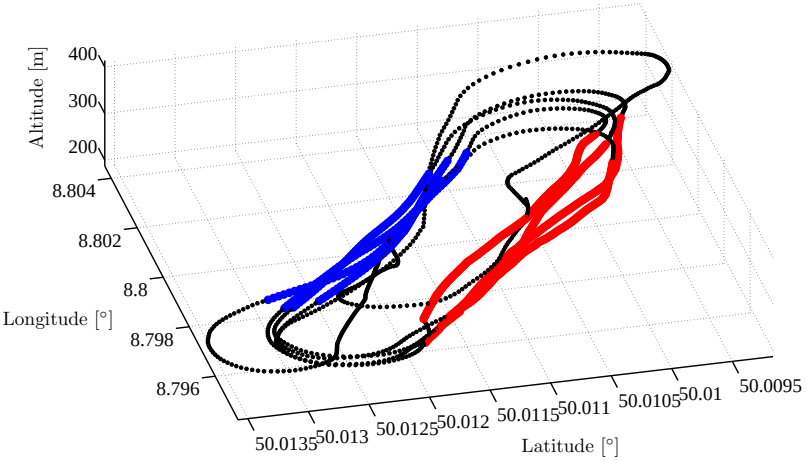

Figure 5.1: Typical flight path for an experiment with manual control. Shown are the positions from the GPS receiver, the flight segments with active actuation are marked in red, the reference segments in blue.

The data can be displayed during flight on the ground station as text, plot or 3D-visualization.

For the post-flight analysis the sensor data as well as the additional output data from the in-flight calculations is used. Alternatively the state can be calculated from the raw sensor data if the in-flight results are assumed to be erroneous.

In this case the objective of the flow control effort is to change the lift coefficient of the controlled section by influencing the separation. Two different methods to measure the lift are conceivable. In both cases only one section is actuated, resulting in an asymmetric lift distribution. Either the roll angle is fixed, i.e. zero, and an aileron deflection is used to counter a roll moment due to the plasma actuation, or the aileron deflection is set to zero and a roll movement is induced by the actuation. While the latter method is easy to execute and directly demonstrates the effect, it is hard to evaluate even at small roll angles since further effects occur, such as yaw coupling and roll damping. The countering of the roll moment with ailerons

Table 5.1: Characteristics of the measured data.

Symbol	Range	Sensitivity	Sample rate
$\check{p}$	$\pm 300°$ /s	3.33 mV/°/s	1000 Hz
$\check{q}$	$\pm 300°$ /s	3.33 mV/°/s	1000 Hz
$\check{r}$	$\pm 300°$ /s	3.33 mV/°/s	1000 Hz
$\dot{u}$	± 3.6 g	300 mV/g	1000 Hz
$\dot{v}$	± 3.6 g	300 mV/g	1000 Hz
$\dot{w}$	± 3.6 g	300 mV/g	1000 Hz
φ_{gs}		5 m SEP	4 Hz
λ_{gs}		5 m SEP	4 Hz
h_{gs}	$\leq 18,000$ m	5 m SEP	4 Hz
u_{gs}	$\lvert\overrightarrow{u}\rvert \leq 515$ m/s	0.1 m/s	4 Hz
v_{gs}	$\lvert\overrightarrow{u}\rvert \leq 515$ m/s	0.1 m/s	4 Hz
w_{gs}	$\lvert\overrightarrow{u}\rvert \leq 515$ m/s	0.1 m/s	4 Hz
ξ_{l}	± 1	± 1200 Counts	50 Hz
ξ_{r}	± 1	± 1200 Counts	50 Hz
η	± 1	± 1200 Counts	50 Hz
ζ	± 1	± 1200 Counts	50 Hz
D_{thr}	± 1	± 1200 Counts	50 Hz
S_{AP}	± 1	± 1200 Counts	50 Hz
S_{PA}	± 1	± 1200 Counts	50 Hz
B_x	± 1100 µT	31.24 Counts/µT	20 Hz
B_y	± 1100 µT	31.24 Counts/µT	20 Hz
B_z	± 1100 µT	31.24 Counts/µT	20 Hz
T	-40–$+125$ °C	10 mV/°C	2 Hz
p	400 hPa	450 mV/hPa	100 Hz
q	1250 Pa	3.2 mV/Pa	100 Hz
$P_{\mathrm{PA,l}}$	5 V	13107.2 Counts/mV	100 Hz
$P_{\mathrm{PA,r}}$	5 V	13107.2 Counts/mV	100 Hz

Table 5.2: Additional output data after transformation, describing position and flight state of the aircraft.

Name	Symbol	Remarks
Time received		
Sequence ID		
Time	t	All data timestamped
Reference pressure	p_{QNH}	
Barometric altitude	h_{b}	
Orientation quaternion	q_x, q_y, q_z, q_w	From EKF

on the other hand is easier to evaluate. Aileron deflection and roll rate, which should fluctuate around zero, can be calculated and compared for the baseline and actuated case. The resulting mean change in aileron deflection can be equated to a roll moment, as shown in Figure 5.2 from wind tunnel measurements. Furthermore the roll moment from the actuation can also be expressed as a change in lift for the actuated section

$$\Delta C_{L,\mathrm{fcs}} = \Delta C_{\check{L}} \frac{b\,S}{2\,y_{\mathrm{fcs}}\,S_{\mathrm{fcs}}}, \tag{5.2}$$

which is a practical indicator for the flow control effect. The assumption of a constant change in lift over the actuated section was made, with $y_{\mathrm{fcs}} = 0.55$ m being the moments lever arm at the center of the section. The data presented in Figure 5.3 shows this correlation for wind tunnel experiments, described in detail in Section 6.4.1.

5.3 Evaluation of Electromagnetic Compatibility

5.3.1 General

Different actuator configurations were tested and the influence on the systems of the UAV measured. As already discussed in Section 4.3.5, the most severe disturbances are to be expected at the servo cables due to capacitive coupling. It was found, that primarily the cables to the servo motors in the wings section and, to a minor degree, to the propulsion motors are affected. In contrast the cables to the tail section are only for a short distance in the vicinity of the high voltage systems and thus less disturbed.

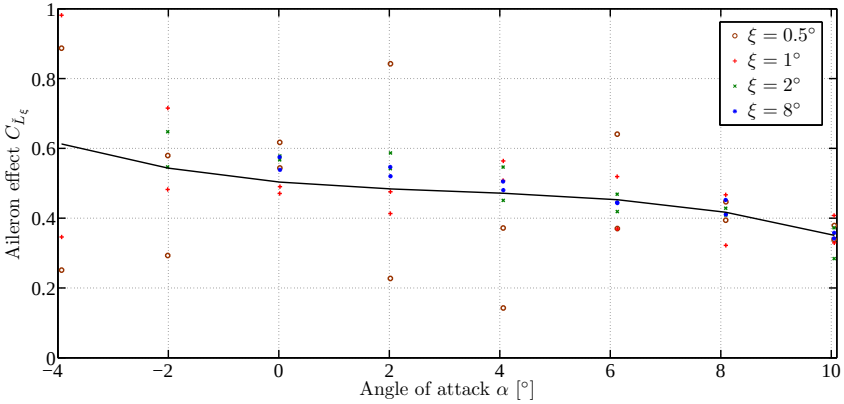

Figure 5.2: Roll moment derivative due to a deflection of the ailerons in dependency of the angle of attack, respectively the airspeed, which was adjusted accordingly. Both ailerons were deflected antimetric, the derivative is based on the mean absolute value. The measurements were conducted in the NWk 1 wind tunnel of the TU Darmstadt, the setup described in Section 6.4.1 was used.

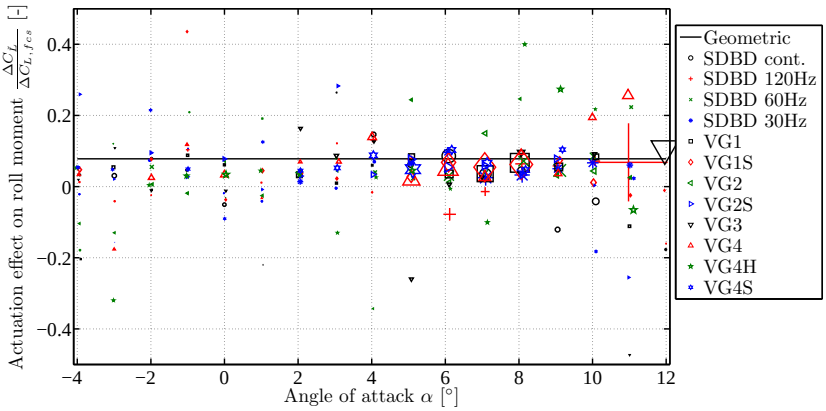

Figure 5.3: Roll moment per change in section lift coefficient due to actuation against angle of attack, respectively airspeed, which was adjusted accordingly. Displayed are the geometric solution from Equation 5.2 and data from wind tunnel experiments. The experimental data is rather scattered, due to noise in the measurements, especially at small flow control effects. The size of the markers was scaled according to the amplitude of the effect measured.

The disturbances in the signal for the different servo cables are shown in Figure 5.4. Although noise is apparent, high grade servo electronics are still able to clearly discern the signal. Other, more susceptible servo motors showed jitter and were unresponsive to input commands. Also proven unaffected was the propulsion system, the brushless motor controllers chosen showed no interference, the measured rotational speed remained constant.

It was determined further that a radio control operating in the 2.4 GHz band is not measurably disturbed, even with a weak radio signal. In contrast, the 35 MHz band, which was formerly used, is heavily disturbed and thus not usable.

The flight control system including the miniature PC and the receiver were found to be unaffected, as expected. Since they work digitally, the disturbances do not compromise the signal as long as below a certain threshold between high and low voltage. Nonetheless, even though the data processing is unaffected, the measurement data by the sensors can be distorted, especially the magnet field sensors, as discussed below.

5.3.2 Sensors

Due to the emitted electromagnetic disturbances the sensors can be distorted, resulting in an increase in noise or deviation of the mean value. Noise is less critical, since for most sensors the sampling rate is sufficient to filter the data before processing. A deviation of the mean value on the other hand can, for example, result in an erroneous state space estimation, influencing the autonomous guidance and compromising the post-flight analysis of the experiments. Especially important under both aspects is the inertial measurement unit, since it is used to obtain the transient change of orientation and direction of flight of the UAV. Less critical regarding noise are the GPS receiver, barometer and the magnetic field sensor, used to avoid drift for the long-term solution. Nonetheless, a deviated mean value can result in an over time deviated solution. Furthermore the plasma power measurement and the airspeed sensor are needed for the evaluation of the experiments.

The results of a comparison for a motionless aircraft in arbitrary orientation on the ground are shown in Figures 5.5 to 5.8. It can be seen, that the noise measured at the IMU is not significantly higher than for the unactuated case. Also precision and trueness of the measurements both show no considerable deviation, which is also true for the barometer. The GPS sensor was not measurably influenced at all. However, the magnetic field sensor indicates a significant altered mean value, especially in the di-

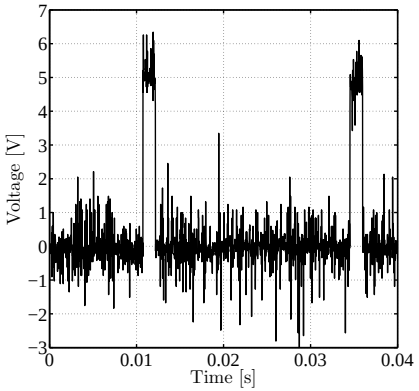

(a) Aileron servo signal at plasma actuator side.

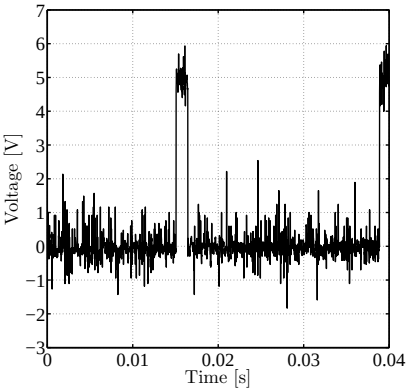

(b) Aileron servo signal at opposite side.

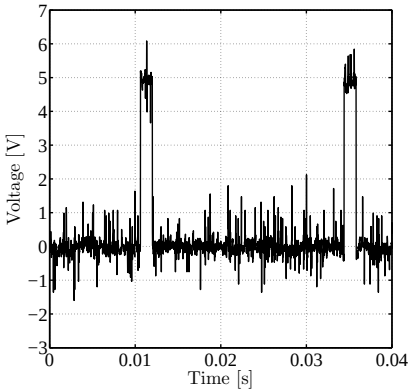

(c) Tail servo signal.

Figure 5.4: PWM servo signal with superimposed electromagnetic disturbances caused by plasma actuation system. Two actuators were placed on the same wing section. Depicted are the disturbances at the aileron servos on the actuator (a), and on the opposite (b) side, and at a tail servo (c). Although disturbed, the pulse of the signal can clearly be distinguished and interpreted by the servo electronics.

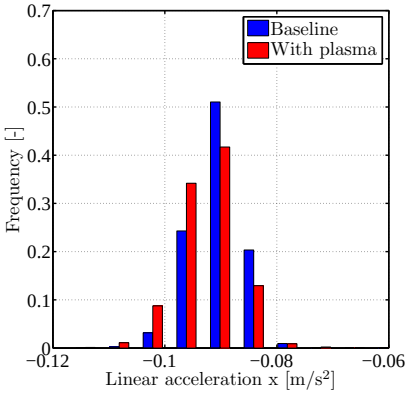

(a) x-axis.

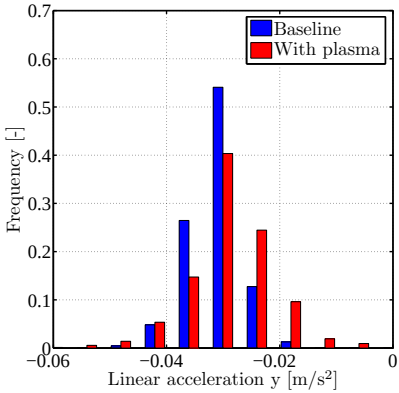

(b) y-axis.

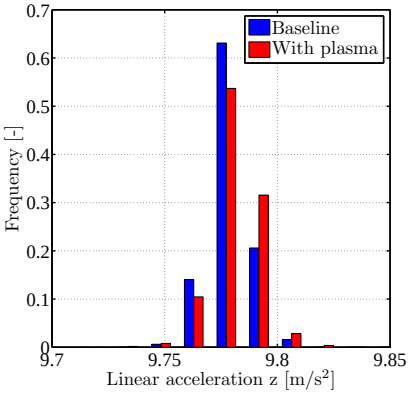

(c) z-axis.

Figure 5.5: Histogram of accelerometer data with and without plasma actuation.

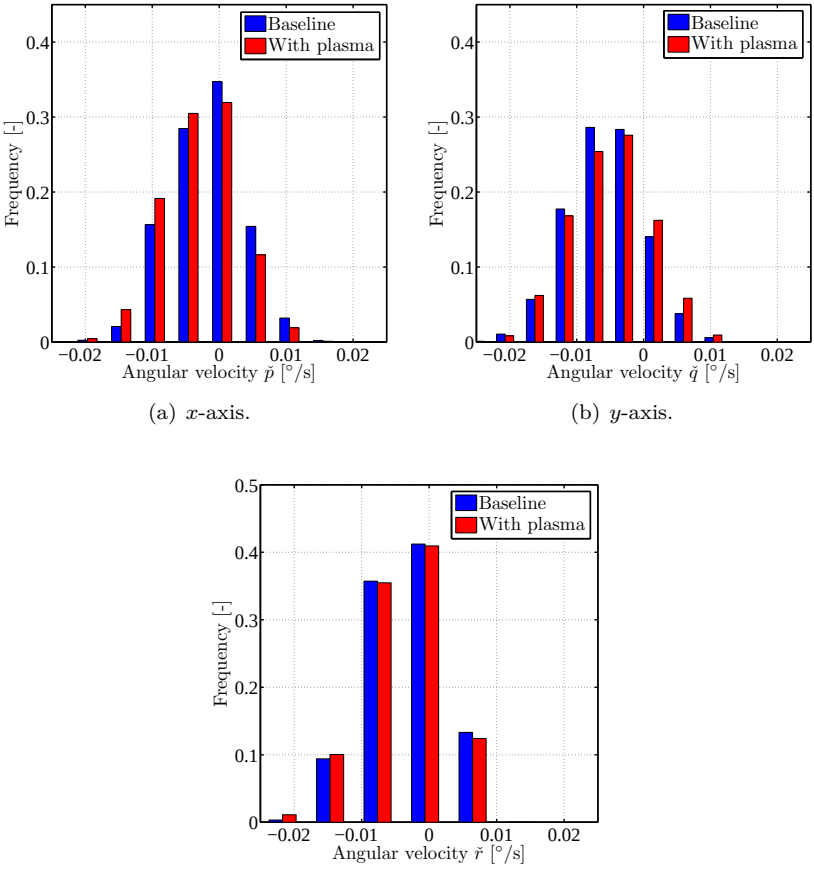

(a) x-axis.

(b) y-axis.

(c) z-axis.

Figure 5.6: Histogram of angular velocity data with and without plasma actuation.

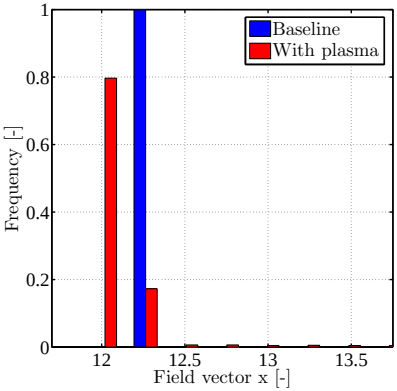

(a) x-axis.

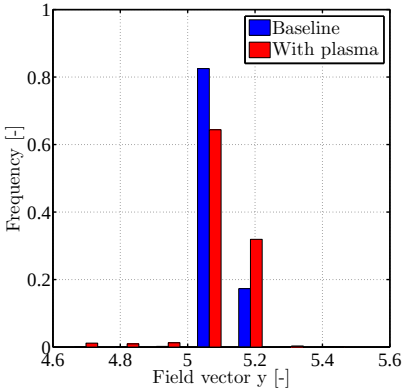

(b) y-axis.

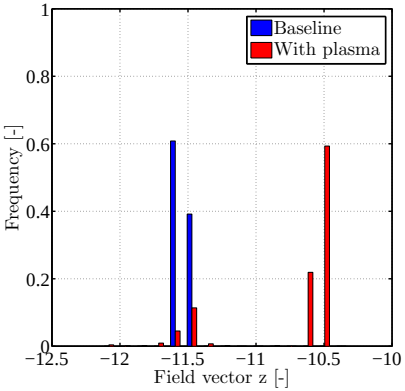

(c) z-axis.

Figure 5.7: Histogram of magnetometer data with and without plasma actuation.

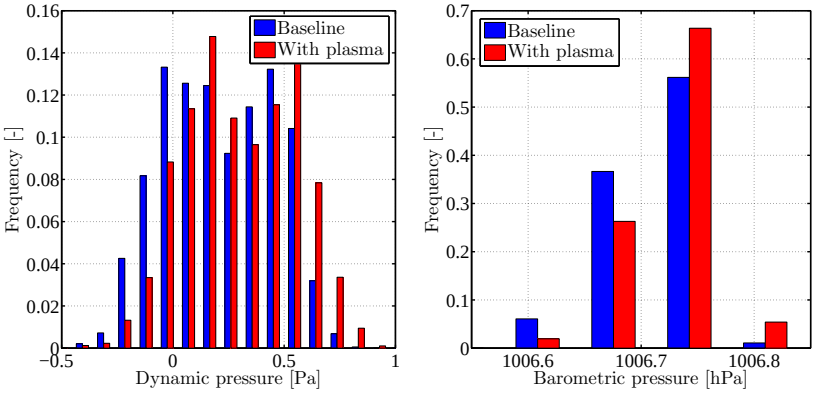

(a) Airspeed.

(b) Altimeter.

Figure 5.8: Histogram of airspeed and barometric pressure sensor data with and without plasma actuation.

rection of the z-axis. This is explained by the presence of a magnetic field emitted from the plasma actuation system, which is superimposed to the earth's magnetic field and is oriented approximately in the z-direction at the position of the sensor in the front of the airplane. Therefore an error in the state estimation of the aircraft results, increasing with the plasma actuation time. This is not critical for short actuation times, nonetheless it can be met by decreasing the influence of the magnetometer on the state estimation during plasma actuation for in-flight autonomous control and post-flight analysis.

Furthermore, the output of the plasma actuator power measurement shows an increasing variance at higher voltages, due to both, capacitive and conductive, coupling. This effect was minimized by installing it in a screened housing and low-pass filtering the input signals, as described in Section 4.3.4.2. Since the actuator power is relatively steady, the output signal can furthermore be averaged in post-processing to achieve an adequately accurate value.

6 Flow Control Experiments

6.1 Analyzed Configurations

6.1.1 Overview

Several new actuators and flow control concepts for separation delay were investigated in the PLASMAERO project, described in detail in the ERCOFTAC Bulletin special theme on plasma aerodynamics [10, 17, 17, 37, 71, 80, 105]. Only a few were considered adequate for the use on the UAV, others were discarded for various reasons. Plasma spark jet actuators are too large to be installed in the wings and need a stronger power supply, nanopulse and fast-rise-pulsed actuators are designed for flow control at higher Mach numbers. The actuator configurations expected to produce a flow control effect at the in-flight flow conditions, and suited for the installation on the UAV, are described in principle in Section 2.4.6.

In this study a MDBD actuator developed at the Instytut Maszyn Przeplywowych, and a VGDBD actuator developed at the University of Nottingham, thus referred to as IMP and UNOTT actuators in the following, were investigated. These, as well as the generic NACA0015 airfoil, chosen for trailing-edge separation control in wind tunnel experiments by the PLASMAERO partners, are described below. Both actuators were tested on this airfoil, since they are designed for and already tested on it. No other actuator configurations were applied to it, due to its problematic characteristics during flight.

In the preliminary flow control experiments, described in Section 3.3, conducted prior to the design of the UAV, the separation ramp profiles showed the most promising results. Therefore several separation ramp airfoils were designed using the inverse design routine of XFOIL. In contrast to the preliminary investigations the separation ramps are not manufactured by applying them onto the wing but by inserting them into the mould. Therefore only subtractions from the original airfoil are possible, additionally structural constraints apply due to the placement of the spar and torsion bolts. Separation ramps at different positions, with different curvature radii and angles were investigated. Since XFOIL can neither estimate a separation

Table 6.1: Airfoil/actuator configurations tested in the wind tunnel experiments.

	SDBD	MDBD	VGDBD
NACA0015		IMP	UNOTT
MOD7	SDBD		VG1, VG1S, VG2, VG2S, VG3, VG4, VG4H, VG4S
MOD11	SDBD		VG5
MOD13	SDBD		VG6

Table 6.2: Airfoil/actuator configurations tested in the flight experiments.

	SDBD	MDBD	VGDBD
NACA0015		IMP	
MOD7			VG1S, VG4S
MOD11			
MOD13			

accurately nor simulate the effect of a plasma actuator, several different airfoils were built for the wind tunnel experiments, and, if proven successful, subsequent flight testing. On each of the two units of the separation ramp airfoils a SDBD and a VGDBD were applied prior to the experiments. The separation lines were previously calculated using XFoil and the actuators positioned accordingly, as listed in Tables 6.3 and 6.4. Since both, the MOD11 and the MOD13 airfoil, exhibit improper characteristics for separation control, no further experiments were performed. Instead additional actuator configurations were tested using the MOD7 airfoil.

The configurations which were most successful in the wind tunnel experiments were chosen for the flight tests. In particular these are the NACA0015 airfoil with the IMP actuator and the MOD7 separation ramp airfoil with the VG1S and VG4S actuators, showing a significant change in lift for a relatively wide range of angles of attack. The VG4S actuator is particular because of its negative change in lift for a very wide range of angles at a comparably small magnitude in the wind tunnel experiments.

6.1.2 NACA 0015 Airfoil

The NACA0015 is an early generic airfoil, developed as part of the NACA 4-digit series in the 1930s [56], which has found wide use in academics. It

Table 6.3: Parameters for the SDBD actuators used.

Airfoil	Position x/c	Mode	V_{pl} [kV]	f_{pl} [kHz]
MOD7	0.44	Continuous	12.5	9.9
		Pulsed 120 Hz, 50%DC	13.8	9.5
		Pulsed 60 Hz, 50%DC	13.8	9.5
		Pulsed 30 Hz, 50%DC	13.8	9.5
MOD11	0.44	Continuous	11.3	9
		Pulsed 120 Hz, 50%DC	13.8	9
		Pulsed 60 Hz, 50%DC	13.8	9
		Pulsed 30 Hz, 50%DC	13.8	9
MOD13	0.5	Continuous	11.5	8.3
		Pulsed 120 Hz, 50%DC	13.3	8.3
		Pulsed 60 Hz, 50%DC	13.3	8.3
		Pulsed 30 Hz, 50%DC	13.3	8.3

Table 6.4: Parameters for the MDBD and VGDBD actuators used.

Airfoil	Name	Position x/c	Electrodes	V_{pl} [kV]	f_{pl} [kHz]
NACA 0015	IMP	0.4–0.65	3 (+2)	11/11	8/8
	UNOTT	0.3–0.63	8	8.8/9.4	6.8/6.8
MOD7	VG1	0.1–0.4	8	9.5/9.5	6.8/6.8
	VG1S	0.25–0.4	8	10.7/10.7	8.2/8.2
	VG2	0.17–0.47	8	10/10	6.8/6.8
	VG2S	0.32–0.47	8	11/11	7.5/7.5
	VG3	0.25–0.4	12	10.8/10	7.1/7.2
	VG4	0–0.3	17	10/9	5.2/5.6
	VG4H	0–0.3	8	10.5/10.5	8/8
	VG4S	0–0.15	17	10.5/10.5	8/8
MOD11	VG5	0.27–0.39	22	8.1	7.5
MOD13	VG6	0.2–0.5	8	9.6/9.6	6.5/6.5

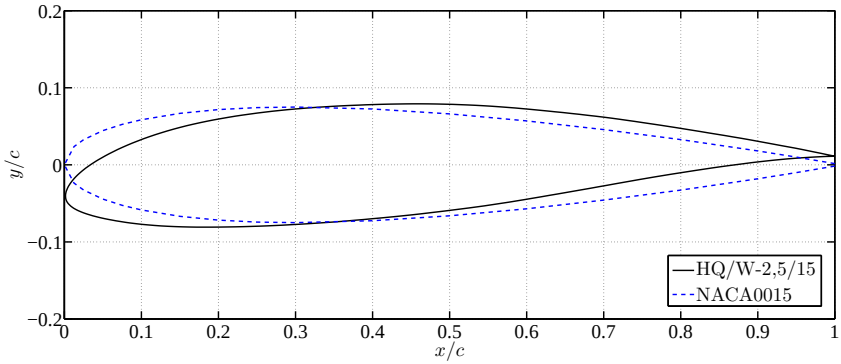

Figure 6.1: Cross section of the NACA0015 airfoil used for the experiments, with the standard wing airfoil at a negative incidence of 3° for reference.

is symmetric and has a thickness of $t/c = 15\%$, in the relevant Reynolds number range it exhibits a trailing-edge separation, which leads to a relatively docile stall behavior. Also beneficial for flight application is its relatively insensitive to surface roughness. However, the maximum attainable lift coefficient is comparably small and the drag is high, especially at low Reynolds numbers. It is therefore rather unsuitable for use on a wing, but was nonetheless used in this case because of the widespread utilization in academics and the availability of reference and comparative data.

To achieve the same lift coefficient as the adjacent sections the NACA0015 flow control sections have an additional incidence angle of 3° to the wing, respectively an angle of 8° to the fuselage. This results in an earlier stall than at the other sections, and corresponding challenging flight characteristics at lower speeds, most critical during during take-off and landing.

6.1.2.1 MDBD Actuator

The IMP MDBD actuator configuration used on the airplane consists of two actuators, each covering half of the span of the wing section. This configuration was chosen due to the restricted power output of the Minipuls 0.1 high voltage supply, each actuator half is driven by one of the Minipuls devices on board of the UAV.

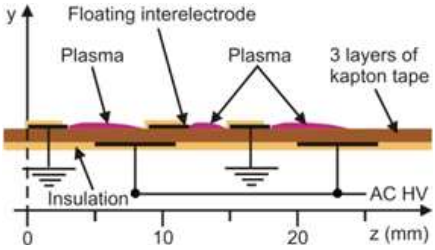

Figure 6.2: Sketch of the IMP MDBD actuator configuration. (From [71])

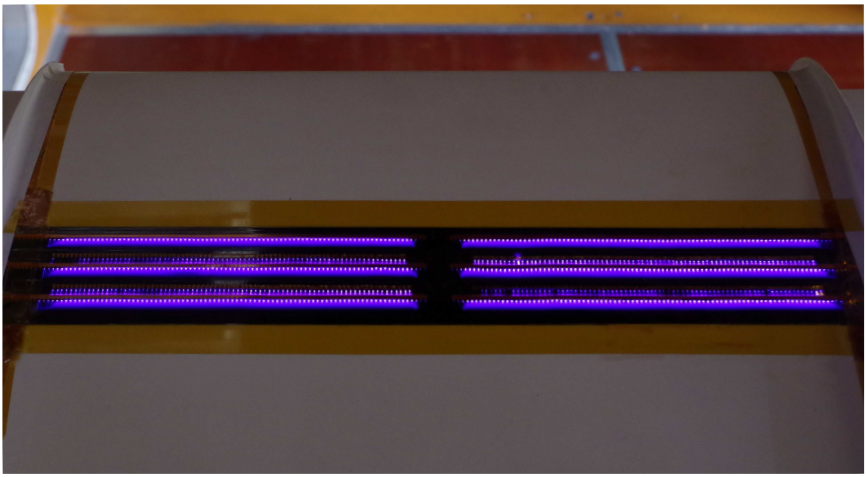

Figure 6.3: IMP MDBD actuator configuration operated by two Minipuls 0.1 high voltage generators.

The actuator array features several grounded electrodes on top of the dielectric, with floating interelectrodes in-between. Details of the actuator and the tests performed at IMP can be found in [71], the working principle is described in Section 2.4.6.2.

The actuator was installed on the flow control section inside a recess of 1 mm depth and 50 mm length, beginning at 40% chord, and was driven by two Minipuls 0.1 power supplies. Various tests were performed to find the maximum power attainable since the generators are less powerful than the one used during the IMP wind tunnel experiments. The specifications of this actuator require 100% duty cycle, also meaning that burst frequency was not a factor. Testing began at a low input voltage of 22 V and was carried forth until reaching 32 V, any input voltage higher than 26.5 V was found sufficient and resulted in both sides of the actuator operating at 11 kV and 8 kHz.

6.1.2.2 VGDBD Actuator

At the University of Nottingham a counter-rotating DBD vortex generator for the use on the UAV was developed, shown in Figure 6.4. Due to the actuation streamwise vortices are generated, entraining the high speed flow from outside into the boundary layer and thereby canceling separation. Details about the UNOTT wind tunnel testing can be found in [105].

The actuator consists of 8 streamwise oriented upper electrodes, which are 45 mm apart from each other in spanwise direction. The dielectric material used is 0.25 mm thick Cirlex, covering the grounded electrode, which extends across the whole span of the wing section. The streamwise length of the actuator is 100 mm , extending from 30 to 63% of the chord. The UNOTT actuator was driven with both Minipuls power supplies at a voltage of 8.8 kV on the right side, respectively 9.4 kV on the left, and a plasma frequency of 6.8 kHz for both.

6.1.3 MOD7 Separation Ramp Airfoil

The MOD7 airfoil has a comparably severe separation ramp with a small curvature radius and therefore a drastic change in pressure coefficient. The ramp begins at 44% x/c, the point of inflexion is at 47% x/c. The pressure coefficient decreases rapidly at the beginning of the ramp, then rises steeply behind. The flow either overcomes this pressure rise, or separates from the surface, depending on the energy in the boundary layer. Flow control is aimed at increasing the energy near the separation point, and thereby

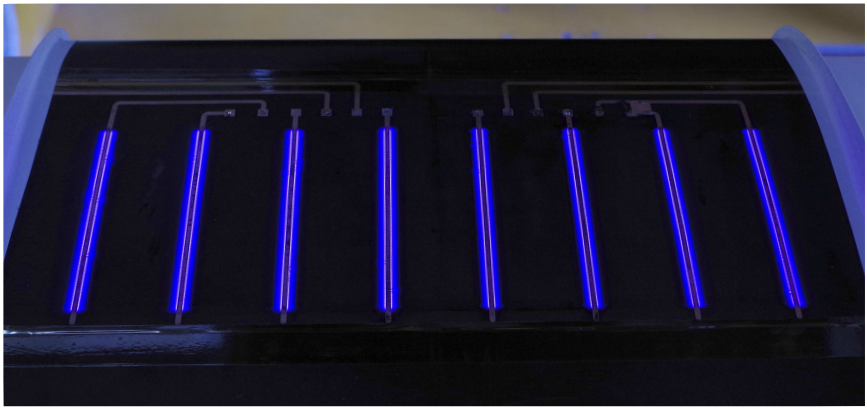

Figure 6.4: UNOTT VGDBD actuator configuration on NACA0015 airfoil during wind tunnel tests.

reducing the severity of the separation. For a significant change in lift it is desirable to have an open separation without flow control, and accomplish a reattachment of the flow in actuated mode.

6.1.3.1 SDBD Actuator

The SDBD actuators used for the experiments consist of a 16 mm wide copper tape lower electrode, a 0.35 mm thick dielectric consisting of several layers of Kapton tape and a 3 mm wide upper electrode, as depicted in Figure 2.9. To achieve a homogenous plasma distribution along the span a small overlap between the electrodes was applied. They cover almost the entire flow control section in spanwise direction, with approximately 20 mm space to the wing fences.

The actuator on the MOD7 airfoil was placed in front of the calculated separation line, at 44% x/c The reference for this value is the end of the upper electrode, respectively front of the lower electrode, the plasma starts at this point and extends in downstream direction.

All SDBD actuators were driven by one Minipuls 0.1 device with the parameters given in Table 6.3. The plasma frequencies were adjusted to the best resonance, the voltages according to the limitations of the Minipuls 0.1 generator, for pulsed actuation a higher voltage was adjusted to achieve a similar mean power output.

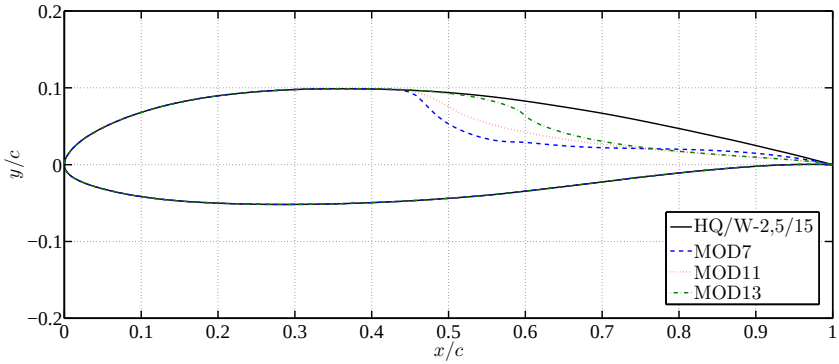

Figure 6.5: Separation ramp airfoils used for the experiments.

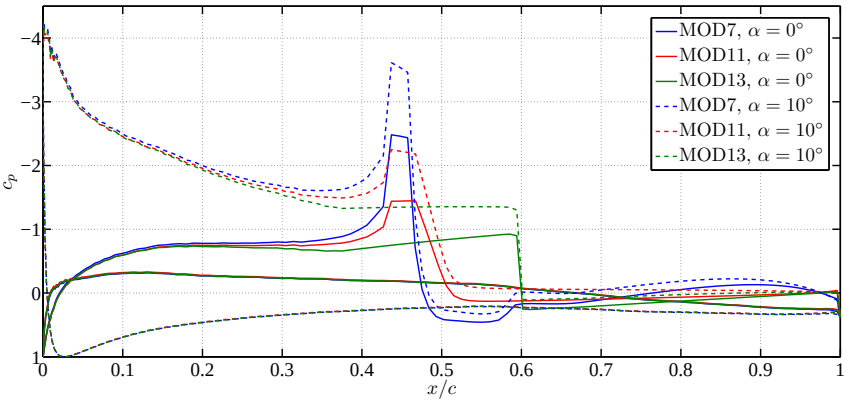

Figure 6.6: Inviscid pressure coefficient of the separation ramp airfoils.

6.1.3.2 VGDBD Actuators

In contrast to the UNOTT actuator on the NACA0015 airfoil, all other VGDBD actuators are made of copper tape lower electrodes, 0.35 mm thick Kapton tape dielectric, and copper tape upper electrodes with a slight overlap of the electrodes.

The VG1 actuator is very similar in geometry to the UNOTT actuator. It also features 8 upper electrodes, 4 driven by each Minipuls. They are spaced 45 mm in spanwise direction and have a width of 3 mm and a length of 90 mm. This equals a range of 10 to 40% x/c on the MOD7 airfoil, with the separation ramp beginning at 44% x/c shortly behind. A voltage of 9.5 kV at a plasma frequency of 6.8 kHz was adjusted for both parts of the actuator.

The VG1S actuator is the shorter version of the VG1, the upper electrodes were shortened to a length of 45 mm. Therefore the beginning of the actuated region is at 25% x/c, while the end remained at 40% x/c in front of the separation. Due to the shorter combined length of the actuator a higher voltage of 10.7 kV at a higher frequency of 8.2 kHz was reached, leading to a more powerful wall-jet, although over a shorter streamwise length.

The VG2 actuator has the same geometry as the VG1, but is mounted in a further downstream position, the actuated region begins at 17% x/c and ends at the inflexion point of the separation ramp at 47% x/c. Due to production impreciseness the maximum adjustable voltage of 10 kV at 6.8 kHz differs slightly from the VG1 actuator.

The VG2S is the shorter version of the VG2, with a streamwise length of the electrodes of 45 mm, from 32 to 47% x/c. The voltage was adjusted to 11 kV at a plasma frequency of 7.5 kHz, for both sides.

The VG3 actuator is placed at the same position as the VG1S, beginning at 25% x/c and ending at 40% x/c. Unlike the previously described actuators it has 12 upper electrodes, with a length of 45 mm. The electrodes are 5 mm in width and are spaced at 30 mm in spanwise direction. The voltage was adjusted to 10.8 kV at a plasma frequency of 7.1 kHz on the right actuator side and 10 kV at 7.2 kHz on the left.

The VG4 actuator is placed further upstream, beginning at the leading edge. It effectively has 17 upper electrodes, with the outermost electrodes only creating a plasma on the inner side. The electrodes are 90 mm long in streamwise direction, extending to 30% x/c. Due to the long combined length of the actuator voltages of only 10 kV at a plasma frequency of 5.2 kHz on the right actuator half, and 9 kV at 5.6 kHz on the left were

reached.

For the VG4H actuator half of the electrodes of the VG4 actuator described above were removed, a voltage of 10.5 kV at a plasma frequency of 8 kHz was adjusted for both sides.

The VG4S actuator has shorter upper electrodes than the VG4 actuator with only 45 mm length, extending from the leading edge to 15% x/c. The voltage was adjusted to 10.5 kV at a plasma frequency of 8 kHz.

6.1.4 MOD11 Separation Ramp Airfoil

The MOD11 airfoil has a more moderate separation ramp than the previously described MOD7. The ramp begins at the same position of 44% x/c, the point of inflexion is at 50% x/c. The attained pressure coefficients are moderate and the resulting separation thus less severe and more sensitive to flow control efforts.

6.1.4.1 SDBD Actuator

The same SDBD actuator configuration as already described in the previous section was also used on the MOD11. The actuator was placed in front of the separation at 44% x/c.

6.1.4.2 VGDBD Actuator

The VG5 actuator spans only 45% of the spanwise length of the flow control section. It is 36 mm in streamwise length, begins at 27% x/c and ends at 39% x/c. The 22 electrodes are spaced closer than for the other VGDBD actuators at only 8 mm apart, and have a width of 2 mm. The voltage adjusted was 8.1 kV at a plasma frequency of 7.5 kHz.

6.1.5 MOD13 Separation Ramp Airfoil

The MOD13 airfoil has a ramp which creates a slightly decreasing to constant pressure coefficient in front of it, depending on the angle of attack. The ramp has an decreasing radius and begins at 45% x/c, the point of inflexion is at 60% x/c. The rise in pressure is considerably smaller than for the other two airfoils.

6.1.5.1 SDBD Actuator

Again the same SDBD actuator configuration as already described was used on this airfoil, the actuator was placed in front of the separation at $50\%\, x/c$, which is further downstream than for the other airfoils, where separation occurs earlier.

6.1.5.2 VGDBD Actuator

The VG6 actuator has the same geometry as the previously described VG1 actuator on the MOD7 airfoil, it begins at $20\%\, x/c$ and ends at the onset of the separation ramp at $50\%\, x/c$. The voltage was adjusted to 9.6 kV at a plasma frequency of 6.5 kHz.

6.2 Wind Tunnel Set-Up

The experiments were conducted in the Göttinger type Niedergeschwindigkeitswindkanal NWk1 wind tunnel facility at the TU Darmstadt. The test section measures 2.9×2.2 m^2 and is 4.8 m long. Velocities of up to 68 m/s can be adjusted, at a turbulence intensity of approximately 0.2%.

The aircraft was mounted on two posts, as shown in Figure 6.7. The main post was fixed to the mounting point of the main gear, to this avail the complete gear was removed. Besides the gear also the propellers were removed, since they could not be operated in the wind tunnel. The main post absorbs forces in all directions and allows rotations around the pitch axis, while fixing the aircraft in roll and yaw. The pitch angle was adjusted by a vertically displaceable post mounted at the tail section. A high-accuracy inclinometer was mounted inside the payload section of the fuselage and connected to the wind tunnel measurement system to control the angle. Both posts are based on the external wind tunnel scale below the test section. The scale is capable of measuring forces and moments in all directions, as defined in Table 6.5. Although the aircraft has a span of 82% of the wind tunnel width, the produced forces and moments are at the lower limit of measuring range of the scale, since usually higher Reynolds numbers are of interest.

For the first experiments the standard profiles were used on the flow control sections, the angle of attack was advanced in 1° steps from the smallest adjustable angle of $-4°$ to the stall angle of 12°. The lift was adjusted to 100 N to reproduce the flight case, and the according velocities, respectively dynamic pressures, recorded, as shown in Figure 6.8. These

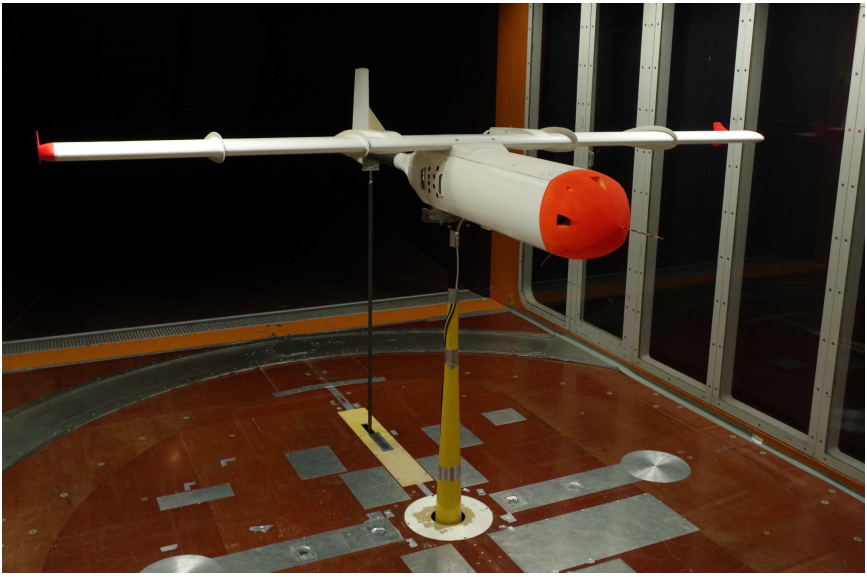

Figure 6.7: UAV mounted in the NWk1 wind tunnel at the TU Darmstadt. The main post fixes the aircraft in the roll and yaw axis, while rotations around the pitch axis are adjusted by the vertically displaceable tail post.

Table 6.5: Parameters of the external wind tunnel scale in the NWk1 wind tunnel facility.

Component	Limitations	Trueness	Precision
Drag	±1500 N	0.02% FS ≡ 0.6 N	0.02% FS ≡ 0.6 N
Side force	±2000 N	0.025% FS ≡ 1 N	0.02% FS ≡ 0.8 N
Lift	−2500– +6000 N	0.025–0.04% FS ≡ 2.125–3.4 N	0.025–0.04% FS ≡ 2.125–3.4 N
Roll moment	±1000 Nm	0.09–0.095% FS ≡ 1.8–1.9 Nm	0.02% FS ≡ 0.4 Nm
Pitching moment	±1300 Nm	0.066–0.08% FS ≡ 1.716–2.08 Nm	0.015% FS ≡ 0.39 Nm
Yaw moment	±1200 Nm	0.028% FS ≡ 0.672 Nm	0.02% FS ≡ 0.48 Nm

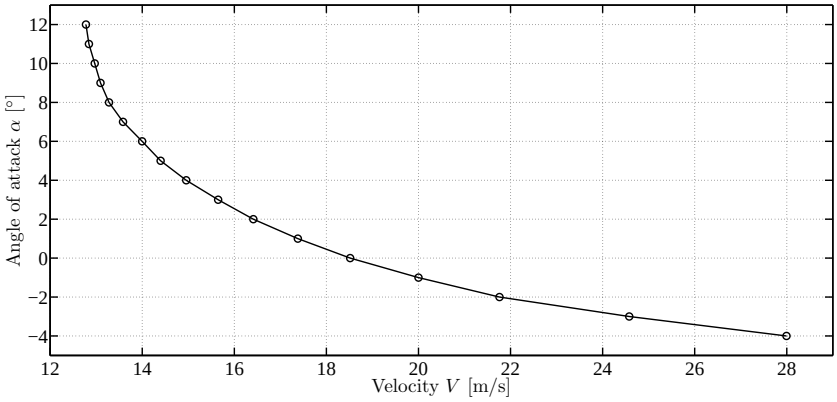

Figure 6.8: Velocity against angle of attack of the UAV in wind tunnel for 100 N lift in baseline configuration. The determined combinations were used for the further wind tunnel experiments.

combinations were used for the further flow control experiments, although other flow control sections are used. It was assumed that the error compared to the free-flight velocities, due to the slightly changed lift coefficients of the sections, is comparably small, and that the flow topology and the control effect are consistent.

6.3 Free-Flight Set-Up

The experiments can only be conducted under favorable weather conditions. The visibility has to be high enough to clearly see the UAV during the entire flight, wind and gusts should be weak for the experiments, although the plane is able to fly and was also tested at higher wind speeds. Additionally, the wind direction has to be suitable for the landing approach at the relatively small model airfield. Even when the weather conditions allow experiments, the flow control effect of the plasma actuator is highly dependent on the atmospheric conditions, as discussed in Section 2.4.3. The relevant atmospheric parameters for the individual flight experiments are listed in Table 6.6.

The first flights were made with different configurations to test all systems and ensure a safe flight with plasma actuation. During these flights the flight control unit was operated as data recording and monitoring device, collecting all available sensor data and remote-control signals. Prior to the flow control experiments the electrical parameters of the actuators were adjusted on the ground. During the experiments straight horizontal legs were flown in actuated and unactuated mode. In the post-flight analysis the roll rate and the aileron deflection were compared for both cases to detect the influence of the actuation.

6.4 Discussion of Results

6.4.1 Wind Tunnel Results

6.4.1.1 NACA0015 Airfoil

The NACA0015 airfoil has a trailing edge separation which moves forward with increasing angle of attack. The ability of the IMP MDBD and the UNOTT VGDBD actuators to delay this separation were investigated. While the UNOTT actuator shows no significant increase in lift coefficient, with

Table 6.6: Conducted flights with the PLASMAERO UAV and ambient conditions. Specified are the temperature T, relative humidity rh, reference pressure p_{QNH} and ground wind speed V_{w}, as measured by the Deutscher Wetterdienst.

Flight	Configuration	T [°C]	rh [%]	p_{QNH} [hPa]	V_{w} [m/s]	Remarks
1	Clean	14	79	1017	2	Maiden flight, no FCS and HV generators on board
2	MOD7	8	68	1003	8	HV generator, FCS data acquisition, EMC tests
3	NACA0015 IMP	5	87	1021	2	Data storage error
-	NACA0015 IMP	-	-	-	-	FCS error, flight aborted
4	NACA0015 IMP	4	81	1001	7	High wind, relatively turbulent, low temperature
-	MOD7 VG4S	-	-	-	-	Missing aileron connection, flight aborted
5	MOD7 VG4S	5	84	1020	2	Slight condensation on wing, low temperature
6	MOD7 VG1S	13	90	1023	2	
7	MOD7 VG1S	8	93	1015	1.5	Slight condensation on wing, low temperature

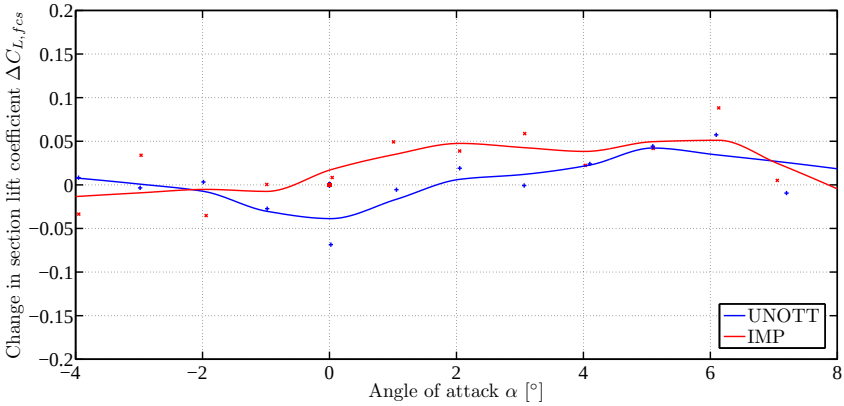

Figure 6.9: Change in section lift coefficient over angle of attack for UNOTT and IMP actuators on NACA0015 airfoil.

the IMP actuator a slight increase of approximately $\Delta C_{L,\text{fcs}} = 0.05$ is observed in the range from 0 to 6° angle of attack.

6.4.1.2 Separation Ramp Airfoil MOD7

The separation ramp airfoil shows a strong separation behind the ramp. Up to approximately 3° angle of attack the flow is able to reattach before the trailing edge, at higher angles the separation is open in the unactuated case.

The SDBD actuator shows an effect when operated in pulsed mode. As depicted in Figure 6.10, especially at burst frequencies of 30 and 60 Hz an increase in lift coefficient is observable in the range from 5 to 11° angle of attack. While the maximum lift change is higher for the 30 Hz case, the effect is present at a broader range of angles for 60 Hz.

The results from the VGDBD actuators are particularly interesting, since both lift increase and decrease were observed. While the VG1 and the shorter VG1S increase the lift by up to $\Delta C_{L,\text{fcs}} = 0.1$ over a range of angles of attack from 5° to 10°, the effect is significantly smaller for the VG2 and VG2S actuators mounted further downstream. It can be assumed, that for the latter configurations the vortices are not yet fully developed and thus weaker. The VG3 actuator, although at the same position as the VG1S actuator, but with a higher number of electrodes, shows no

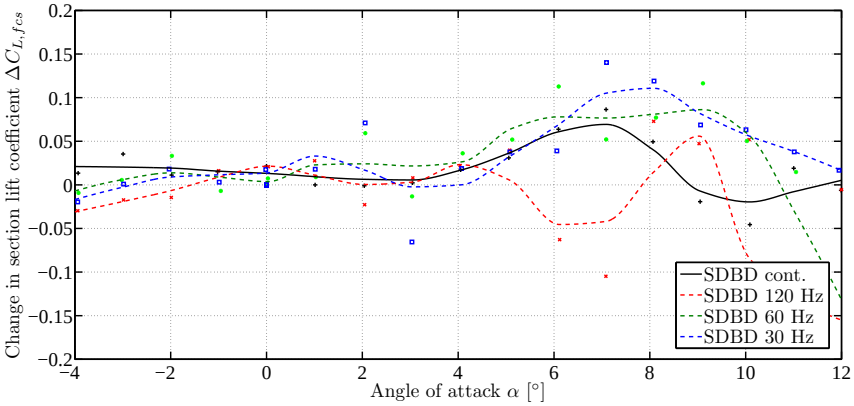

Figure 6.10: Change in section lift coefficient over angle of attack for SDBD actuator on MOD7 airfoil.

significant influence on the flow. The VG4 and VG4S actuators, placed at the leading edge, decrease the lift coefficient. While the change in lift is up to $\Delta C_{L,\text{fcs}} = -0.1$ for the VG4 actuator, its effect is limited to 4° to 7° angle of attack. The VG4S actuator with shorter electrodes induces a smaller change in lift of up to -0.05, albeit over a range from 2° to 9° angle of attack. The VG4H actuator again shows no significant influence on the flow. It is assumed that the dissimilar results originate from effects due the not yet fully developed boundary layer at the leading edge, as well as vortex interactions.

6.4.1.3 Separation Ramp Airfoil MOD11

The flow over the MOD11 airfoil does not exhibit a strong separation at low angles of attack. Although a separation bubble may be present, the flow reattaches before reaching the trailing edge, thus no flow control effect was measured in this regime. At higher angles a massive separation occurs, no flow control configuration was able to manipulate it significantly. Only the two previously prepared configurations were tested, no further efforts were made after evaluation of the baseline flow.

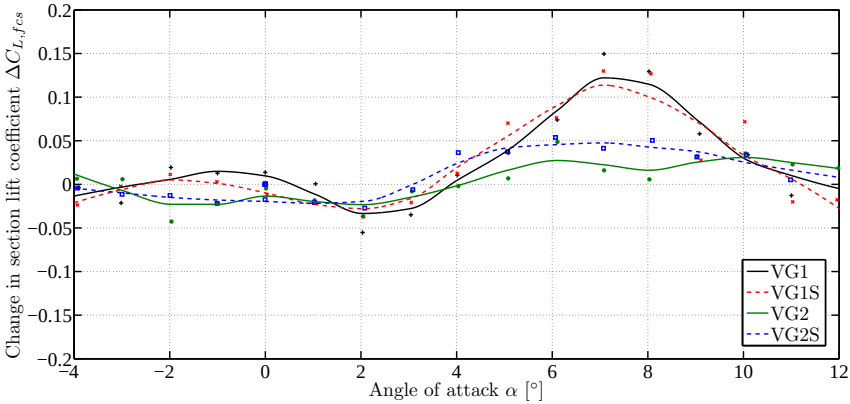

Figure 6.11: Change in section lift coefficient over angle of attack for VG1, VG1S, VG2, VG2S actuators on MOD7 airfoil.

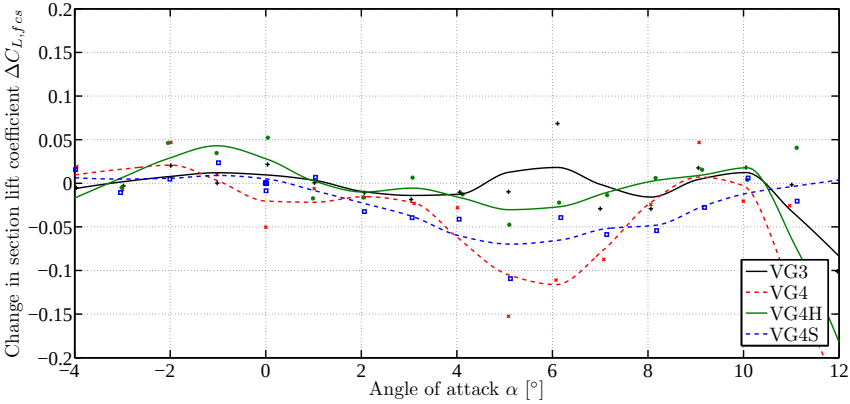

Figure 6.12: Change in section lift coefficient over angle of attack for VG3, VG4, VG4H, VG4S actuators on MOD7 airfoil.

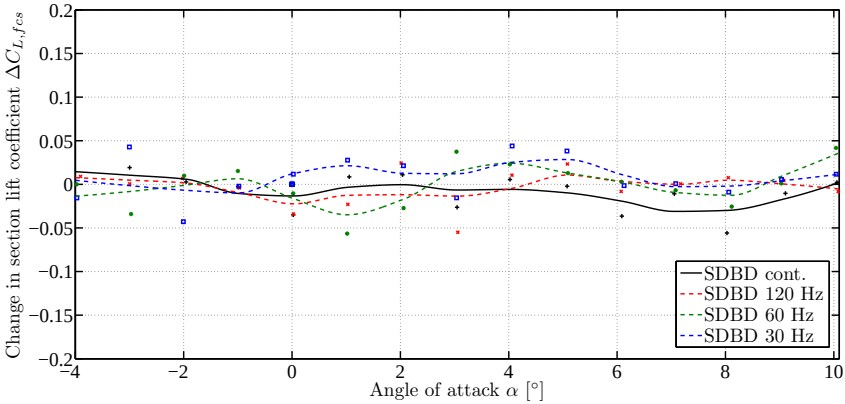

Figure 6.13: Change in section lift coefficient over angle of attack for SDBD actuator on MOD11 airfoil.

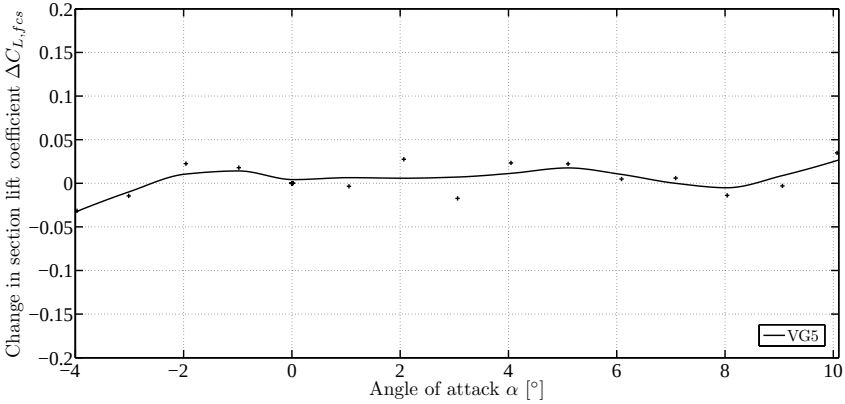

Figure 6.14: Change in section lift coefficient over angle of attack for VG5 actuator on MOD11 airfoil.

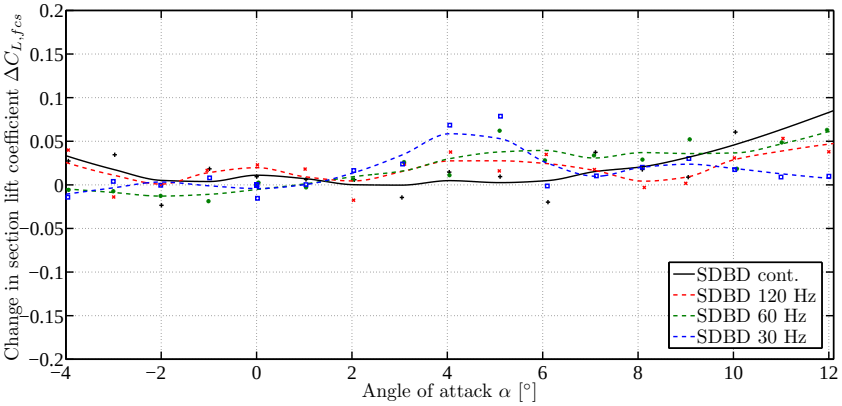

Figure 6.15: Change in section lift coefficient over angle of attack for SDBD actuator on MOD13 airfoil.

6.4.1.4 Separation Ramp Airfoil MOD13

The same behavior as for the MOD11 airfoil was found for the MOD13. Again, only two configurations were tested without achieving a flow control effect.

6.4.2 Free-Flight Results

Although present in the wind tunnel experiments, no significant effect of the plasma actuator flow control on the aircraft occurred in flight for any configuration tested. The post-flight analysis of the measured data as well as the subjective assessment of the flight characteristics during the experiments both showed no influence of the actuation. Although a small effect of the VG1S actuator on MOD7 airfoil is apparently visible in the evaluation of flight 6, as shown in Figure 6.19, it is not present for the replication, shown in Figure 6.20.

Compared to the wind tunnel several parameters are changed and could be potential causes for this discrepancy:

- The flow conditions, especially the turbulence, in the wind tunnel and in free-flight greatly differ. This is actually one of the most important motivations to undertake free-flight experiments, but the results are

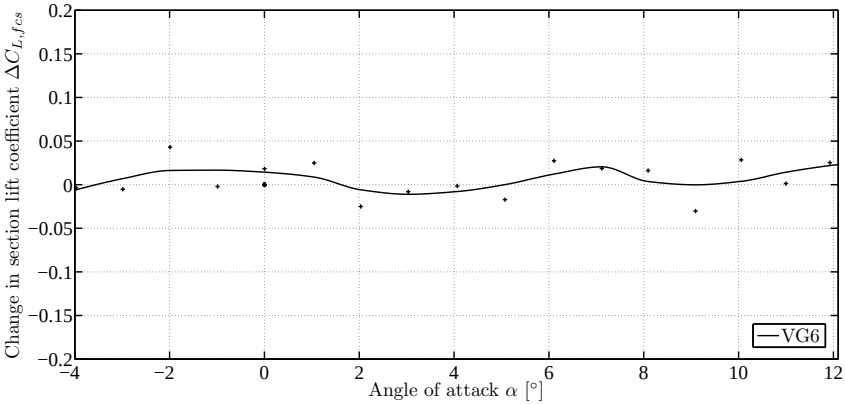

Figure 6.16: Change in section lift coefficient over angle of attack for VG6 actuator on MOD13 airfoil.

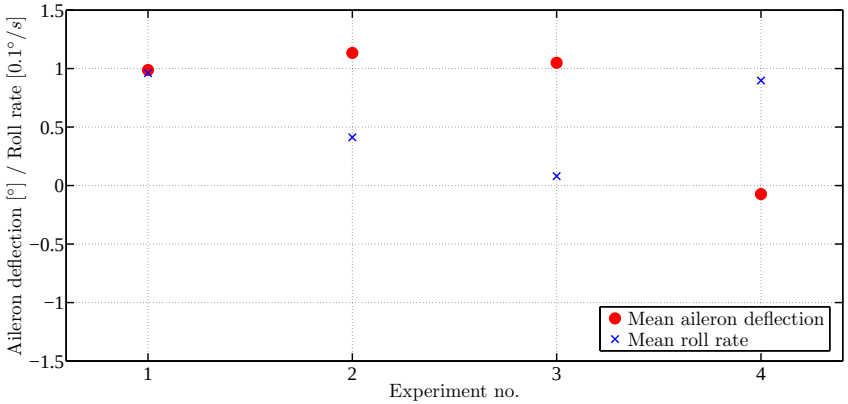

Figure 6.17: Aileron deflection and roll rate for IMP actuator on NACA0015 airfoil in free-flight. Depicted are the changes in deflection and roll rate due to actuation, compared to unactuated straight flight, for each experimental run of flight 4.

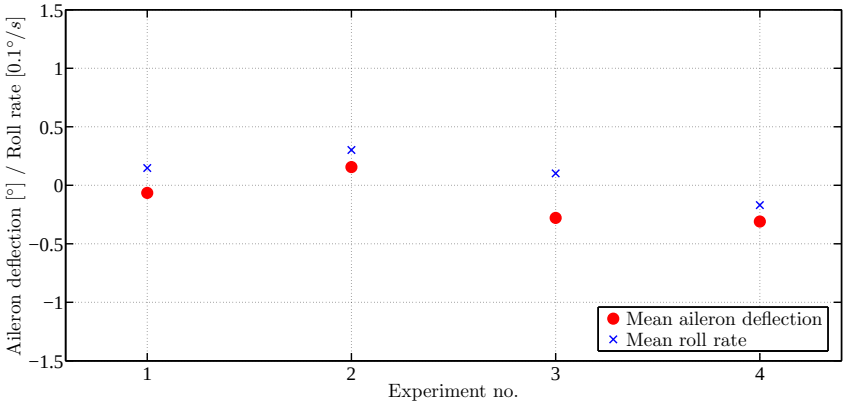

Figure 6.18: Aileron deflection and roll rate for VG4S actuator on MOD7 airfoil in free-flight. Depicted are the changes in deflection and roll rate due to actuation, compared to unactuated straight flight, for each experimental run of flight 5.

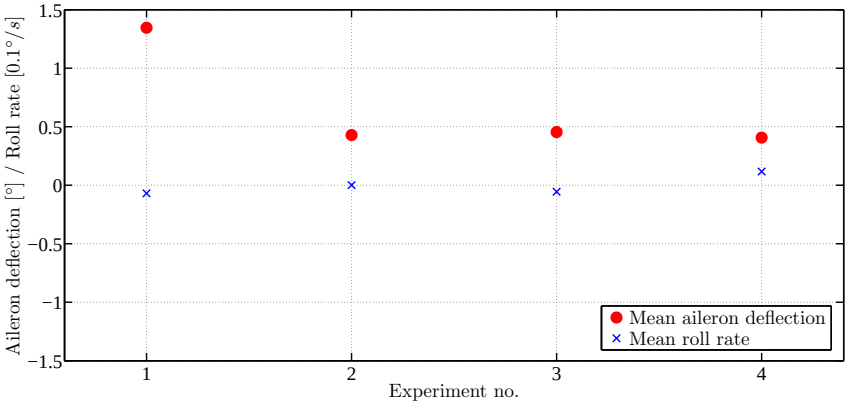

Figure 6.19: Aileron deflection and roll rate for VG1S actuator on MOD7 airfoil in free-flight. Depicted are the changes in deflection and roll rate due to actuation, compared to unactuated straight flight, for each experimental run of flight 6.

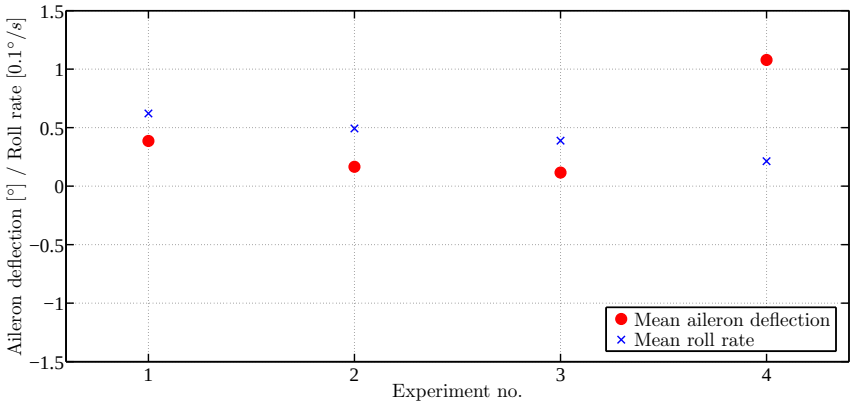

Figure 6.20: Aileron deflection and roll rate for VG1S actuator on MOD7 airfoil in free-flight. Depicted are the changes in deflection and roll rate due to actuation, compared to unactuated straight flight, for each experimental run of flight 7.

incommensurable. In flight usually a much lower turbulence is encountered, resulting in a long laminar region on the wing, especially at the low Reynolds numbers encountered on the UAV the effects are essential.

- The atmospheric conditions were not identical for each flight and considerably differ from laboratory conditions. While the pressure in the low flight altitudes for the experiments is comparable to the ground pressure, temperature and especially relative humidity are not.

  The temperature in the closed-loop wind tunnel was around 30° C, during the flight experiments temperatures between 4 and 14° C were encountered. As discussed in Section 2.4.3 the lower temperatures are expected to reduce the effect of the plasma actuator.

  Even more substantial for the actuator effect is the change in relative humidity. Although not explicitly measured during the wind tunnel measurement campaign, it is assumed as being in the range of 40 to 50%. In flight humidities from 68 to 93% were measured. In some cases even a condensation on the actuator surface was observed. Al-

though an evaporation due to the actuation occurred on the ground, the situation during flight is unknown. Nonetheless, it can be assumed, as discussed in Section 2.4.3, that the effect of the plasma actuator is greatly reduced.

- Another consideration to be made is the power supply of the actuators. In flight obviously a battery has to be used, during the wind tunnel experiments a power supply was used to save time by not recharging the batteries. A battery has two major disadvantages which have to be considered, the over time decreasing voltage and the missing ground potential. While the first effect was found to be negligible for the described experiments, due to the latter interactions, such as beats, between the two high voltage generators may occur, although a generously dimensioned battery was installed.

7 Conclusions and Outlook

7.1 The PLASMAERO UAV

In this work the design of a UAV for flow control experiments with DBD plasma actuators under realistic atmospheric conditions in free flight is described. Essential problematics, besides the design of the UAV itself, include the miniaturization of the equipment and abatement of electromagnetic interferences. It was further ensured that the aircraft can also be mounted in the NWk 1 wind tunnel of the TU Darmstadt, enabling a comparison between wind tunnel and free-flight experiments. The flow conditions in free-flight and wind tunnel experiments can be vastly different, regarding turbulence, temperature, pressure or relative humidity. Important conclusions can thus be drawn for the evaluation of flow control experiments with DBD plasma actuators conducted in a wind tunnel, with respect to the transferability to free-flight.

The developed UAV has a rectangular wing in kite configuration with span of 2.38 m, a wing chord of 0.3 m and a flight gross mass of 10 kg. With a stall speed of 13 m/s and a maximum speed in level flight of around 30 m/s, Reynolds number in the range of 280.000 to 600.000 are contrivable for the experiments. Due to the modular design of the wing, the two 0.4 m span flow-control-segments are interchangeable, different airfoil and actuator configurations can thus be investigated.

The equipment includes a remote control system, a flight control system for autonomous flight and data acquisition, two Minipuls 0.1 power supplies for the DBD plasma actuators and an actuator power measurement and control system. The Minipuls 0.1 high voltage generators are able to produce a peak-to-peak voltage of up to 12 kV, at frequencies from 5 to 20 kHz and an output power of 30 W. They are specifically designed for the use in the UAV in terms of size and weight, both boards of one generator combined weigh around 340 g. The flight control system is able to compute the state of the aircraft, autonomously fly specified routes and record all sensor data, and can be extended if necessary.

A crucial complex of problems when working with DBD plasma actuators, especially regarding future applicability in flight, is the electromag-

netic compatibility of all systems. Due to the alternating high voltage and the plasma generation strong electromagnetic emissions of various frequencies occur. It was evidenced, that a safe operation in combination with other systems can be rendered possible, if appropriate countermeasures are taken. These include the reduction of emissions, spatial separation of EMI source and victim, the use of unsusceptible equipment, notably digitally operating, avoidance of disturbed frequencies and ultimately the assurance of fail-safe operation. With the help of these measures the compatibility of all systems and a safe operation in flight were ensured. Furthermore, the disturbance of the used sensors was analyzed, only for the magnetic field sensors an appreciable error was detected, yet neither critical for the evaluation of the experiments nor for the flight controller.

With the UAV described in this study further flow control experiments with DBD plasma actuators in free-flight are rendered possible. Thus a tool is provided to bring these actuators, although still in an early stage of development as flow control device, towards a possible practical application on aircraft.

7.2 Flow Control Experiments

The circulation control effect achieved in the hitherto conducted flow control experiments with the UAV was marginal in the wind tunnel and not measurable in free-flight. Different causes for this observation can be stated. On the one hand the Reynolds numbers are relatively high compared to other experiments, and the desired effect is comparatively demanding, namely the significant change of the lift force on the wing section. Often either smaller Reynolds numbers are investigated, more powerful high voltage generators are used, or more local and sensitive effects, such as boundary layer velocity profiles, are studied. On the other hand only few configurations were tested, no exhaustive study of the different parameters was conducted to maximize the flow control effect. In particular, the decrease in lift for certain cases in wind tunnel and free-flight experiments, while achieving the anticipated increase for other configurations, is still to be investigated and explained.

Furthermore, a significant subject for the qualification of DBD plasma actuators was identified in the experiments, namely the power output in different atmospheric conditions. Temperature, pressure and relative humidity, as well as the flight velocity, have a significant influence on the actuator. Different investigations of the effect of individual parameters on

the produced wall-jet are introduced in Section 2.4.3, although no extensive study of all parameters regarding realistic atmospheric conditions encountered during flight exists. The conditions encountered during flight differ drastically from the usual laboratory conditions, temperature and pressure are usually lower, while relative humidity can be considerably higher, especially in low to medium altitudes. In the free-flight experiments the influence of high humidity and low temperatures, in some cases also slight condensation on the actuator surface, reduced the voltage reached by the actuators, and thereby the power output drastically.

7.3 Future Advancement and Use of the UAV

For future experiments with the developed UAV several modifications and additions are recommended. To precisely measure the previously discussed effect of the atmospheric conditions on the actuator, relative humidity and temperature have to be logged. To this avail a humidity sensor should be installed and the existing temperature sensor relocated into the free-stream. Furthermore, the autonomous flight controller has to be brought into service and its parameters, derived from estimations and simulation, adjusted. As a possibility to further reduce the weight of the aircraft, the revision and further miniaturization of the actuator power measurement and control system is suggested.

The organizational and logistical effort for the execution of flight experiments is tremendous, especially if the experiments can not be conducted on-site, but the equipment has to be transported to an appropriate airfield. Therefore an authorization for flights at the TU Darmstadt, or a suitable workshop for work on the UAV near an airfield should be aspired in the long term.

Moreover, prior to further free-flight flow control experiments extensive wind tunnel studies, regarding airfoil and actuator configurations, should precede, since especially in the case of the DBD vortex generators the parameter space is vast. Due to the mentioned organizational effort and inherent risk of damages to the airplane, free-flight experiments should be selectively conducted, only if the flow control causes a significant change in the produced forces.

The closed-loop control schemes for separation and circulation control for maneuvering and gust alleviation, requested for the PLASMAERO project, can first be implemented after effective flow control methods have been developed. To further pursue the concept of the aircraft as pure measurement

platform, it is recommended to implement the control schemes using distinct hardware, separate from the flight control system. To this avail the actuator power controller could be enhanced with appropriate sensors for reactive control.

7.4 Perspectives for DBD Plasma Actuator Flow Control

Although in this work the successful operation of DBD plasma actuators on a UAV in free-flight was demonstrated, no flow control effect was measured and several problems persist. The most crucial is the effectiveness of the flow control, especially challenging at higher Reynolds numbers. Several different approaches exist for flow control, namely drag reduction, most often transition control, and circulation control, for example separation control. In this study only circulation control by the manipulation of separation was investigated. Although new types of actuators have been developed, namely vortex generating and multi-DBD, successful separation control with DBD plasma actuators appears to be limited to low Reynolds numbers.

If an effective flow control setup is found, its efficiency becomes relevant. Different definitions of efficiencies are discussed in Section 2.3.5, coming to the conclusion that the overall flight mission has to be considered. In this context the objective of drag reduction seems more promising than lift enhancement. For lift control devices used as additional system, for example to further reduce the stall speed, the added weight has to be carried, although the system is used only during a very small percentage of the flight. A net weight saving due to replacement of conventional systems for lift control is doubtful, at least at the current state of the art, and for aircraft similar to the developed UAV. Drag reduction, on the other hand, is relevant to almost the entire flight mission, allowing for a much better efficiency.

A further important aspect to be considered is operational safety. Although the durability and reliability of the actuators are still inadequate for application, a sufficient improvement seems feasible. Nonetheless, the problem of high relative humidities and condensation on the actuator surface still persists. A confinement to flights completely avoiding these conditions seems impractical, on the other hand a protection of the actuator is incompatible with its working principle. Again, the objective of drag reduction

emerges as more viable for future applications than lift control, due to its lower criticality regarding operational safety.

Bibliography

[1] Description of Work v2.1, European research project PLASMAERO, project full title: Useful Plasma for Aerodynamic Control, Seventh Framework Programme, Grant agreement no.: ACP8-GA-2009-234201, 2011, 2011.

[2] S. G. Anders, W. L. Sellers, and A. E. Washburn. Active flow control activities at NASA Langley. *AIAA Paper*, 2004-2623, June 2004.

[3] J. D. Anderson. *Fundamentals of Aerodynamics*, volume 2. McGraw-Hill New York, 2001.

[4] C. Baird, C. L. Enloe, T. E. McLaughlin, and J. W. Baughn. Acoustic testing of the dielectric barrier discharge (DBD) plasma actuator. In *AIAA 2005-565; 43rd AIAA Aerospace Sciences Meeting and Exhibit, Reno, Nevada, USA*, 2005.

[5] M. J. Bamber. *Windtunnel tests on airfoil boundary layer control using a backward-opening slot.* National Advisory Committee for Aeronautics, 1932.

[6] N. Bénard, N. Balcon, and E. Moreau. Electric wind produced by a single dielectric barrier discharge actuator operating in atmospheric flight conditions - pressure outcome. In *AIAA 2008-3792; 39th Plasmadynamics and Lasers Conference, Seattle, Washington, USA*, 2008.

[7] N. Bénard, N. Balcon, and E. Moreau. Electric wind produced by a surface dielectric barrier discharge operating over a wide range of relative humidity. In *AIAA 2009-488; 47th AIAA Aerospace Sciences Meeting, Orlando, Florida, USA*, 2009.

[8] N. Bénard, N. Balcon, and E. Moreau. Jet flow control by dielectric barrier discharge - excitation by axisymmetric and flapping modes. In *AIAA 2009-776; 47th AIAA Aerospace Sciences Meeting, Orlando, Florida, USA*, 2009.

[9] N. Bénard, J. Jolibois, and E. Moreau. Lift and drag performances of an axisymmetric airfoil controlled by plasma actuator. *Journal of Electrostatics*, 67(2-3):133–139, May 2009.

[10] N. Benard, E. Moreau, N. Zouzou, H. Rabat, J. Pons, D. Hong, A. Leroy-Chesneau, P. Peschke, and C. Hollenstein. Nanosecond pulsed plasma actuators. *ERCOFTAC Bulletin 94*, 2013.

[11] A. Berendt, J. Podliński, and J. Mizeraczyk. Comparison of airflow patterns produced by DBD actuators with smooth or saw-like discharge electrode. *Journal of Physics: Conference Series*, 301(1), 2011.

[12] J. P. Boeuf, Y. Lagmich, T. Unfer, T. Callegari, and L. C. Pitchford. Electrohydrodynamic force in dielectric barrier discharge plasma actuators. *Journal of Physics D: Applied Physics*, 40:652–662, Feb 2007.

[13] R. Brockhaus. *Flugregelung*. Springer Berlin / Heidelberg, 2001.

[14] Bundesrepublik Deutschland. Luftverkehrsgesetz vom 1. August 1922 (RGBl. 1922 I S. 681), das zuletzt durch Artikel 3 des Gesetzes vom 5. Dezember 2012 (BGBl. I S. 2454) geändert worden ist, 2012.

[15] Bundesrepublik Deutschland, Bundesministerium für Verkehr. Luftverkehrs-Ordnung vom 10. August 1963 (BGBl. I S. 652), die zuletzt durch Artikel 3 des Gesetzes vom 8. Mai 2012 (BGBl. I S. 1032) geändert worden ist, 2012.

[16] G. Cai, K.-Y. Lum, B. M. Chen, and T. H. Lee. A brief overview on miniature fixed-wing unmanned aerial vehicles. In *8th IEEE International Conference on Control and Automation, Xiamen, China*, 2010.

[17] D. Caruana, J. Cambronne, P. Barricau, and A. Belinger. The plasma synthetic jet actuator for separation control. *ERCOFTAC Bulletin 94*, 2013.

[18] P. Chen, X. Zhang, S. Chappell, Z. Cai, and D. Angland. Attenuation of noise from an airfoil equipped with a high-lift device using plasma actuators. *ERCOFTAC Bulletin 94*, 2013.

[19] R. Chow and C. V. Dam. Unsteady computational investigations of deploying load control microtabs. *Journal of Aircraft*, 43(5):1458–1469, 2006.

[20] H. Coanda. Device for deflecting a stream of elastic fluid projected into an elastic fluid, 1936. US Patent 2,052,869.

[21] T. Corneli. Verbesserung der Messergebnisse durch EMV Maßnahmen bei Untersuchungen von Dielectric Barrier Discharge (DBD) Plasma Aktuatoren zur Ablösekontrolle, Bachelor thesis, TU Darmstadt, 2009.

[22] W. Crowther, M. Jabbal, and S. Liddle. Flow control fallacies: a review of common pitfalls in flow control research. *Proceedings of the Institution of Mechanical Engineers, Part G: Journal of Aerospace Engineering*, 225(1):1–11, 2011.

[23] S. David and A. Seifert. On the generation of yawing moment using active flow control. *International Journal of Heat and Fluid Flow*, 38:72–81, 2012.

[24] A. Depperois. XFLR5. http://www.xflr5.com/xflr5.htm (29 Oct. 2013).

[25] A. Depperois. XFLR5 analysis of foils and wings operating at low Reynolds numbers. 2009.

[26] M. Drela. XFOIL: An analysis and design system for low Reynolds number airfoils. In *Conference on Low Reynolds Number Airfoil Aerodynamics, University of Notre Dame*, June 1989.

[27] A. Duchmann. *Boundary-layer stabilization with dielectric barrier discharge plasmas for free-flight application.* PhD thesis, TU Darmstadt, Dec. 2012.

[28] A. Duchmann, A. Kurz, A. Widmann, S. Grundmann, and C. Tropea. Characterization of Tollmien-Schlichting wave damping by DBD plasma actuators using phase-locked PIV. In *AIAA 2012-903; 50th AIAA Aerospace Sciences Meeting, Nashville, Tennessee, USA*, 2012.

[29] A. Duchmann, B. Simon, P. Magin, C. Tropea, and S. Grundmann. In-flight transition delay with DBD plasma actuators. In *AIAA 2013-900; 51st AIAA Aerospace Sciences Meeting, Grapevine, Texas, USA*, Jan. 2013.

[30] R. J. Englar, G. Blaylock, R. J. Gaeta, G. S. Jones, and W. E. Milholen. Recent experimental development of circulation control

airfoils and pneumatic powered-lift systems. *AIAA Paper*, 345:4–7, 2010.

[31] R. J. Englar and G. Huson. Development of advanced circulation control wing high-lift airfoils. *Journal of Aircraft*, 21(7):476–483, 1984.

[32] C. L. Enloe, M. G. McHarg, G. I. Font, and T. E. McLaughlin. Plasma-induced force and self-induced drag in the dielectric barrier discharge aerodynamic plasma actuator. In *AIAA-2009-1622; 47th AIAA Aerospace Sciences Meeting, Orlando, Florida, USA*, 2009.

[33] R. Eppler and D. Somers. A computer program for the design and analysis of low-speed airfoils. NASA technical memorandum 80210, National Aeronautics and Space Administration, Aug 1980.

[34] P. Fahlstrom and T. Gleason. *Introduction to UAV Systems*. John Wiley & Sons, 3. edition, 2012.

[35] G. I. Font, C. L. Enloe, and T. E. McLaughlin. Plasma volumetric effects on the force production of a plasma actuator. *AIAA Journal*, 48:1869–1874, 2010.

[36] G. I. Font and W. L. Morgan. Plasma discharges in atmospheric pressure oxygen for boundary layer separation control. In *AIAA 2005-4632; 35th AIAA Fluid Dynamics Conference and Exhibit, Toronto, Ontario, Canada*, 2005.

[37] M. Forte, A. Debien, D. Caruana, N. Benard, P. Barricau, C. Gleyzes, and E. Moreau. Mid-chord separation control using PSJ and DBD plasma actuators. *ERCOFTAC Bulletin 94*, 2013.

[38] M. Forte, A. Seraudie, A. Kurz, S. Grundmann, C. Tropea, J. Pons, and A. Leroy-Chesneau. Boundary layer transition control with steady and unsteady DBD plasma actuation. *ERCOFTAC Bulletin 94*, 2013.

[39] M. Frey. Konstruktion und Bau eines Unmanned Aerial Vehicles (UAV) zur Erprobung von Plasmaaktuatoren. Bachelor thesis, TU Darmstadt, 2008.

[40] W. Friedrichs, S. Grundmann, and C. Tropea. Unmanned aerial vehicle for plasma flow control. *ERCOFTAC Bulletin 94*, 2013.

[41] P. H. Fung and M. Amitay. Control of a miniducted-fan unmanned aerial vehicle using active flow control. *Journal of Aircraft*, 39(4):561–571, 2002.

[42] M. Gad-el-Hak. *Flow Control: Passive, Active, and Reactive Flow Management*. Cambridge University Press, Mar. 2007.

[43] M. Gaster. Laminar separation bubbles. In *IUTAM Symposium on Laminar-Turbulent Transition*, pages 1–13, 2006.

[44] D. E. Gault. A correlation of low-speed, airfoil-section stalling characteristics with Reynolds number and airfoil geometry. NACA technical note 3963, National Advisory Committee for Aeronautics, 1957.

[45] A. Glezer. Some aspects of aerodynamic flow control using synthetic-jet actuation. *Philosophical Transactions of the Royal Society A: Mathematical, Physical and Engineering Sciences*, 369(1940):1476–1494, 2011.

[46] G. Godard and M. Stanislas. Control of a decelerating boundary layer. Part 1: Optimization of passive vortex generators. *Aerospace Science and Technology*, 10:181–191, 2006.

[47] A. Gopalarathnam, B. A. Broughton, B. D. McGranahan, and M. S. Selig. Design of low Reynolds number airfoils with trips. *Journal of Aircraft*, 40(4):768–775, 2003.

[48] D. G. Gould. The use of vortex generators to delay boundary layer separation. *Laboratory Report LR-183, National Aeronautical Establishment Canada, Ottawa*, 1936.

[49] T. Graber, S. Kohlbrecher, J. Meyer, K. Petersen, O. von Stryk, and U. Klingauf. RoboCupRescue 2013 - Robot League Team Hector Darmstadt (Germany). 2013.

[50] A. Gross, C. Pearman, R. Kremer, B. Napier, C. Gosla, A. Kurz, S. Mack, C. Brehm, B. Heine, A. Radi, et al. 1/5 scale model of Aeromot 200S SuperXimango for scaled flight research. *AIAA Paper*, 2008-6416, 2008.

[51] S. Grundmann, M. Frey, and C. Tropea. Unmanned aerial vehicle (UAV) with plasma actuators for separation control. In *AIAA-2009-698; 47th AIAA Aerospace Science Meeting; Orlando, Florida, USA*, 2009.

[52] S. Grundmann, E. Sayles, and J. Eaton. Sensitivity of an asymmetric 3D diffuser to plasma-actuator induced inlet condition perturbations. *Experiments in Fluids*, 50:1–15, 2011.

[53] H. Hagedorn and P. Ruden. Windkanaluntersuchungen an einem Junkers-Doppelflügel mit Ausblaseschlitz am Heck des Hauptflügels. 1938.

[54] B. Heine, S. Mack, A. Kurz, A. Gross, and H. Fasel. Aerodynamic scaling of general aviation airfoil for low Reynolds number application. *AIAA Paper*, 2008-4410, 2008.

[55] International Civil Aviation Organization. Manual of the ICAO Standard Atmosphere extended to 32 km, 1964.

[56] E. N. Jacobs, K. E. Ward, and R. M. Pinkerton. The characteristics of 78 related airfoil sections from tests in the variable-density wind tunnel. NACA technical report 460, National Advisory Committee for Aeronautics, 1933.

[57] Joint Aviation Authorities. Joint aviation requirements JAR-22, Sailplanes and powered sailplanes, 2001.

[58] G. S. Jones and R. J. Englar. Advances in pneumatic-controlled high-lift systems through pulsed blowing. *AIAA Paper*, 2003-3411, 2003.

[59] T. N. Jukes and K.-S. Choi. Dielectric-barrier-discharge vortex generators: Characterisation and optimisation for flow separation control. *Experiments in Fluids*, 52(2):329–345, 2012.

[60] J. C. Kok, P. Catalano, K. Kourtzanidis, F. Rogier, and T. Unfer. Coupling of CFD with advanced plasma models. *ERCOFTAC Bulletin 94*, 2013.

[61] K. Kourtzanidis, F. Rogier, G. Dufour, J. P. Boeuf, and T. Unfer. Numerical modeling of plasma actuators. *ERCOFTAC Bulletin 94*, 2013.

[62] J. Kriegseis. *Performance Characterization and Quantification of Dielectric Barrier Discharge Plasma Actuators*. PhD thesis, TU Darmstadt, Dec 2011.

[63] J. Kriegseis, T. Dehler, S. Grundmann, and C. Tropea. Flowfield-Characteristics Generated by DBD Plasma Actuators. In A. Dillmann, G. Heller, M. Klaas, H.-P. Kreplin, W. Nitsche, and W. Schröder, editors, *New Results in Numerical and Experimental Fluid Mechanics VII*, pages 233–240. Springer Berlin / Heidelberg, 2010.

[64] J. Kriegseis, S. Grundmann, and C. Tropea. Power consumption, discharge capacitance and light emission as measures for thrust production of dielectric barrier discharge plasma actuators. *Journal of Applied Physics*, 110(1):013305, 2011.

[65] J. Kriegseis, A. Kurz, A. Duchmann, S. Grundmann, and C. Tropea. Influence of air flow on the performance of DBD plasma actuators. In *AIAA 2012-0406; 50th AIAA Aerospace Sciences Meeting, Nashville, Tennessee, USA*, 2012.

[66] J. Kriegseis, B. Möller, S. Grundmann, and C. Tropea. On performance and efficiency of dielectric barrier discharge plasma actuators for flow control applications. *International Journal of Flow Control*, 4:3–4, 2012.

[67] J. Kriegseis, D. Schröter, S. Grundmann, and C. Tropea. Online-characterization of dielectric barrier discharge plasma actuators for optimized efficiency of aerodynamical flow control applications. *Journal of Physics: Conference Series*, 301(1):012020, 2011.

[68] J. Kriegseis, C. Schwarz, A. Duchmann, S. Grundmann, and C. Tropea. PIV-based estimation of DBD plasma-actuator force terms. In *AIAA 2012-0411; 50th AIAA Aerospace Sciences Meeting, Nashville, Tennessee, USA*, 2012.

[69] G. V. Lachmann. *Boundary layer and flow control: its principles and application*, volume 2. Pergamon, 1961.

[70] J. G. Leishman. *Principles of Helicopter Aerodynamics*. Cambridge University Press, 2006.

[71] A. Leroy-Chesneau, P. Audier, D. Hong, J. Podlinski, A. Berendt, and J. Mizeraczyk. Fully separated flow control using DBD plasma actuators located at the leading edge of an airfoil. *ERCOFTAC Bulletin 94*, 2013.

[72] R. H. Liebeck. Design of subsonic airfoils for high lift. *Journal of Aircraft*, 15(9):547–561, 1978.

[73] A. V. Likhanskii, M. N. Shneider, S. O. Macheret, and R. B. Miles. Modeling of interaction between weakly ionized near-surface plasmas and gas flow. In *AIAA 2006-1204; 44th AIAA Aerospace Sciences Meeting and Exhibit, Reno, Nevada, USA*, 2006.

[74] J. C. Lin. Review of research on low-profile vortex generators to control boundary-layer separation. *Progress in Aerospace Sciences*, 38(4):389–420, 2002.

[75] P. Lissaman. Low-Reynolds-number airfoils. *Annual Review of Fluid Mechanics*, 15(1):223–239, 1983.

[76] A. Marino, P. Peschke, F. De Gregorio, P. Leyland, P. Ott, C. Hollenstein, and R. S. Donelli. High voltage pulsed DBD effects on the aerodynamic performances and on the shock buffet. *ERCOFTAC Bulletin 94*, 2013.

[77] J. H. McMasters and M. L. Henderson. Low speed single element airfoil synthesis. *Technical Soaring*, 2(2), 1980.

[78] J. Meyer and A. Strobel. A flexible real-time control system for autonomous vehicles. In *Robotics (ISR), 2010 41st International Symposium on and 2010 6th German Conference on Robotics (ROBOTIK)*, pages 1–8. VDE, 2010.

[79] P. Molton, A. Leroy-Chesneau, J. Pons, Y. Carpels, P. Barricau, C. Gleyzes, M. Forte, and D. Caruana. Wing tip vortex control by plasma actuators. *ERCOFTAC Bulletin 94*, 2013.

[80] E. Moreau, A. Debien, N. Benard, T. N. Jukes, R. D. Whalley, K.-S. Choi, A. Berendt, J. Podlinski, and J. Mizeraczyk. Surface dielectric barrier discharge plasma actuators. *ERCOFTAC Bulletin 94*, 2013.

[81] K. C. Pfingsten and R. Radespiel. Experimental and numerical investigation of a circulation control airfoil. *AIAA Paper*, 2009-533, 2009.

[82] R. Pischinger, M. Klell, and T. Sams. *Thermodynamik der Verbrennungskraftmaschine*. Springer Berlin / Heidelberg, 2009.

[83] C. O. Porter, J. W. Baughn, T. E. McLaughlin, C. L. Enloe, and G. I. Font. Plasma actuator force measurements. *AIAA Journal*, 45:1562–1570, July 2007.

[84] L. Prandtl. Über Flüssigkeitsbewegung bei sehr kleiner Reibung. In *Verhandlungen des dritten internationalen Mathematiker-Kongresses*, volume III, page 484. Teubner, Leipzig, 1904.

[85] H. Quabeck. *Design, Leistung und Dynamik von Segelflugmodellen.* HQ-Modellbauliteratur, 1994.

[86] A. Rodewald. *Elektromagnetische Verträglichkeit.* Vieweg, 2009.

[87] R. J. Roth, J. Rahel, X. Dai, and D. M. Sherman. The physics and phenomenology of one atmosphere uniform glow discharge plasma reactors for surface treatment applications. *Journal of Physics D: Applied Physics*, 38:555–567, 2005.

[88] P. G. Savage. Strapdown inertial navigation integration algorithm design, Part 1: Attitude algorithms. *Journal of Guidance, Control, and Dynamics*, 21(1):19–28, 1998.

[89] P. G. Savage. Strapdown inertial navigation integration algorithm design, Part 2: Velocity and position algorithms. *Journal of Guidance, Control, and Dynamics*, 21(2):208–221, 1998.

[90] H. Schlichting and E. A. Truckenbrodt. *Aerodynamik des Flugzeuges, Band 2: Aerodynamik des Tragflügels (Teil 2), des Rumpfes, der Flügel-Rumpf-Anordnung und der Leitwerke.* Springer Berlin / Heidelberg, 3. edition, 2001.

[91] A. Seifert. Closed-loop active flow control systems: Actuators. In *Active Flow Control*, pages 85–102. Springer Berlin / Heidelberg, 2007.

[92] A. Seifert, T. Bachar, I. Wygnanski, A. Kariv, H. Cohen, and R. Yoeli. Application of active separation control to a small unmanned air vehicle. *Journal of Aircraft*, 36(2):474–477, 1999.

[93] A. Seifert, A. Darabi, and I. Wyganski. Delay of airfoil stall by periodic excitation. *Journal of Aircraft*, 33(4):691–698, 1996.

[94] A. Seifert, S. David, I. Fono, O. Stalnov, and I. Dayan. Roll control via active flow control: From concept to flight. *Journal of Aircraft*, 47:864–874, 2010.

[95] A. Seifert, S. Eliahu, D. Greenblatt, and I. Wygnanski. Use of piezoelectric actuators for airfoil separation control. *AIAA Journal*, 36(8):1535–1537, 1998.

[96] A. Seifert and L. G. Pack. Oscillatory control of separation at high Reynolds numbers. *AIAA Journal*, 37:1062 – 1071, 1999.

[97] M. Selig. Low Reynolds number airfoil design lecture notes. *VKI Lecture Series*, pages 24–28, Nov 2003.

[98] M. S. Selig and J. J. Guglielmo. High-lift low Reynolds number airfoil design. *Journal of Aircraft*, 34(1):72–79, 1997.

[99] A. R. Sinclair and A. W. Robins. A method for the determination of the time lag in pressure measuring systems incorporating capillaries. NACA technical note 2793, National Advisory Committee for Aeronautics, 1952.

[100] B. L. Smith and A. Glezer. The formation and evolution of synthetic jets. *Physics of Fluids*, 10:2281, 1998.

[101] J. H. Spurk. *Fluid Mechanics*. Springer Berlin / Heidelberg, 1997.

[102] F. Thomas and J. Milgram. *Fundamentals of Sailplane Design*. College Park Press, 1999.

[103] P. Versailles, V. Gingras-Gosselin, and H. Vo. Impact of pressure and temperature on the performance of plasma actuators. *AIAA Journal*, 48:859–863, 2010.

[104] C. S. Wells. *Viscous Drag Reduction*. Plenum Press, New York, 1969.

[105] R. D. Whalley, A. Debien, J. Podlinski, T. N. Jukes, K.-S. Choi, N. Benard, E. Moreau, A. Berendt, and J. Mizeraczyk. Trailing-edge separation control of a NACA 0015 airfoil using dielectric-barrier-discharge plasma actuators. *ERCOFTAC Bulletin 94*, 2013.

[106] B. Wilke. *Aerodynamische Strömungssteuerung mittels dielektrischen Barriereentladungs-Plasmaaktuatoren*. PhD thesis, TU Darmstadt, DLR Göttingen, 2009.

Nomenclature

Latin Letters

Upper Case

Symbol	SI unit	Description
A	m^2	Area, cross section
$\mathbf{A}$	–	State matrix
AFM	–	Aerodynamic figure of merit
$\vec{B}$	T	Magnetic field strength
$\mathbf{B}$	–	Input matrix
C	–	Coefficient (3-dimensional)
C	F	Capacitance
$\mathbf{C}$	–	Output matrix
D	N	Drag
$\mathbf{D}$	–	Feedtrough matrix
D_f	N	Friction drag
D_i	N	Lift-induced drag
D_p	N	Pressure drag
D_thr	–	Throttle position
D_w	N	Wave drag
DC	–	Duty cycle
E	J	Energy
$\vec{E}$	V / m	Electric field strength
G	N	Weight
H	N m	Hinge moment
I	A	Current
J	N s	Momentum
$\mathbf{J}$	kg m^2	Inertia matrix

L	N	Lift force
L	H	Inductance
L'	N / m	Lift per unit span
$\check{L}$	N m	Moment around x-axis
M	N m	Moment
M'	N m / m	Moment per unit span
$\check{M}$	N m	Moment around y-axis
M_b	N m	Bending moment
Ma	–	Mach number
$\check{N}$	N m	Moment around z-axis
P	W	Power
Q	N	Shear force
R	Ω	Resistance
$R_\parallel$	N / mm^2	Fibre-parallel resistance
$R_\perp$	N / mm^2	Fibre-normal resistance
$R_{\perp\parallel}$	N / mm^2	Shear resistance (in fibre-parallel plane)
Re	–	Reynolds number
Re_x	–	Local Reynolds number
S	m^2	Area of wing, stabilizer or control surface
S_{AP}	–	Plasma actuator switch position
S_{PA}	–	Autopilot switch position
T	N	Thrust
T	K	Temperature
U_{G}	m / s	Vertical gust velocity
V	m / s	Absolute velocity
V	V	Voltage
V	m^3	Volume
V_{A}	m / s	Manoeuvring speed
V_{D}	m / s	Design maximum speed
V_{S}	m / s	Stall speed
V_{W}	m / s	Wind speed
V_{pl}	V	Peak-to-peak voltage

X	N	Force in x-direction
Y	N	Force in y-direction
Z	N	Force in z-direction

Lower Case

Symbol	SI unit	Description
a	m / s	Sonic speed
b	m	Span
c	m	Chord length
c	m	Coefficient (2-dimensional)
c	m / s	Speed of light = 299, 792, 458 m/s
c_μ	m	Mean aerodynamic chord length
c_f	–	Friction coefficient
d	m	Diameter
f	Hz	Frequency
f_res	Hz	Resonance frequency
g	m / s^2	Gravitational constant ≈ 9.81 m/s^2
h	m	Height, altitude
h_b	m	Barometric altitude
k	–	Factor
k_v	Hz / V	Speed constant
l	m	Length, moment arm
m	m	Camber
m	kg	Mass
m_g	kg	Gross mass of the aircraft
m'	kg / m	Weight per unit length
$\dot{m}$	kg / s	Mass flow
n	–	Load factor
p	Pa	Static pressure
p_QNH	Pa	QNH reference pressure
$\check{p}$	s^{-1}	Rotational velocity around x-axis

q	Pa	Dynamic pressure
q_x	–	Quaternion x-component
q_y	–	Quaternion y-component
q_z	–	Quaternion z-component
q_w	–	Quaternion w-component
$\check{q}$	s^{-1}	Rotational velocity around y-axis
r	m	Radius
$\check{r}$	s^{-1}	Rotational velocity around z-axis
rh	–	Relative humidity
s	m	Half-span
t	m	Thickness
t	s	Time
u	m / s	Velocity in x-direction
u_{Fuel}	J / kg	Fuel energy density
$\vec{u}$	–	Control vector
v	m / s	Velocity in y-direction
w	m / s	Velocity in z-direction
w	m	Width
$\vec{y}$	–	Output vector
x_{sep}	m	Position of separation
$\vec{x}$	–	State vector

Greek Letters

Upper Case

Symbol	SI unit	Description
Γ	m^2 / s	Circulation
Δ	–	Difference, change
Θ	–	Pitch angle
Θ_{PA}	$s^{\frac{3}{2}} A^{\frac{7}{2}} / W^{\frac{5}{2}} m$	Plasma actuator scaling number
Λ	–	Aspect ratio

Π_P	–	Relative performance, based on power
Φ	–	Roll angle
Ψ_P	–	Relative performance drop, based on power
Ψ	–	Course angle
$\vec{\Omega}$	s^{-1}	Rotational velocity vector

Lower Case

Symbol	SI unit	Description
α	–	Angle of attack
β	–	Yaw angle
γ	–	Slope angle
δ	m	Boundary layer thickness
δ_F	–	Dimensionless thickness of fuselage
ε	–	Incidence angle
ε_0	F / m	Vacuum permittivity $\approx 8.85\dot{1}0^{-12}$ F/m
ε_r	F / m	Relative permittivity
ζ	–	Rudder deflection
ζ_P	–	Propeller loss coefficient
η	–	Elevator deflection
η	–	Efficiency
η	kg / m s	Dynamic viscosity
λ	m	Wave length
λ_{gs}	–	Geodetic longitude
μ_{PL}	–	Payload percentage
ν	m^2 s	Kinematic viscosity
ν_P	–	Propeller velocity ratio
ξ	–	Aileron deflection
ρ	kg / m^3	Air density
υ	–	Dihedral
φ	–	Fibre volume fraction in FRP
φ_{gs}	–	Geodetic latitude

χ	–	Track angle
ω	s^{-1}	Rotational velocity

Subscripts

Symbol	Description
Bat	Battery
C	Probe capacitor
E	Electrical
EM	Electric motor
F	Fuselage
Fuel	Fuel
FM	Fluid-mechanic
G	Gust
H	Horizontal stabilizer
I	Input
ICE	Internal combustion engine
O	Output
P	Propeller
PA	Plasma actuator
S	Savings
V	Vertical stabilizer
V0	Vertical stabilizer without fin
W	Wing
WJ	Wall jet
a	Aerodynamic
ad	Aerodynamic coordinate system
ail	Aileron
b	Burst
bl	Baseline case
cg	Center of gravity
d	Derivative
de	Dielectric
eff	Effective
ele	Elevator
far	Far-field

fc	Flow control
fcs	Flow control section
gs	Geodetic coordinate system
i	Reference
i	Integral
l	Left
le	Lower electrode
max	Maximum
mid	Middle section
min	Minimum
nom	Nominal
ol	Overlap
out	Outer section
p	Proportional
pl	Plasma
r	Right
rud	Rudder
ue	Upper electrode
-1	Point of zero angle of attack
0	Point of zero lift
1	Point of minimum drag
2	Point of maximum lift-to-drag ratio
3	Point of minimum sink speed
4	Point of maximum lift

Abbreviations

Abbreviation	Description
AC	Alternating current
AIAA	American Institute of Aeronautics and Astronautics
ATX	Advanced Technology eXtended form factor
A/D-converter	Analog-digital converter
BLDC	Brushless direct current electric motor
CE	Communauté Européenne conformity marking
CRP	Carbon-fibre-reinforced plastic
DC	Direct current
DBD	Dielectric barrier discharge
DOF	Degrees-of-freedom
EKF	Extended Kalman filter
EMF	Electromagnetic force
ERCOFTAC	European Research Community on Flow, Turbulence and Combustion
FCS	Flight control system
FRP	Fibre-reinforced plastic
FS	Full scale
FSR	Institute of Flight Systems and Automatic Control at the TU Darmstadt
GPS	Global Positioning System
GRP	Glass-fibre-reinforced plastic
HV	High voltage
IMP	Instytut Maszyn Przeplywowych im. Roberta Szewalskiego Polskiej Akademii Nauk
IMU	Inertial measurement unit
I2C	Inter-Integrated Circuit computer bus
LAN	Local area network
LC circuit	Resonant circuit (inductor and capacitor)
$LiFePo_4$	Lithium iron phosphate battery
LiPo	Lithium polymer battery

MDBD	Multi-DBD
MEMS	Microelectromechanical system
NiCd	Nickel-cadmium battery
NiMH	Nickel-metal hydride battery
NWk 1	Niedergeschwindigkeitswindkanal 1 wind tunnel
P	Proportional
PA	Plasma actuator
PC	Personal computer
PI	Proportional-integral
PID	Proportional-integral-derivative
PIV	Particle image velocimetry
PLASMAERO	Useful PLASMas for AEROdynamic control research project
PMMA	Poly(methyl methacrylate)
PTFE	Polytetrafluoroethylene
PT1	First-order low-pass filter
PVC	Polyvinyl chloride
PWM	Pulse-width modulation
RANS	Reynolds-averaged Navier-Stokes equations
RC	Radio control
RC circuit	Resonant circuit (resistance and capacitor)
rpm	Revolutions per minute
RS-232	Recommended Standard 232 serial interface
SDBD	Single DBD
SSD	Solid state disk
TU Darmstadt	Technische Universität Darmstadt
UAV	Unmanned aerial vehicle
UNOTT	University of Nottingham
UP	Unsaturated polyester
VG	Vortex generator
VGDBD	Vortex generating DBD
WGS-84	World Geodetic System 1984 coordinate system
WLAN	Wireless LAN

2D	Two-dimensional
3D	Three-dimensional

List of Figures

List of Tables

Wilm Christian Friedrichs

Born on 19th February 1984, in Brake (Unterweser), Germany

Education

09/2009 - 01/2014	Doctoral Research in Mechanical Engineering Center of Smart Interfaces, Technische Universität Darmstadt, Darmstadt, Germany
10/2003 - 08/2009	Studies in Mechanical Engineering (Dipl.-Ing.) Technische Universität Darmstadt, Darmstadt, Germany
08/1996 - 06/2003	Secondary Education (Abitur) Pestalozzigymnasium Idstein, Idstein, Germany

Professional Experience

09/2009 - 12/2013	Research Assistant Center of Smart Interfaces, Technische Universität Darmstadt, Darmstadt, Germany
04/2008 - 08/2008	Intern EADS Deutschland GmbH, Ulm, Germany
06/2007 - 01/2008	Undergraduate Research Assistant Institute for Fluid Mechanics and Aerodynamics, Technische Universität Darmstadt, Darmstadt, Germany
09/2003 - 10/2003	Intern Grünewald Feinmaschinenbau GmbH & Co. KG, Grävenwiesbach, Germany

Darmstadt, January 2014